Ph.D. DISSERTATION

Enhanced Neural Stimulation System using Localized Surface Plasmon Resonance of Gold Nanorods

금나노입자의 국소표면플라즈몬공명을

이용한 향상된 신경자극 시스템

By

KYUNGSIK EOM

AUGUST 2016

DEPARTMENT OF ELECTRICAL ENGINEERING AND COMPUTER SCIENCE
COLLEGE OF ENGINEERING
SEOUL NATIONAL UNIVERSITY

Enhanced Neural Stimulation System using Localized Surface Plasmon Resonance of Gold Nanorods

금나노입자의 국소표면플라즈몬공명을

이용한 향상된 신경자극 시스템

지도교수 김 성 준

이 논문을 공학박사 학위논문으로 제출함

2016 년 6 월

서울대학교 대학원

전기·컴퓨터공학부

엄 경 식

엄 경 식의 공학박사 학위논문을 인준함

2016 년 6 월

위 원 장 _____ (인)

부위원장 _____ (인)

위 원 _____ (인)

위 원 _____ (인)

위 원 _____ (인)

Abstract

Modulating neural activity is essential to clinical treatment of neurological disorder and to the study of neural function. In particular, there has been growing interest in the development of a contact-free and high spatial selective infrared neural stimulation (INS) technique for use in clinics as well as research area. Despite a potential of INS for modulating neural activities, INS suffers from limited light confinement and tissue damage due to bulk heating. This dissertation provides fundamental information on the development of enhanced INS that could circumvent the limitations of conventional INS. The first part of this dissertation demonstrates for the first time that localized surface plasmon resonance of gold nanorods (GNRs) could induce neural depolarization with safe manner by lowering the stimulation threshold. To perform optical stimulation of neural tissue with GNRs, controllable fiber-coupled laser diode system, GNRs complex and neural cells are prepared. Pulsed near-infrared (NIR) light to efficiently absorbed to GNRs rather than bulk tissue and converted into localized heat which finally triggers neural activation. In the second part of this dissertation, surface-modified GNRs are used to bind to neuronal membrane to achieve washout resistance and to locally heat the neuronal membrane for which neural activation is responsible. INS using cell-targeted GNRs are employed in other types of cells, which is discussed in third part of this dissertation. Transient intracellular calcium waves are evoked in the

astrocyte cells revealing GNRs-mediated INS stimulation can be applied in variety of cells. In the last part of this dissertation, the mechanism underlying GNRs-mediated INS is discussed. Illumination of NIR light to the GNRs at their resonant wavelength leads to local electromagnetic field enhancement and the generation localized heat. Local heat diffuses to the nearby plasma membrane which result transient temperature elevation. Transient temperature increase lead to capacitance change and/or opening of the temperature sensitive ion-channel (e.g. transient receptor potential vanilloid 1 (TRPV1) channel) which both trigger the neural depolarization. A neuron model is developed to theoretically and mathematically demonstrate on the mechanism underlying GNRs-mediated INS. These experimental and theoretical findings are expected to open up new possibilities for applications to non-invasive investigations of diverse excitable tissues and treatments of neurological disorders.

Keywords : infrared neural stimulation, gold nanorod, localized surface plasmon resonance, non-invasive neuromodulation

Student Number : 2012-30216

Contents

List of Figures

List of Tables

♦ Note

Some parts of this dissertation are extracted and adapted from the journal publications which were published or submitted during the course of this study:

1) **Kyungsik Eom**, Changkyun Im, Seoyoung Hwang, Seyoung Eom, Tae-Seong Kim, Hae Sun Jeong, Kyung Hwan Kim, Kyung Min Byun, Sang Beom Jun, and Sung June Kim, "Synergistic combination of near-infrared irradiation and targeted gold nanoheaters for enhanced photothermal neural stimulation," *Biomedical optics express*, Vol 7, No 4, 1614-1625, (2016).

2) **Kyungsik Eom**, Jinhyung Kim, Jong Min Choi, Taekyeong Kang, Jin Woo Chang, Kyung Min Byun, Sang Beom Jun, Sung June Kim, "Enhanced infrared neural stimulation using localized surface plasmon resonance of gold nanorods", *Small*, Vol. 10, No. 19, pp. 3853-3857, (2014).

3) **Kyungsik Eom**, Joonsoo Jeong, Junghoon Kim, Jinhyung Kim, Sung Eun Lee, Sung June Kim, "A Wireless Power Transmission System for Implantable Devices in Freely Moving Rodents", *Medical and Biological engineering and computings*, Vol. 52, No. 8, pp. 639-651, (2014).

4) **Kyungsik Eom**, Seo-Young Hwang, Kyung Min Byun, Sang Beom Jun, Sung June Kim, "Photothermal activation of astrocyte cells using localized surface plasmon resonance of gold nanorods", *Biomedical optics express*, submitted.

Chapter 1: Introduction

This chapter introduces the motivation behind the research for this dissertation, particularly why gold nanorods (GNRs) are employed in optical neural stimulation. In addition, this chapter defines the objectives of the thesis on developing safe, effective and wide applicable optical neural stimulation system with theoretical elucidation.

1.1. Background

1.1.1. Neuroprosthetic devices

Neuroprosthetic devices are implantable electronics devices that can replace or restore the impaired sensory and motor function by external stimuli of neural tissue. Until now, people suffering from hearing loss, vision loss and movement disorder benefit from cochlear implant [1-3], retinal implant [4-6], and deep brain stimulation (DBS) [7, 8], respectively. Among them, cochlear implant has been the most successful and helped more than 120,000 people since 1980s. Patient with a damaged hair cells cannot hear, since the hair cells cannot translate sound wave to electrical signal. In this case, cochlear implants directly stimulate auditory nerve bypassing the damaged hair cells and enable patient to hear. The success story of cochlear implant inspired engineers and clinicians to develop an electronic device for the blind patients. Age-related macular degeneration (AMD) and retinitis

pigmentosa (RP) are the most common retinal degenerative diseases leading to blindness. Patients suffering from these diseases have a problem in photoreceptor which converts light into electrical signal. Similar to the cochlear implant, retinal implant directly simulate optic nerve and substitute the function of the photoreceptor [9]. Finally, DBS stimulates neural tissue in the deep brain area for the treatment of Parkinson's diseases, essential tremor, and movement disorder [7]. The fundamental idea underlying neuroprosthetic devices is the modulation of neural activity by external stimulation. The principles and the methodologies of neural stimulation techniques will be detailed in the following chapter 1.1.2.

1.1.2. Neural stimulation techniques

Modulating neural activities is important to the clinical treatment of neurological disorder as mentioned in chapter 1.1.1 and to the study of the neuroscience. Up to date, electrical stimulation has been commonly used. Injection of electric charges to the neural cell alters the conductance of voltage-gated ion channels and lead to neural activation [10]. Electrical method is simple, reliable, robust and easy to control [11]. However, electrode must be inserted into and directly contact to the neural tissue causing severe tissue damage [11, 12]. Moreover, since biological tissue is a good conductor, electric charge spreading is inevitable limiting spatial selectivity [11]. Alternative neural stimulation techniques such as magnetic [13-15], mechanical [16] and optical methods [12, 17-20] have been suggested to modulate neural activities in central and peripheral nervous systems (Table 1).

As one of the most promising neuro-modulation technique, optical stimulation has gained popularity in the last decade, due to its appealing features

compared to the electrical stimulation: contact-free and electrical artifact-free stimulation with a spatiotemporally precise control [12, 17-19]. In particular, optogenetics technique has gained increasing attention in modulating neural activity by expressing light-sensitive cation channels such as channelrhodopsin-2 (ChR2) and halorhodopsin on the membrane of neurons [18, 19]. Although it is an excellent tool for preclinical breakthroughs, optogenetics is still unavailable in clinical use owing to controversial issues of genetic manipulation in human. Femto-second pulsed laser is an alternative tool for stimulating neural cells requiring neither genetic modification nor exogenous chemical compound with high spatiotemporal precision [21, 22], but it may produce significant photo-damage due to the generation of reactive oxygen species (ROS) upon laser irradiation [23] (Table 1).

Table 1 Comparison of neural stimulation techniques

	Electric method	**Mechanical method**	**Magnetic method**	**Optogenetics method**	**Optical method (INS, femtosecond)**
Robustness	○	Δ	×	○	Δ
Spatial selectivity	Δ	Δ	×	○	○
Cellular damage free	×	Δ	Δ	×	Δ
Surgical procedure free	×	○	○	×	Δ

1.1.3. Infrared neural stimulation (INS)

Infrared neural stimulation (INS) is a method that could modulate neural activities by irradiating pulsed infrared light with a light wavelength in the range of

1.4 μm ~ 6 μm and duration of 100 μs ~ 1000 μs [17, 20]. In 2005, Jonathon Wells et al., first demonstrated that low-level, pulsed infrared light could elicit compound nerve and muscle potential in rat sciatic nerve *in vivo* [24]. They were able to evoke neural activities by optical pulse having energy below the tissue ablation threshold. Following the work done by Jonathon Well et al, INS has been successfully employed not only in the peripheral nervous system (PNS) but also in the central nervous system (CNS). Optical stimulation of thalamocortical brain slice was able to evoke action potentials without electrical artifact [25]. Attempts to use of INS in the clinics especially for the cochlear implant have emerged since optical stimulation has incomparable spatial selectivity against electric stimulation used in the conventional cochlear implant [26-28]. The first human trials were conducted on human spinal nerve roots and found out INS worked well on human nerve as well. In this case, thermal damage was first noted at 1.09 J/cm^2 and a safety ratio of 2:1 was identified [29]. Moreover, attempts to optimize the stimulation parameters as well as speculation of reducing radiant exposure have been performed. Austin R. Duke et al. found that combined optical and subthreshold electrical stimulus can lower the radiant exposure energy [30, 31]. Interestingly, in some case of which duration of optical pulse is bigger than 1 ms, nerve conduction was blocked. Austin R. Duke et al, showed pulsed infrared light could inhibit electrically initiated axonal activation in Aplysia [32] (Table 2).

While the underlying mechanism of INS is not clear yet, recent evidences have suggested that heat-related physiological change seems to be a key factor [17, 33]. Shapiro et al. have shown that transient heat near the plasma membrane induced an increase in the membrane capacitance, leading to a membrane potential change even without the aids of ion channels [34]. They experimentally discovered that membrane capacitance is increased when irradiating pulsed infrared light in an

artificial lipid bilayer prepared from 1:1 phosphatidylcholine (PC) and phosphatidylethanolamine (PE). The transient capacitance change led displacement current through the membranes, finally generating action potentials in 'artificial neuron' which is oocyte co-expressing voltage-gated sodium (Nav1.4 α,β) and potassium (Shaker) channels. Aside from the heat induced capacitance change, researchers discovered that principal temperature sensors are expressed on the neural cells including sensory nerve endings [35, 36]. At present, six temperature-sensitive transient receptor potential (TRP) have been described. Among them TRPV1 which are activated upon noxious heat (> 43 °C) are thought to be main factor involving heat activated TRP channel [37]. In 2010 Huang et al. showed thermal activation of temperature sensitive ion channel (e.g. TRPV1) can trigger action potentials in cultured neurons [14] (Table 2).

Table 2 History of infrared neural stimulation

Year	Stimulation Target	Summary
2005	Rat sciatic nerve *in vivo* [24]	• Neural activation using infrared light (2~10 μm).
2006	Gerbil cochlear *in vivo* [38]	• Cochlear nerve activation using infrared light (2.12 μm).
2009	Rat sciatic nerve *in vivo* [30]	• Combination of optical (1.875 μm) and electrical stimulation. • Combined method lowers the laser threshold.
2010	Thalamocortical brain slice *ex vivo* [25]	• Optical stimulation (2.51 ~ 10 μm) can activate central nervous system.
2012	Primary retinal ganglion cell culture *in vitro* [36]	• Optical stimulation (1.875 μm) of sensory neuron is affected by TRPV4 channel.
2012	X. *laevis* oocytes HEK & Artificial cell *in vitro* [34]	• Transient heat induces transient capacitance change which result neural depolarization.

2013	Aplysia *in vivo* [32]	• Neural inhibition using NIR light (1.86 μm).
2015	Human spinal nerve roots *in vivo* [29]	• Feasibility of INS in human nerve. • Thermal damage of 1.09 J/cm^2.

Despite a potential of INS for modulating neural activities, INS suffers from the limited light confinement and bulk tissue heating. Conventional INS incorporating infrared wavelength in the range of 1450 ~ 2200 nm has been in trouble with tissue damage due to strong water absorption [39]. Although tissue damage is different for the stimulation strategy and condition [40], possible tissue damage due to light absorption by a bulk tissue is still existing [41, 42].

In order to overcome the limitations of conventional INS, localized surface plasmon resonance of nanoparticles were used to locally heat the neural tissue and to avoid bulk tissue heating. We will introduce localized surface plasmon resonance (LSPR) of gold nanoparticles in the following chapter.

1.1.4. Localized surface plasmon resonance (LSPR)

Recently, gold nanoparticles of various shapes including nanospheres, nanorods and nanoshells have been frequently used to offer a light-induced functionality due to their unique optical property, called localized surface plasmons (LSPs) [43, 44]. Illumination at their resonant frequency leads to an efficient light absorption and local electromagnetic field enhancement, where the absorbed energy is converted to heat [43]. Unlike propagating surface plasmons supported by a planar gold surface, nanoparticle plasmons induce the quantized electron oscillations confined to nanoscale volume, providing a means for manipulating

light-matter interaction.

Among aforementioned nanoparticles, GNRs have gained attention due to its high photothermal efficiency [45] and easy tunability of their SPR resonance, whose spectrum can be adjusted from the visible to the infrared light by controlling their aspect ratio [44]. GNRs have two distinct LSPs modes in terms of their orientation with light (Figure 1). In the longitudinal mode, incoming EM-wave oscillates the electrons in the long-axis of GNRs, while electrons oscillate along short-axis in the transverse mode. Longer wavelength of electric field is required to induce electron oscillation along the long-axis of GNRs compared to the wavelength required to induce electron oscillation along the short-axis. Among these two modes, longitudinal mode has bigger extinction cross-section area than that of the transverse mode [44]. Therefore, the longitudinal mode is more prominent for the photothermal conversion from the LSPs of GNRs.

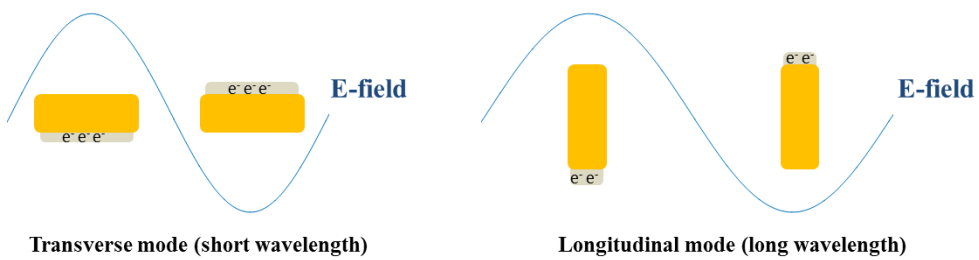

Figure 1 Illustration depicting two types of localized surface plasmon of gold nanorods; transverse (left), longitudinal (right) modes.

Plasmonic nanoparticles have been widely employed in variety fields including enhanced raman scattering [46], sensing or imaging for medical diagnostic and therapeutic medical applications [39, 47, 48]. In the therapeutic medical applications, GNRs are delivered to the target, for instance cancer cells, and generate localized heat for selective treatment [49]. Similar to the therapeutic

applications of GNRs, we could speculate that the introduction of GNRs near the plasma membrane can locally heat the membrane without bulk tissue heating. Introduction of GNRs near the plasma membrane could overcome the limitations of the conventional INS which arise from the fact that the bulk neural tissue absorb light regardless of the specific area in which is responsible for neural activation.

1.2. Objectives

1.2.1. GNRs-mediated NIR neural stimulation system

Since INS requires high laser exposure to evoke an action potential and employs the wavelength in the region of 1450 nm ~ 2200 nm in which water in the tissue strongly absorb the light, conventional INS suffers tissue damage and shallow penetration depth. The objective of this dissertation is to overcome the limitations of conventional INS by combining NIR light with GNRs, finally realizing enhanced INS in terms of safe, effective and wide applicable.

NIR spectrum was selected as a light source of noninvasive neural stimulation for several reasons. First, cells are more transparent in this wavelength compared to the infrared light [39, 50]. Moreover, compared to the visible light, NIR light can pass through the skin as well as the skull [50]. Due to these appealing features, NIR light has been spotlighted on the development of the authentic noninvasive neural stimulation.

While NIR light easily pass through the tissue, GNRs were then used to absorb the light energy delivered to the deep inside the tissue as shown in Figure 2. Matching the resonant wavelength of GNRs with the wavelength of the NIR light, GNRs efficiently absorb NIR light to generate local heat via non-radiative damping

of LSPs [51].

In this study, enhanced INS using LSPRs of GNRs was shown by demonstrating following features: (i) safe INS in terms of low laser exposure; (ii) effective INS in terms of GNRs conjugation with plasma membrane; (iii) wide applicable INS in terms of optical stimulation of non-neuronal cell.

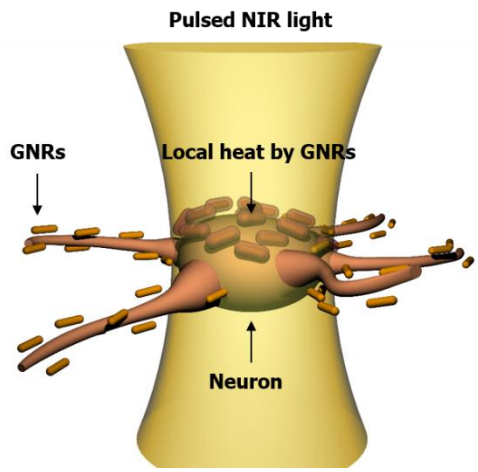

Figure 2 Schematic illustrating optical neural stimulation combined with GNRs and NIR light. GNRs absorb pulsed NIR light and generates local heat near the plasma membrane to initiate neural activation.

1.2.2. Theoretical elucidation on the origin of GNRs-mediated INS

To verify NIR light combined with GNRs locally elevate the temperature near the membrane to generate action potentials, theoretical elucidation underlying the GNRs-mediated INS was quantitatively solved using MATLAB. From the we designed the model describing from the laser exposure to the initiation of action potentials step by step as shown in Figure 3.

Interaction of light with GNRs was identified using the Gans theory. Heat diffusion from the GNRs to the nearest neuronal membrane was numerically solved

by 1-dimensional heat diffusion equation. With an aid of Gouy-Chapman-Stern theory, time course of membrane surface potential of each side of the neuronal membrane and the change in membrane capacitance was quantified. Moreover, the TRPV1 channel was modeled which is gated depending on the temperature. Both membrane capacitance change and TRPV1 channel were introduced in Hodgkin-Huxley model to generate action potentials.

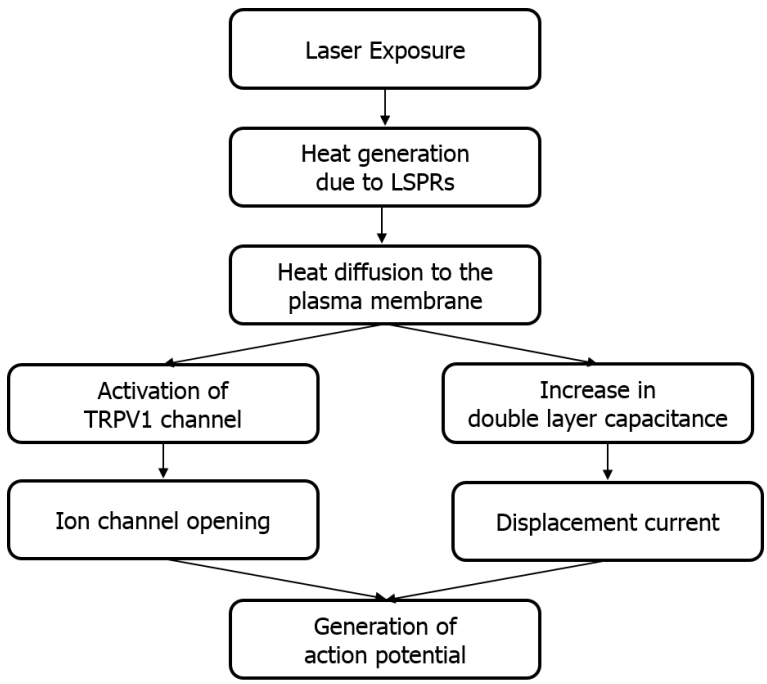

Figure 3 Flow chart showing the mechanisms underlying GNRs-mediated INS.

Chapter 2: Materials and Methods

This chapter demonstrates the materials associated with GNRs-mediated NIR neural stimulation system. This chapter starts from the design and the verification of laser system, GNRs complex and their thermal characteristics upon laser irradiation. Finally, in order to demonstrate safe, effective and wide applicable INS, neural cells were selected with corresponding recording systems.

2.1. Experimental overview

Enhanced INS using LSPR of GNRs was demonstrated by performing three subtopic experiments; (i) safe INS, (ii) effective INS, and (iii) wide applicable INS as shown in Figure 4. Moreover, theoretical mechanisms underlying GNRs-mediated INS were elucidated with numerical analysis. To validate the GNRs-mediated NIR stimulation could safely and effectively stimulate neuron as well as other non-neuronal cell, laser system, GNRs, neural cells, and recording system were prepared. First, laser system was developed to generate 980 nm wavelength laser beam. Secondarily, to absorb the light energy and generate localized heat near the plasma membrane, GNRs complex was prepared. Combination of laser and GNRs were used to activate the neural cells. Neural cells were selected that could effectively demonstrate safe, effective and wide applicable INS. Finally, after determining the appropriate neural cells, recording systems that correspond to

neural were chosen and developed. We summarized our experimental methods in Table 3.

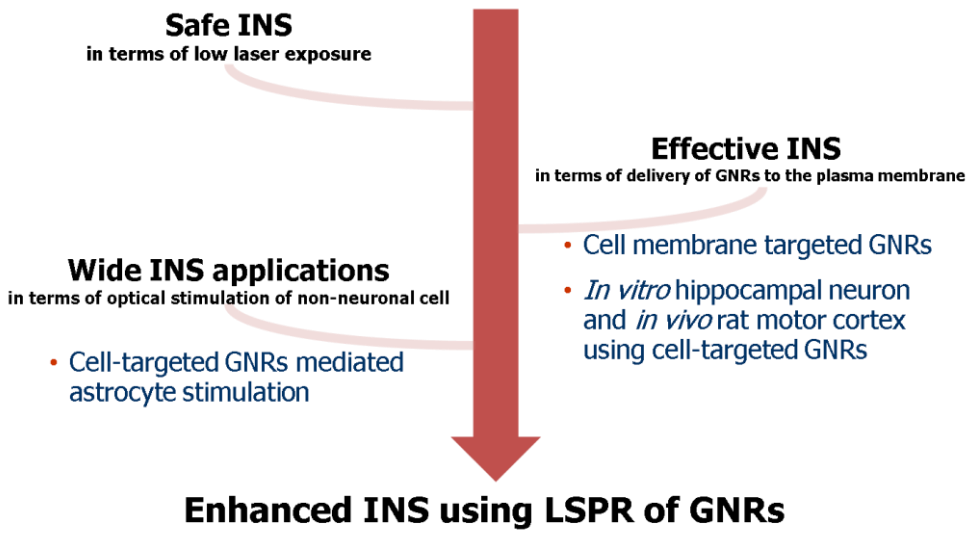

Figure 4 Schematic diagram illustrating steps toward enhanced INS using LSPRs of GNRs.

Table 3 Overall experimental configuration of GNRs-mediated NIR stimulation system.

	Safe INS	**Effective INS**		**Wide applicable INS**
Laser	980 nm fiber-coupled laser diode system (all cases)			
GNRs	Bare GNRs	Antibody-conjugated GNRs	Antibody-conjugated GNRs	Antibody-conjugated GNRs
Neural cells	Rat sciatic nerve	Rat cultured hippocampal	Rat motor cortex	Rat cultured astrocyte

	(*in vivo*)	neuron	(*in vivo*)	
Recording	Electrical recording (Single channel)	Electrical recording (Multiple channels)	Electrical recording (Single channel)	Optical recording (Ca^{2+} indicator)

2.2. Laser system

2.2.1. Design

We designed laser system to optically stimulate various types of neural cells by considering the following criteria; (i) wavelength of laser should be in the range of the optical window, (ii) intensity of laser should be at least 30 W according to the maximum stimulation threshold observed in the research done by Jonathon Wells et al [12], (iii) parameters such as pulse duration, number of pulses, pulse frequency, and pulse intensity should be manipulated, (iv) laser beam should be easily focused on the various type of cells, and (v) timing of the optical stimulation should be recorded in order to match with optically evoked neural signal recording. Based on the above mentioned criteria, fiber-coupled laser system was developed consisting of two parts; control part and operation part.

In the control part, a LabVIEW-based laser controller software was built to control the laser system and to record the neural signals. The software was designed to set the parameters of optical stimulation pulses and to deliver the laser modulation signals to the current driver in the operation part through the digital acquisition (DAQ) board as shown in Figure 5. The neural signals were recorded

simultaneously with a synchronization with optical pulses.

Operation part was designed to generate the laser beam based on the pre-set optical stimulation parameters. It consists of power supply, current driver, laser diode and lens. The temperature of the laser diode, status of current driver, applied current into the laser diode, limits of the current driver were fed into the controller part to check and monitor the status of the laser (Figure 5).

Detail parts of each component are shown in the chapter 2.2.2 and 2.2.3.

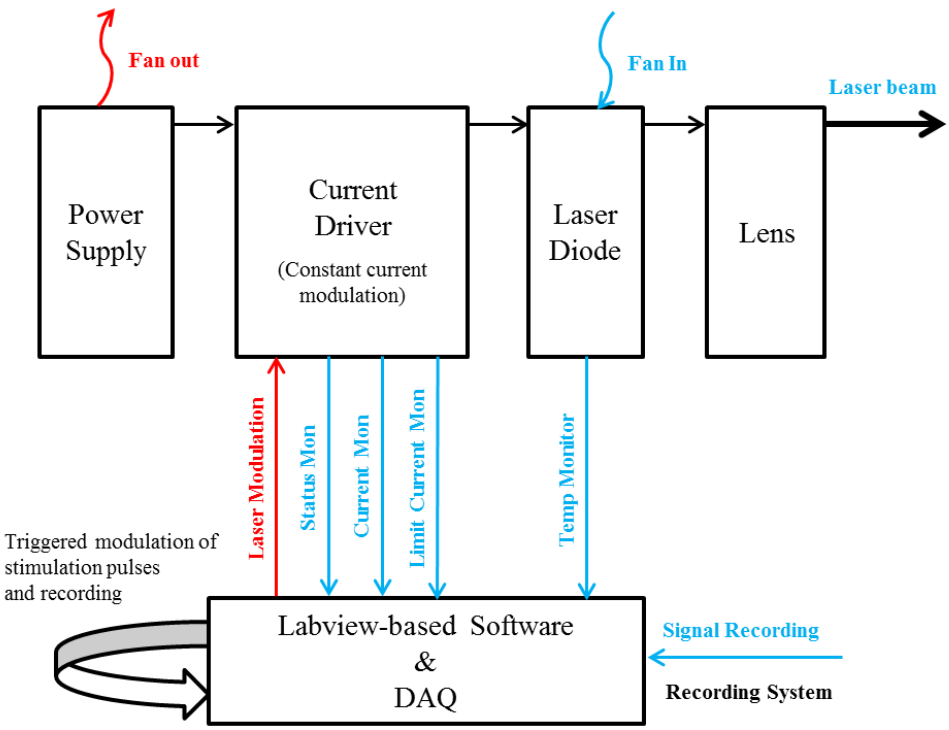

Figure 5 Schematic diagram of the laser system consisting of control part and operation part. In the control part, LabVIEW-based software was designed to control laser and record the neural signal. Focused optical pulses were generated from the control part.

2.2.2. Hardware

In the operation part, we integrated lens, a laser diode, a current driver, and a power supply. The laser diode with a wavelength of 980 nm was used to optically

stimulate a neuron. 980 nm wavelength was chosen since this wavelength is more transparent to the biological tissue including skin and skull compared to visible and infrared light over 1.4 μm. The laser diode was directly coupled to the 400 μm core optical fiber having a numerical aperture equal to 0.14 (Pearl P14 Series, nLIGHT, Vancouver, WA, USA). Fiber-coupled laser is advantageous when delivering laser beam in various experimental circumstances. To focus a laser beam, collimator and focusing lens were mounted at the end of the fiber creating a beam diameter of ~600 μm laser pulses. We monitored the temperature of the laser diode by measuring the resistance of the embedded thermistor and converted temperature from the measured impedance using the Equation 1.

$$\frac{1}{T} = 1.4 \times 10^{-3} + 2.37 \times 10^{-4} \ln(R) + 9.9 \times 10^{-8} (\ln(R))^3 \qquad \text{Equation 1}$$

where, T is the temperature [K] and R is the resistance [ohm] of the thermistor.

Fiber-coupled laser diode was driven by the current driver (PLD 10K-CH, Wavelength Electronics Inc., MT, USA) according to the optical stimulation parameters (Figure 6). Laser modulation signals were delivered to the driver from the control part. The modulation signals which convey the information of optical pulses were converted into current which operates the laser diode (Equation 2). Finally, modulated current from the current driver are fed into the laser diode.

$$I_{laser\ diode} = 4.6 \times V_{modulation} \qquad \text{Equation 2}$$

where $I_{laser\ diode}$ is the input current of laser diode [A] and $V_{modulation}$ is the modulated

input voltage of laser diode driver.

At last, power supply was connected to the laser driver to operate the system and to generate optical pulses. Moreover, Air-cooling method using fans were integrated to cool down the laser system (Figure 6).

Figure 6 A picture of fiber-coupled laser diode system

In the control part, DAQ (PXI-6221 and PXI-6132, National Instruments, Austin, TX, USA) were used to deliver laser modulation signals to the current driver and send the status of the laser system such as temperature of the laser diode, status of current driver, applied current into the laser diode, a limit of the current

driver to the software. This system is also connected with an electrophysiological setup to acquire optically evoked neural activities through 4-channels DAQ (PXI-4462, National Instruments).

2.2.3. Software

A LabVIEW-based software has been developed to control the laser system, acquire and analyze the data real-time. The software consists of three parts as controller part, recording part, and analyze part.

First, optical and recording parameters were configured in the controller part. In particular, parameters involving optical pulses such as pulse duration, pulse frequency, and pulse intensity can be configured. In the recording system, recording conditions (e.g. types of digital filter and its specific performance and number of averaging of the recorded data) can be easily configured. Second, the software acquires recorded data which were temporally synchronized with the onset of optical pulses by a common trigger clock. Data were acquired continuously and repeatedly for every 1 s. Finally, the software analyzes the recorded data real time and show the recorded data.

In some situations, where commercial recording systems were used for recording, only the laser controller part and the trigger clock are adopted to synchronize recorded data with optical pulses while neglecting recording part. All the versions of software we implemented are shown in Figure 7.

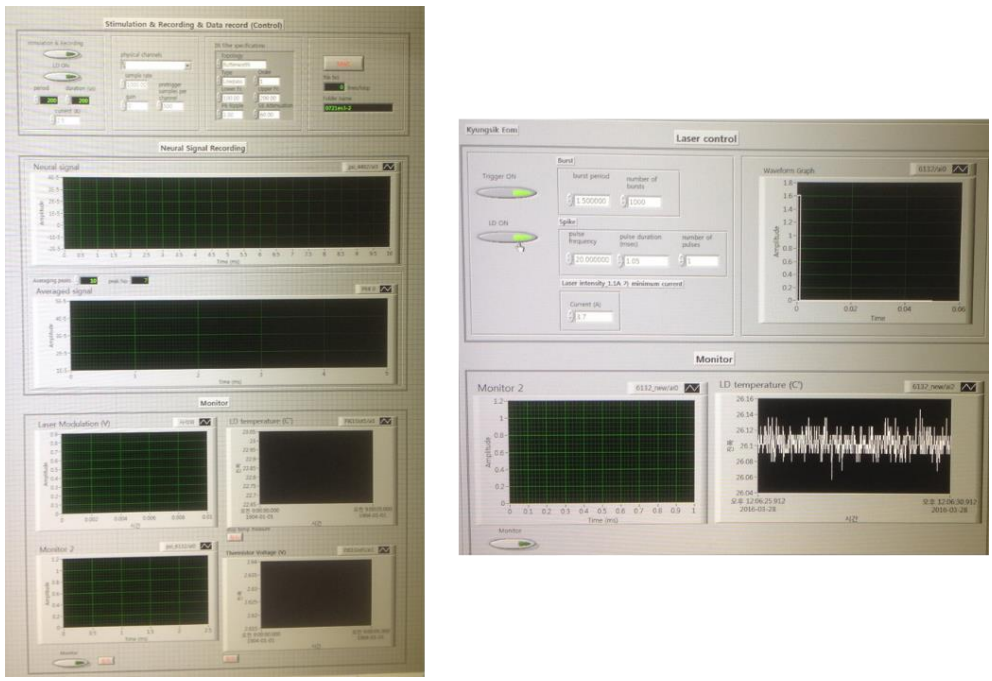

Figure 7 Pictures of LabVIEW-based software with recording part (left) and without recording part (right).

2.2.4. Calibration

The laser system was calibrated in two aspects; laser intensity and temporal profile of pulse.

Laser diode was driven by current input generated from the laser driver. We measured the pulse energy while increasing the input current that fed into the laser diode. Energy of optical pulse was measured using energy meter (PM100D, ES11C, Thorlabs, Newtown, NY, USA) with a fixed duration of 1 ms. Linear relationship between the current and the pulse energy was found and a fitting curve having an Equation 3 (Figure 8).

$$y = 0.0085 \times x - 0.0052 \qquad R^2 = 0.9953 \qquad \text{Equation 3}$$

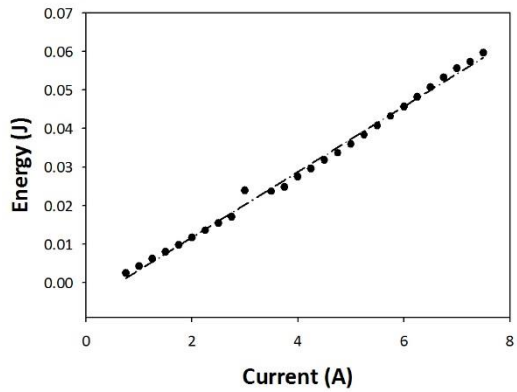

Figure 8 Graph of laser input current and the optical pulse of 1 ms duration.

Temporal profile of laser pulse was monitored using photodetector (PDA100A-EC, Thorlabs). Pulse frequency, number of pulses, and the repetition rate were well controlled as configured parameters. However, laser response to the onset of laser driver is lagged by 50 μs and the short tails appeared at the end of the pulse. Figure 9 shows linear relation of measured pulse duration with an preset pulse duration.

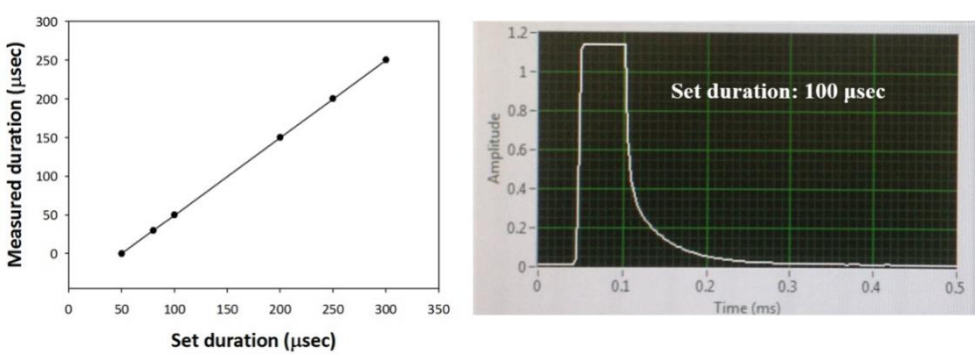

Figure 9 Relation of preset pulse duration and measured duration (left). Temporal profile of laser pulse preset by 100 μs duration (right).

2.3. GNRs complex

2.3.1. Characteristics of GNRs

At first, structural and optical properties of GNRs were characterized. Streptavidin-coated GNRs (C12-10-980-TS, Nanopartz Inc., Loveland, CO, USA) with a concentration of 3.4×10^{13}/mL and 2.8 mg/mL were prepared. The size and shape of GNRs were characterized by transmission electron microscopy (TEM, Libra 120, Carl Zeiss, Germany) and extinction spectrum was measured using a wide-band spectrophotometer (UV-1800, Shimadzu, Japan) to find a surface plasmon resonance peak. As shown in Figure 10, average values of the length and width of GNRs are measured as 80.4 ± 6.3 nm and 15.3 ± 0.58 nm, respectively, resulting in the aspect ratio equal to 5.3. For elongated GNRs with two plasmonic resonance modes, as a longitudinal mode at λ = 977 nm along the long-axis is more prominent for photothermal effect than a transverse mode at λ = 505 nm, pulsed infrared laser with a wavelength of λ = 980 nm is chosen as a light source of NIR stimulation (Figure 11). Moreover, due to the geometrical inhomogeneity, broadening at the SPR peak was observed which causes reduced photothermal efficiency. While extinction peak of GNR is adjustable in a wide range of visible and NIR wavelengths depending on the aspect ratio [44, 48], the use of resonant wavelength in NIR band is considered advantageous in terms of heat generation in a deep tissue [39].

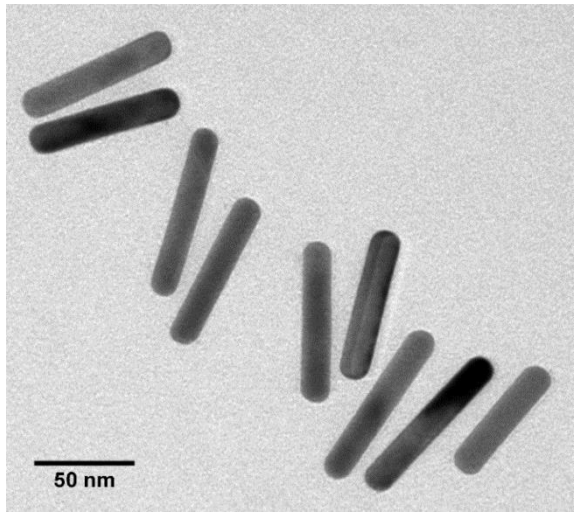

Figure 10 TEM image of GNRs.

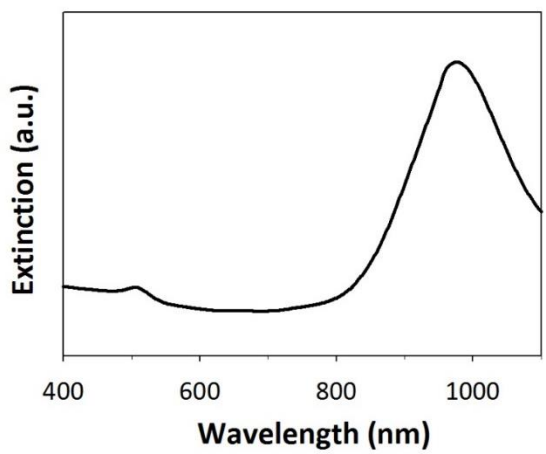

Figure 11 Extinction spectrum of GNRs.

2.3.2. Photothermal effect of GNRs

For optically evoked action potentials, it has been hypothesized that temperature elevation vicinity of the neuron cell can depolarize the membrane potential by directly changing membrane capacitance or opening the temperature-sensitive ion channels [34, 36, 52]. Thus, local heat generation by GNRs and rapid

heat dissipation are important for spatiotemporally precise stimulation of neuronal activity. In order to measure the temperature change induced by the GNRs-mediated NIR stimulation, FITC bound to GNRs was employed because its fluorescent intensity is proportional to the temperature change of surrounding medium [14, 53]. Therefore, the temperature dependence of biotinylated FITC was characterized in aqueous solutions. While the solution containing FITC is slowly heated in a custom-made chamber equipped with a temperature controller (TC02, MultiChannel systems), the fluorescent intensity was recorded with high sensitive CCD camera (Zyla 5.5 sCMOS, ANDOR, UK) and the average fluorescent intensity in a region of interest was obtained during temperature change. Figure 12 shows a linear decay of normalized fluorescent intensity with an increasing temperature. Linear regression analysis shows that fluorescent intensity as a function of temperature change is determined to be $y = -0.0047x + 1.002$ and R^2=0.9852. Fit line obtained is used to estimate the time-varying temperature characteristic.

After finding the relation between temperature change and fluorescent intensity, we measured the temperature change due to the laser exposure. We enclosed 10 μL solution containing biotinylated FITC (1 mg/mL) bound to GNRs (1.7×10^{11}/mL) between a microscope slide glass and a cover glass (Marienfeld-Superior, Lauda-Königshofen, Germany). Laser beam with a radiant exposure 190 mJ/cm^2 and a pulse width of 400 μs was irradiated on the thin sandwiched sample and fluorescent signals were collected during 10 ms before and 100 ms after the onset of optical stimulation with a frame rate of 500 frames per seconds. Fluorescent intensity of each image was averaged and converted into an average temperature. When a solution containing biotinylated FITC bound to GNRs was irradiated by the laser, the temperature rapidly increases up to 5 °C within 20 ms

and returns to the base level room temperature immediately (Figure 13). On the other hand, no significant temperature change occurred in the solution without GNRs. This indicates that local temperature increases by illuminating GNRs can induce a selective and localized heating of neuron cells depending on the presence of GNRs and contribute to a rapid and spatiotemporally precise optical stimulation of neuron cells.

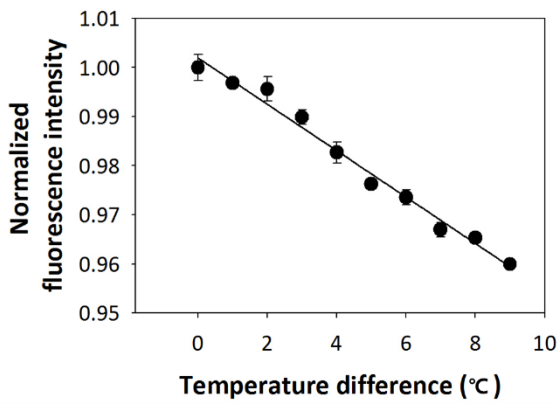

Figure 12 Graphs of normalized fluorescence intensity of FITC upon temperature change.

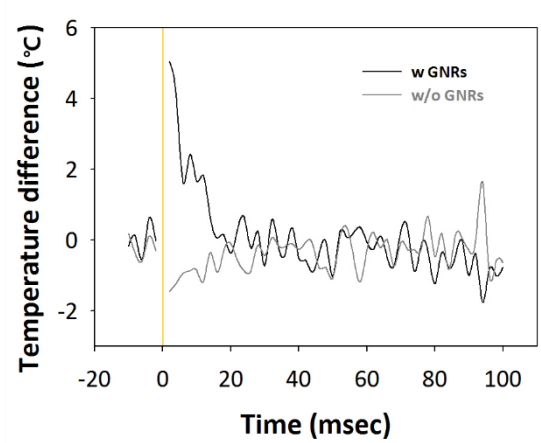

Figure 13 Temperature profile of the medium with and without GNRs upon optical stimulus (yellow box)

2.3.3. Orientation of GNRs

Unlike spherical gold nanoparticles, GNRs respond to the light to generate LSPs depending on their orientation between the light. As mentioned in chapter 1.1.4, longitudinal LSP is induced when the direction of polarization of incident light matches the long-axis of GNRs, while the transverse LSP is generated when the incident light is perpendicular to the long-axis of GNRs. To create the longitudinal LSP mode which is more prominent for photothermal conversion than the transverse mode [44], the incident light should be polarized with respect to the long-axis of GNRs. Unfortunately, neither semiconductor laser is polarized nor GNRs are uniformly oriented along polarization of incident beam. In this situation, the coupling efficiency of light with GNRs should be considered.

The amount of light coupled to the GNRs increases when GNRs absorb much more electric field. We could speculate that the absorption cross-section area increases as amount of light coupled to the GNRs increases. In this chapter, extinction (≈ absorption) cross-section area is used compare the light interaction with GNRs.

Before considering the relation of light with GNRs, we assumed the followings; (i) direction of polarization is set to maximize the LSPs of GNRs, (ii) polarized light is originally made by passing unpolarized light through polarizing filter, (iii) concentration of GNRs is low enough so that extinction cross-section areas of each GNRs do not overlap, and (iv) probabilities of GNRs with specific orientation are assumed as below.

Single orientation ($0 \leq \theta < 2\pi$)

$$p(\theta) = 1 \quad (when\ \theta = 0)$$

$$0\ (when\ \ \theta \neq 0)$$

Random orientation ($0 \leq \theta < 2\pi$)

$$p(\theta) = \frac{1}{2\pi}$$

At first, the extinction-cross section area of a single GNR is determined. The extinction cross-section area of a GNRs upon its orientation angle is defined as Equation 4 [54, 55]. For longitudinal LSPR mode, extinction cross-section area maximized when direction of polarization of light matches to the long-axis of GNRs at longitudinal LSPR mode.

$$\sigma_{ext} = \sigma_{\parallel} cos^2\,\alpha + \sigma_{\perp} sin^2\,\alpha \approx \sigma_{\parallel} cos^2\,\alpha \qquad \text{Equation 4}$$
$$(\sigma_{\perp} = \ 0\ \ at\ \ longitudinal\ \ mode)$$

Based on the extinction cross-section area of a single GNR, we could find the average extinction cross-section area of total GNRs. By simply multiplying the extinction cross-section area with a probability of GNRs with a certain direction and integrate for all directions, then we could find the average extinction cross-section area as shown in Equation 5.

$$\int_0^{2\pi}\int_0^{2\pi} \sigma_{\parallel} cos^2(\theta)p(\theta) \times cos^2(\varphi)p(\varphi)\, d\theta d\varphi \qquad \text{Equation 5}$$

$\sigma(\theta/\varphi)$: $extinction\ cross-section\ area\ at\ polarization\ angle\ of\ \theta/\varphi$

$p(\theta/\varphi)$: $probability\ of\ GNRs\ with\ polarization\ angle\ of\ \theta/\varphi$

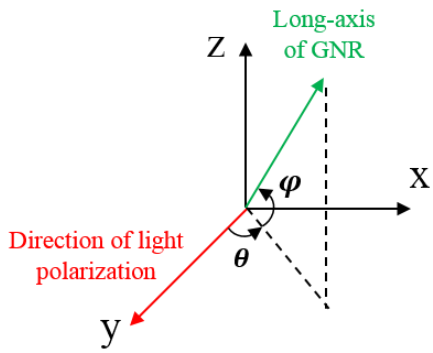

Figure 14 Direction of light polarization and long-axis of a GNR

From the Equation 5, we determined the average extinction cross-section area of GNRs for all cases of polarizations of light and the orientations of the GNRs as shown in the Table 4.

Table 4 Average extinction cross-section area of GNRs upon polarizations of light and GNRs orientations.

Light Polarization	**GNRs Orientation**	**Average extinction cross-section area (normalized)**
P	$\boldsymbol{\theta_s\varphi_s}$	1
P	$\boldsymbol{\theta_s\varphi_R}$, $\boldsymbol{\theta_R\varphi_s}$	0.5

P	$\boldsymbol{\theta_R \varphi_R}$	0.25
U	$\boldsymbol{\theta_s \varphi_s}$	1
U	$\boldsymbol{\theta_R \varphi_s}$	1
U	$\boldsymbol{\theta_R \varphi_R}$, $\boldsymbol{\theta_s \varphi_R}$	0.5

P represents polarized light.

U represents unpolarized light.

$\boldsymbol{\theta/\varphi_s}$ represents that GNRs are oriented in single orientation in the direction of θ, φ.

$\boldsymbol{\theta/\varphi_R}$ represents that GNRs are oriented randomly in the direction of θ, φ.

Since we used unpolarized light, detail explanations for the case of unpolarized light is discussed. When GNRs are oriented in a single direction for instance *y*-axis as shown in the Figure 15, the average extinction cross-section area becomes the maximum since the direction of light propagation matches to the long-axis of GNRs. Similarly, the maximum extinction cross-section area is obtained even for the case when GNRs are randomly distributed in θ direction (or *xy*-plane) (Figure 16). However, the situation is changed if the GNRs is randomly distributed in the plane of electric field of oscillation (Figure 17). Some GNRs whose long-axes are not aligned in the polarization direction of light generate reduced LSPs. From the Equation 5, when shining an unpolarized light to randomly distributed GNRs, the average extinction cross-section area is reduced to half from the maximum extinction cross-section area which can be obtained in the case when using polarized light with GNRs aligned in parallel.

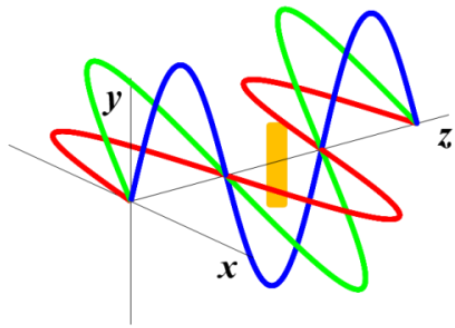

Figure 15 Unpolarized light and GNR oriented in the direction of *y*-axis.

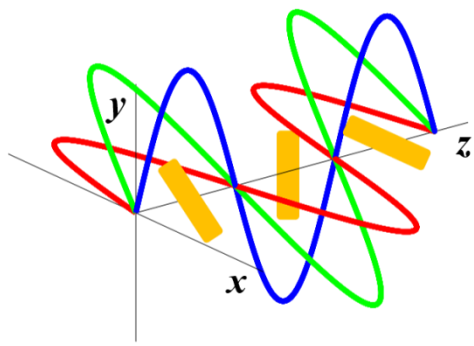

Figure 16 Unpolarized light and GNRs oriented in the direction of each linearly polarized light

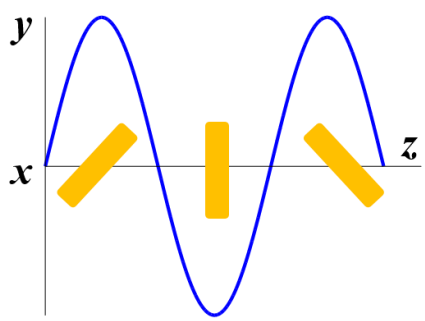

Figure 17 Incident light in *z*-direction and randomly distributed GNRs in *yz*-plane.

Overall, to attain maximum extinction cross-section area, long-axes of GNRs must be perpendicular to the direction of incident light as followings: (i) polarized light with uniformly oriented GNRs whose long-axis are perpendicular to the direction of light; (ii) unpolarized light with randomly distributed GNRs in a plane normal to the direction of light.

We could categorize our experiments in terms of the orientation GNRs: (i) in the *in vitro* experiments, GNRs are randomly distributed in quasi-2D surface, (ii) in the *in vivo* experiments, GNRs randomly distributed in 3D volume. When GNRs are randomly distributed in quasi-2D surface and the light are irradiated normal to the 2D surface, then GNRs generates nearly the maximum LSPs. However, when GNRs are randomly distributed in 3D volume, average LSPs generated by GNRs is about the half the maximum. We will show about the types of tissue the in section 2.4. GNRs in the experiments using cultured hippocampal neurons and cultured astrocyte cells distributed in quasi-2D surface, while GNRs in the experiments using rat sciatic nerve *in vivo*, and motor cortex *in vivo* distributed in 3D volume.

2.4. Neural cells

We demonstrated that combination of GNRs and NIR stimulation is safe, effective and wide applicable by performing experiments in different types of cells. First, Safe INS in terms of low laser exposure was experimentally confirmed in the *in vivo* rat sciatic nerve. Optically evoked neural responses were recorded electrically. Second, effective INS in terms of delivery of GNRs to the plasma membrane was demonstrated in cultured rat hippocampal neuron *in vitro* and rat motor cortex *in vivo*. Multielectrode arrays (MEAs) were used to record neural

activities of cultured hippocampal neurons. Cell-targeted GNRs-mediated INS induced motor behavior were videotaped with simultaneous electrical recording. Finally, wide applicable INS in terms of optical stimulation of non-neuronal cell was experimentally confirmed in cultured rat astrocyte *in vitro*. Calcium imaging was performed to optically monitor intracellular calcium transient of cultured astrocyte.

2.5. Experimental protocols

2.5.1. Safe INS

To validate GNRs-mediated INS can safely stimulate neural cells with low laser exposure, *in vivo* rat sciatic nerve and electrical recording system was used. We performed the experiments in the following process; (i) preparation of rat, (ii) injection of GNRs to the rat sciatic nerve, (iii) optical stimulation and electrical recording, and (iv) histological analysis.

Spraque-Dawley rat (~350 g) was anesthetized with intraperitoneal injection of urethane (1.5 g/kg). All animals were treated in accordance with the animal research guidelines of Use Committee of the Institute of Laboratory Animal Resources at Seoul National University. To access the sciatic nerve, an incision was made from the biceps femoris muscle to the gluteus muscle. The muscle covering the nerve was carefully removed to expose the nerve surface while continually moistened with saline buffer.

Prior to optical stimulation of sciatic nerve, GNRs were prepared and injected to the sciatic nerve *in vivo*. Injection was conducted using microprocessor-controlled injection system (Nanoliter 2010, World Precision Instruments, Sarasota,

FL, USA) which was mounted on a micromanipulator [56]. A 75 μm diameter, 30º beveled pulled glass capillary injection tip (SBB-75X, Sunlight Medical, Jacksonville, FL, USA) was coupled with the injection system. GNRs were filled in the glass capillary tip via front filling. The tip was moved until it pierced the tissue of the distal part of the exposed nerve bundle. Once the penetration was achieved, GNRs were injected at the rate of 23 nL/s.

The distribution of gold nanorods inside the nerve bundle was visualized as follows. Sciatic nerve bundle was excised and the specimen was fixed via Karnovsky's fixation (primary fixation). Washing out the Karnovsky's solution by 0.05 M sodium cacodylate buffer was, then, followed. Lipid fixation was conducted (post fixation, 2 % osmium tetroxide and 0.1 M cacodylate buffer). After washing the sample, an en-block staining was performed. The samples were dehydrated by soaking into the ethanol solution. Infiltration by spurr's resin was performed after transiting the environment as the resin friendly by propylene oxide. The polymerized specimen block was sectioned with a 5 nm thickness via ultramicrotome (MTX, RMC, USA). The sample was reviewed via the 80 kV TEM (JEM1010, JEOL, Japan).

Fiber-coupled laser at λ = 980 nm illuminated the proximal part of the nerve bundle where a 1 μL of GNR solution was injected in advance using micro-injector while extracellular electrical recording was performed at the distal as shown in Figure 18. Optically evoked responses were recorded via electrical recording system. From the preamplifier (×10), optically evoked signals were pre-amplified and were fed into the differential AC amplifier (Microelectrode AC Amplifier Model 1800, AM systems, Carlsborg, WA, USA) whose gain was set as 1,000 and band-pass filter was ranged from 10 Hz to 10 kHz. Amplified electrical signals

were recorded with a data acquisition system (PXI-4462, National Instruments, Austin, TX, USA). Data recording were pre-triggered 1.6 ms prior to the optical stimulation pulse and the signals were monitored while 15 signals were averaged simultaneously.

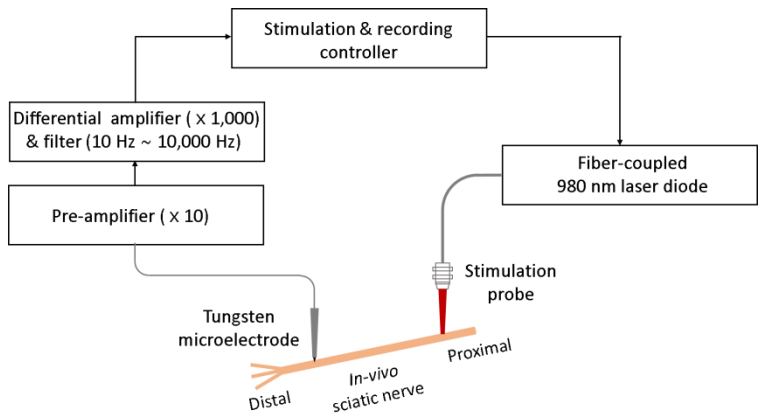

Figure 18 Schematic of stimulation and recording system of rat sciatic nerve *in vivo*

For identification of laser mediated tissue damage, the nerve was excised and immediately subjected to laser irradiation. The nerve was, then, placed in 4 % paraformaldehyde solution and sent for the paraffin embedding. The tissue block was sectioned sagittally with 4 μm thickness and placed on the glass slide. The tissues were stained with hematoxylin and eosin (H&E) [41]. All the sections were reviewed using a photomicroscope (Axiophot, Carl Zeiss, Germany).

2.5.2. Effective INS

In the chapter 2.5.1, we presented that an optical neural stimulation using NIR light incorporating plasmonic nanoheaters injected in a proximity of neuron cells could reduce the stimulation threshold. However, unconjugated nanoparticles

might be ineffective when they are washed off by extracellular fluid flow. Strongly bound nanoparticles to the target are more critical in central nervous system (CNS) because body fluid such as cerebrospinal fluid (CSF) in CNS flows continuously through living cells to dump out the metabolic wastes [57-59]. Therefore, it is essential to make a strong conjugation GNRs and the surface of membrane to overcome GNRs washout due to convective solution.

In this chapter, *in vitro* cultured hippocampal neuron was used to verify cell-targeted GNRs effectively depolarize neuron with fast neural response. Moreover, cell-targeted GNRs were employed to rat motor cortex *in vivo* to cortically control the motor behavior.

2.5.2.1. Cell-targeted GNRs-mediated NIR stimulation of cultured hippocampal neuron

We performed the experiments in the following process; (i) primary hippocampal neuron culture, (ii) conjugation of GNRs to the neuronal membrane, (iii) optical stimulation and electrical recording.

Hippocampi were dissected from Sprague-Dawley rat embryos (E19) under sterile conditions in accordance with the animal research guidelines of Use Committee of the Institute of Laboratory Animal Resources at Ewha Womans University (IACUC No. 15-045). Cells were dissociated using 5% trypsin-EDTA for 15 mins prior to trituration and then were plated at 1,800 cells/mm^2 on multi-electrode arrays (MEAs, MultiChannel systems, Reutlingen, Germany) coated with poly-L-lysine (P4707, Sigma-Aldrich, St. Louis, MO, USA) [60, 61]. Culture of hippocampal cells for 2 to 3 weeks was found to provide tightly synchronized periodic bursting, which was advantageous for distinguishing spontaneous activity

from optically evoked activity [61, 62]. The culture medium refers to the method by Brewer et al.; Neurobasal medium (NEUROBASAL™ Medium, 21103, GIBCO®, CA, USA) with B-27 supplement (17504-044, GIBCO®, CA, USA), 2 mM glutamax (35050, GIBCO®, CA, USA), and antibiotics (15240, Life technologies, Carlsbad, CA, USA) [63]. Cultures were kept in an incubator at 36.5 °C at 5 % CO_2.

Biotinylated antibody was employed to target the neuron cell membrane combined with streptavidin-conjugated GNRs as shown in Figure 19. As it has been well known that Thy-1 antigen exists as a glycosylphosphatidylinositol (GPI)-anchored protein on the surface of neuron cells [64, 65], the neuronal surface was tagged by biotinylated anti-Thy-1 antibody. GNRs covered with streptavidin are intended to bind with biotinylated antibody which is located on the surface of neuron so that GNR-mediated heat could effectively raise the temperature of the neuronal membrane.

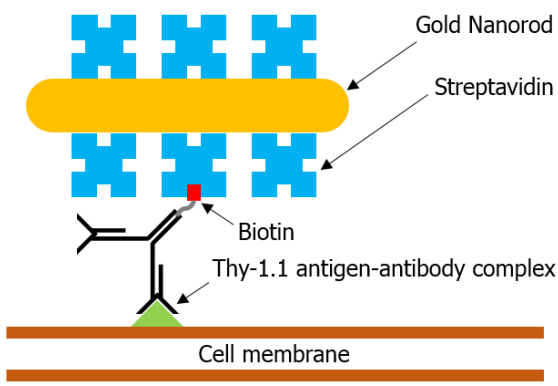

Figure 19 Schematic illustrating cell-targeted GNRs

We determined an incubation time to minimize an internalization of GNRs by living samples and to form a strong antigen-antibody reaction for stable attachment of GNRs. From the previous reports, we found that anti-Thy-1.1

antibody generally requires at least an hour to bind to the cell membrane [64, 66]. Hence, we set an incubation time of antibody-conjugated GNRs at 2 hours to realize a strong and stable attachment.

In order to verify whether streptavidin-conjugated GNRs were well bound to the cell membrane, the distribution of GNRs was visualized according to the following processes: Cultured neuron cells 18 days *in vitro* were fixed in warm 4% paraformaldehyde for 15 mins and washed with PBS three times. Subsequently, without perfusion of Triton X-100 which is a routine immunocytochemistry protocol, BSA was applied to prevent a non-reactive binding. Cells were then washed with PBS before incubating in biotinylated anti-Thy-1 antibody (554896, BD Biosciences, San Jose, CA, USA) diluted by 1:100. After washing with PBS three times, streptavidin-coated GNRs (5.1×10^{11}/mL) were added to form antibody-GNRs complex. Cells were washed three times and incubated with biotinylated FITC (B-1370, Life Technologies, Carlsbad, CA, USA) for staining. Using an inverted microscope (IX71, Olympus, Tokyo, Japan), we visualized the distribution of GNRs.

Cultures incubated in the MEA were transferred to a recording system and visualized through an inverted microscope to obtain a bright field image. We used a glass MEA (MultiChannel systems) with 30 μm diameter titanium nitride for electrode, silicon nitride for insulation layer and transparent indium tin oxide for contact pads and tracks. MEA is composed of 59 electrodes laid out in a rectangular grid with 200 μm inter-electrode spacing. Signals were pre-amplified (×1100), filtered in a bandwidth from 1 Hz to 3 kHz by MEA 1060-Inv-BC amplifier (MultiChannel Systems), and digitized using MC-Card (MultiChannel Systems). Neural signal recordings were pre-triggered for 100 ms prior to the

electrical/optical stimulation and end until 1 s. All the recorded data were analyzed using an off-line software MC-Rack (MultiChannel Systems) and filtered digitally (70 Hz highpass filter).

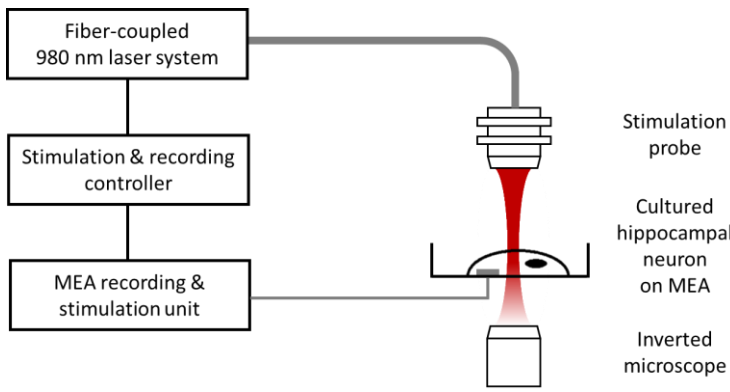

Figure 20 Experimental setup of stimulation and recording for cultured hippocampal neuron.

Prior to optical stimulation, electrical stimulation and recording were performed in advance to check the neural response to the stimuli. We produced an anodic-first biphasic current stimulation pulse of current level of 20 μA and a width of 200 μs per phase using stimulus generator STG-4008 (MultiChannel Systems). 10 stimulation pulses with a period of 60 s were delivered and the evoked responses of cultured neuron cells were recorded. Subsequently, fiber-coupled laser diode was used to optically stimulate a neuron. Accurate positioning of NIR stimulation was controlled by monitoring a visible guiding beam through optical microscope (Figure 20). After determining a stimulus area, 10 stimulation pulses with a period of 60 s and a pulse width of 400 μs were delivered and optically evoked responses are recorded. Prior to optical stimulation, the culture medium was replaced with 1.5 mL of artificial cerebrospinal fluid (aCSF, composition (in mM): 124 NaCl, 4.5 KCl, 1.2 NaH_2PO_4, 26 $NaHCO_3$, 1 $MgCl_2$, 2 $CaCl_2$, 10 Glucose with 15 mins 5% CO_2 bubbling) and maintained in the incubator (36.5°C,

5% CO_2) for 15 mins for stabilization.

2.5.2.2. Cell-targeted GNRs-mediated NIR stimulation for rat whisker control

INS evoked motor behaviors have been poorly studied to date with a lack of knowledge of effective stimulation parameters to evoke motor behaviors, contrasting with the many results of INS evoked neural activities. To demonstrate the cell-targeted GNRs can effectively initiate motor behavior, whisker region of rat motor cortex *in vivo* was selected. In the following, consideration of stimulation parameters to evoke whisker movement was taken into account. We observed the whisker behavior while changing optical stimulus parameters such as pulse duration, frequency, and number of pulses.

We performed the experiments in the following process: (i) preparation of rat, (ii) injection of GNRs to the whisker motor cortex, (iii) optical stimulation and electrical recording.

All procedures were carried out with the approval of the Institutional Animal Care and Use Committee (IACUC) of Seoul National University. Male Sprague-Dawely rats were used in this experiment. Rats were initially anesthetized with intraperitoneal injection of urethane (200 mg/kg) to find GNRs-mediated INS can induce behavior. In fact, we later found out that mixture of Ketamine/Xylazine injection was more widely used in cortically controlled motor behavior research [16, 67]. Hence in the following experiment of determining laser parametric effects on motor behavior was performed under the intraperitoneal injection of a mixture of Ketamine/Xylazine (20/6 mg/kg intraperitoneally and then supplemental dose intramuscularly as needed). The depth of anesthesia was frequently monitored by observing vibrissae movements and testing hindlimb reflex [68]. After anesthesia,

the animals were placed in a stereotaxic frame (David Kopf Instruments, Tujunga, CA, USA). A craniotomy was performed by stereotaxic coordinates ranging 2.0 mm in the anteroposterior axis and 1.5 to 2.0 mm in the mediolateral axis relative to bregma. To confirm the placement whisker-responsive sites in vibrissal primary motor cortex, an extracellular recording electrode was stereotaxically inserted into 1.0-1.2 mm from the surface of the brain (layer V).

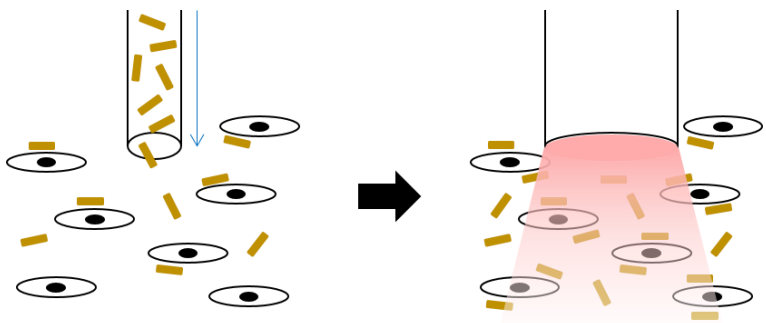

Figure 21 Illustration of GNRs injection and optical stimulation at the injection site.

After determining the exact position of motor cortex corresponding to vibrissae movement, antibody-conjugated GNRs were injected as depicted in Figure 21. Prior to injection, biotinylated anti-Thy-1.1 antibody (554896, BD Biosciences) which binds to neuronal membrane were mixed with streptavidin-coated GNRs to have a final concentration of antibody and GNRs of 0.138 μg/mL and 1.41×10^{10}/mL, respectively, with a total volume of 690 nL. Antibody-conjugated GNRs were filled in pulled glass capillary injection tip with a diameter of 75 μm (SBB-75X, Sunlight Medical) and mounted in a motorized injection system (Nanoliter 2010, World Precision Instruments) employing direct piston displacement for nanoscale injection. Precise positioning of injection tip was conducted using micromanipulator. The tip was inserted further 400 μm in depth from the target vibrissae motor cortex. After the pipette insertion, 230 nL of GNRs

were injected at a rate of 23 nL/sec. The pipette was left in place for 5 mins for solution distribution. Injection of GNRs was also conducted in an aforementioned procedure after pulling injection tip out 400 μm and 300 μm in sequence.

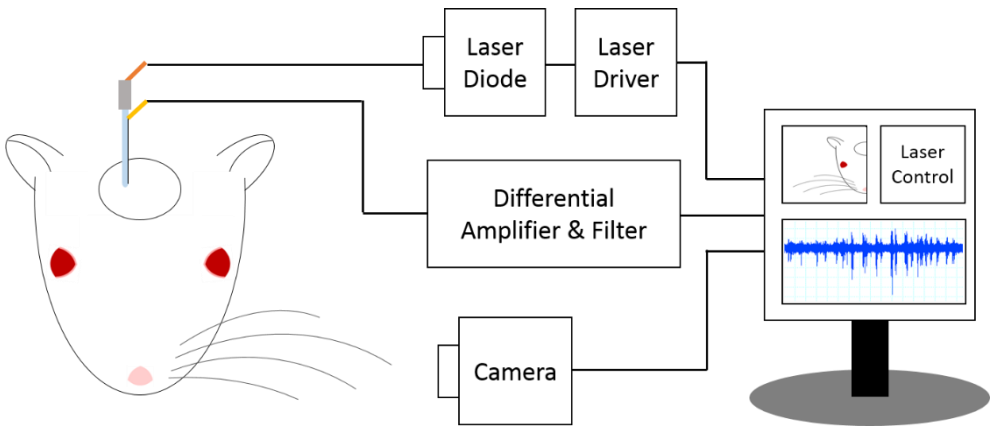

Figure 22 Illustration of optical stimulation and electrical recording of whisker region of motor cortex and video taping of whisker.

After GNRs injection, optical stimulation was performed using fiber-coupled laser system. In the experiment of finding cell-targeted GNRs can induce motor behavior, beam was focused simply outside of the brain. However, in the following study involving laser parametric effect upon motor behavior, laser was delivered inside the brain and recorded the neural signal at the exact position of laser illumination as depicted in Figure 22. Optical fiber (M84L02, Thorlabs) was directly coupled to the laser diode at the one end and 200 μm core fiber optic cannula (CFM22L20, Thorlabs) was mounted at the other end of the optical fiber in order to deliver laser pulses directly to the target. Implantation of fiber optic cannula was performed using 3-dimensional micromanipulator after injecting GNRs complex.

Electrical recording was performed to assess electrophysiological change upon optical stimulation. Customized tungsten rod electrode (diameter: 0.002 in,

AM systems) was attached parallel to the fiber optic cannula to record optically evoked neural responses (Figure 23). Neural responses were recorded with data acquisition system (Powerlab 4/20, ADInstruments, Dunedin, New Zealand) controlled using Labchart (ADInstruments) software. All recordings were captured digitally after amplifying from the preamplifier (×10) followed by differential AC amplifier (1800, AM systems) having gain of 10,000 and band-pass filter ranging from 0.1 Hz to 10 kHz and analyzed using MATLAB.

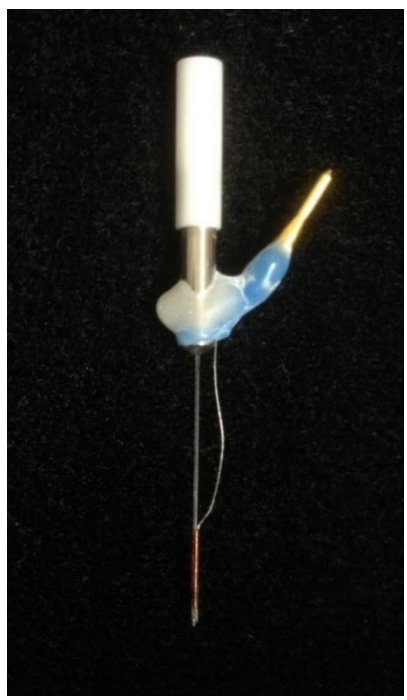

Figure 23 Picture of stimulating optical cannula with rod-type recording electrode.

Unfortunately, light induced artifact occurs when shining a light to the metal electrodes [69, 70] which seems to be associated with the ions movements due to temperature change upon light irradiation. In this study, an artifact removal technique with a curve-fitting method [71] was used to remove the artifact. After removing artifact, spike detection and sorting were performed before 1 s and after 3 s of optical stimulation. Average firing rates were calculated and compared to

quantitatively assess the effect of different stimuli.

We videotaped whisker movement using CCD camera (C920, Logitech, Lausanne, Switzerland) before 1 s and after 3 s of optical stimulation. Whisker movement was measured by reference to image pixels at fixed *x* positions in the (*x, y*) coordinate frame of the camera (to a first approximation, whisker movement is primarily in the *y* direction). The angular movement of whisker of interest was quantified in a frame-by-frame analysis using MATLAB as shown in the Figure 22.

2.5.3. Wide applicable INS

Cultured astrocyte *in vitro* and optical recording was used to verify glial cells are responsive to GNRs-mediated optical stimulation, and to show the possibility of cell-type specific multi-channel stimulation. Brief introduction of astrocyte and its modulation techniques are dealt below.

2.5.3.1. Techniques of modulating astrocyte's activities

Although astrocytes occupy a significant proportion in the central nervous system in terms of volume and population, their functions have been restricted as passive roles of supporting the network of neurons physically, creating the brain environment, building up the micro-architecture of the brain parenchyma, maintaining brain homeostasis, and controlling the development of neural cells. On the other hand, recent literatures are suggesting that astrocyte is an active participant in brain signaling and neurovascular coupling, which challenges its traditional role [72, 73]. When astrocytes are activated by external stimuli, intracellular Ca^{2+} transients or waves induce a release of neurotransmitters from a

presynaptic terminal [74, 75] and evoke an intracellular Ca^{2+} transients of neighboring astrocytes, finally leading to a release of gliotransmitters [72, 73, 76, 77]. It is interesting that those gliotransmitters are responsible for regulating the postsynaptic terminal and modulating other glial cells as well as blood vessels [72, 78].

In order to explore the physiological functions of astrocytes, dynamic modulation techniques for cytosolic calcium have been developed. While mechanical or electrical stimulation combined with a glass micropipette has been attempted [75, 79], tissue damage due to invasive insertion of glass micropipette into the brain tissue is unavoidable. Instead, optical methods have been introduced to stimulate an astrocyte as a minimally invasive approach. For example, optical uncaging technique was found to trigger intracellular Ca^{2+} responses by shining UV-light and unlocking the caged-Ca^{2+} or IP3 [80]. However, the use of caged compounds requires a periodic injection to the target region and the tissue can be damaged by UV-light exposure for uncaging the molecules.

Optogenetics techniques have been frequently used to modulate an astrocyte by expressing light-sensitive cation channels on the membrane of astrocytes [81, 82]. Although optogenetics can provide a spatiotemporally precise and controllable stimulation, it is currently unavailable for clinical use owing to imperative genetic modification. Femto-second pulsed laser is an alternative tool for stimulating astrocytes requiring neither genetic modification nor exogenous chemical compound with high spatiotemporal precision [83, 84], but it may produce significant photo-damage due to the generation of reactive oxygen species upon laser irradiation. Introduction of a pulsed infrared light to the brain cortex intrinsically evokes calcium activities consisting of fast and slow responses that

originate from the neuron and astrocyte, respectively [85]. However, it is still unclear whether the pulsed infrared light directly stimulates astrocytes when neurons and astrocytes are intermingled, indicating that direct stimulation of astrocytes is not guaranteed when they are isolated from the neurons.

Inspired by the plasmonic activation of neuron cells and the lack of studies associated with photothermal activation of astrocytes using pulsed infrared light, we demonstrated a novel optical method of direct astrocytes stimulation using surface-modified plasmonic GNRs.

2.5.3.2. Cell-targeted GNRs-mediated NIR stimulation of cultured astrocyte

We performed the experiments in the following process: (i) primary astrocyte culture, (ii) conjugation of GNRs to astrocyte membrane, (iii) optical stimulation and optical imaging.

Astrocyte cultures were prepared from cerebral cortices of Spraque-Dawley rat through a protocol modified from a previous report [76]. Briefly, cerebral cortices were isolated from postnatal (P2) rat brains under sterile conditions in accordance with the animal research guidelines of Use Committee of the Institute of Laboratory Animal Resources at Ewha Womans University (IACUC No. 15-045). Tissues were minced and dissociated using 5% trypsin-EDTA (15400, Life technologies, Carlsbad, CA, USA) after removing meninges and hippocampi. Cells were plated into a culture flask and grown in Dulbecco's modified Eagle medium (DMEM, 11995, Life technologies, Carlsbad, CA, USA) containing 10% fetal bovine serum (FBS, 16000, Life technologies, Carlsbad, CA, USA), and 1% Mycozap antibiotics (Lonza, Basel, Switzerland). After five times subcultures, cultured cells were shaken for 1 hours at 180 rpm followed by 240 rpm for 6 hours

on an orbital shaker [86] and replated in the culture flask.

Similar to the method mention in chapter 2.5.2, streptavidin-coated GNRs are delivered to the plasma membrane of the astrocytes with an aid of biotinylated antibodies. It was reported that thymocyte antigen 1 (Thy-1) exists on the surface of astrocytes in long-term cultures of rat central nervous system [87]. Biotinylated anti-Thy-1 antibody was employed to tag the surface of astrocyte and make a conjugation between antibody and GNRs through a strong biotin-streptavidin interaction.

Experiments were carried out using a home-built fiber-coupled laser system. Laser diode was modulated to generate pulses of 950 μs duration in all experiments. The position of incident laser beam having a diameter of ~400 μm was identified using a red guiding beam through optical microscope as shown in Figure 24.

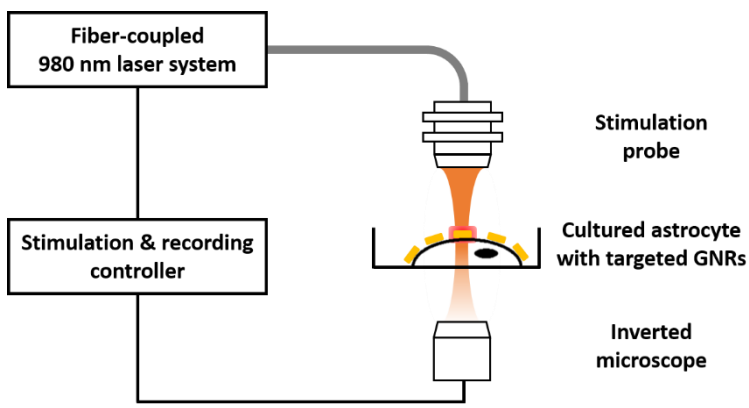

Figure 24 Experimental setup of GNRs-mediated astrocyte stimulation and calcium imaging system.

Optically evoked intracellular Ca^{2+} transients were monitored by fluorescence microscopy using the Ca^{2+} indicator Rhod-2 (R1245MP, Life Technologies, Carlsbad, CA, USA). Cells were pre-incubated in artificial cerebrospinal fluid (aCSF, composition (in mM): 124 NaCl, 4.5 KCl, 1.2 $NaH2PO_4$,

26 $NaHCO_3$, 1 $MgCl_2$, 2 $CaCl_2$, 10 Glucose with 5% CO_2 bubbling) containing 0.01 mg/mL of Rhod-2 for 15 mins. Cultures were then washed three times with aCSF prior to fluorescence imaging. Photobleaching was kept to a minimum by using low intensity excitation light while acquiring images. The fluorescence images were collected using a CMOS camera (Zyla 5.5 sCMOS, ANDOR, UK). Intracellular Ca^{2+} transients were monitored 30 s before onset of optical stimulus and 90 s after NIR stimulation and each image of 2560 × 2160 pixels is acquired with a rate of 10 frames per second.

2.6. Numerical modeling

This chapter provides the theoretical mechanisms underlying GNRs-mediated NIR stimulation. From the onset of laser irradiation to the action potentials are quantitatively discussed. In the first part, existing basic theories will be discussed. Based on these theories, light interaction with GNRs and neuron interaction with heat are modeled.

We hypothesized that heat generated from the GNRs due to the damping of LSPs affects neuronal membrane (Figure 25). Ions near the neuronal membrane redistributed upon thermal heat inducing membrane potential change. Moreover, temperature increase induces opening of temperature-sensitive ion channels resulting influx of cations. Both ion redistribution and the opening of ion channel lead membrane potential change and affect gating condition of voltage-gated ion channel. Finally, activation of ion channel lead to the generation of action potential.

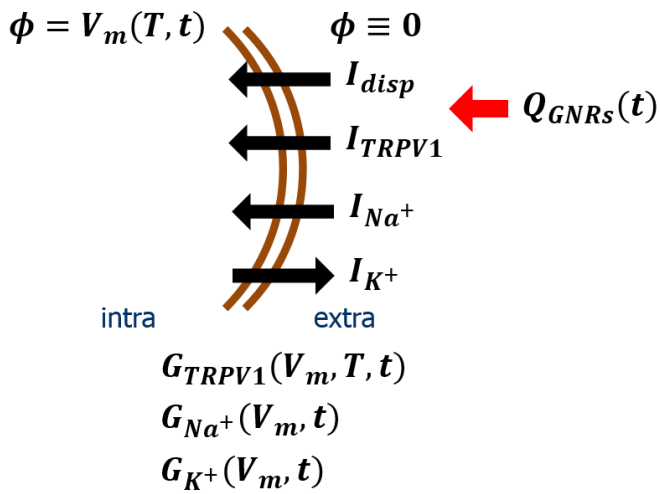

Figure 25 Mechanisms of GNRs-mediated INS.

2.6.1. Overview

The fundamental mechanisms underlying the GNRs-mediated NIR stimulation is thermal activation of neuronal membrane. A diagram in Figure 26 illustrates the mechanisms step by step. When laser is illuminated on to the GNRs, heat is generated due to the LSPs of the GNRs. Total amount of energy generated by the GNRs can be approximated using Gans theory. Heat generated from GNRs diffuse to the plasma membrane and resulting temperature elevation. The temperature profile of the plasma membrane can be numerically solved at given heat source using 1-dimensional heat diffusion equation. Temperature rise in the plasma membrane could activate temperature-sensitive ion channel and/or increase the double layer capacitance formed at each side of the lipid bilayer which in turn induce displacement current. Both result the membrane potential change (or current flow) and generate an action potential. Implementing the temperature dependent gating of the temperature-sensitive ion channel and the double layer capacitance into the classic model reported by Hodgkin and Huxley, the generation of action

potentials can be numerically simulated.

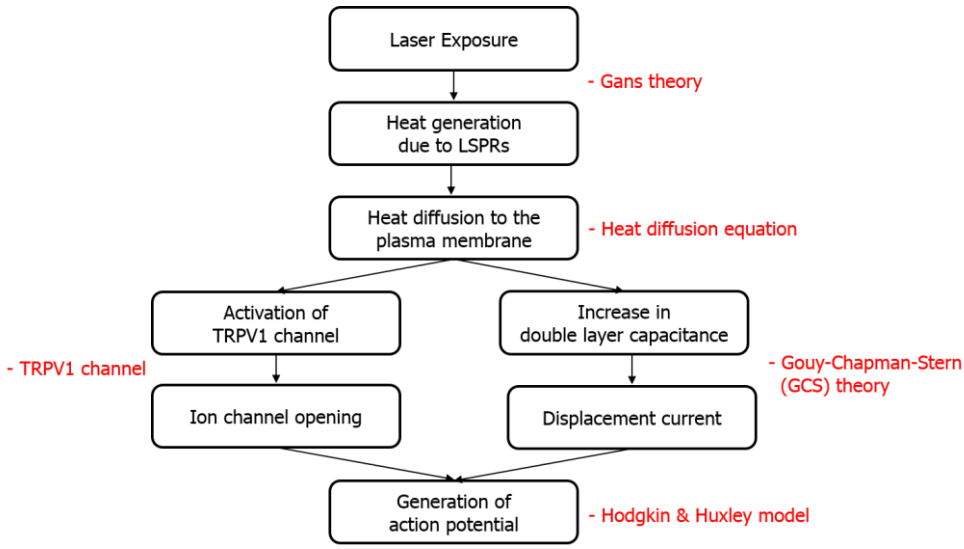

Figure 26 Mechanisms of GNRs-mediated NIR neural stimulation.

2.6.2. Background theory

2.6.2.1. Gans theory

The interaction of a particle particularly small, sub-wavelength conductive nanoparticle with an EM-field brings about electric-field amplification both inside and outside of near-field area of particle. This phenomenon is called localized surface plasmon resonance which is also concomitant enhancement in the efficiency with which a nanoparticle absorbs and scatters light [88]. The electric field enhancement of a spherical nanoparticle located at the static electric field is described as Equation 6 and Equation 7 [88].

$$\boldsymbol{E_{in}} = \frac{3\varepsilon_m}{\varepsilon + 2\varepsilon_m}\boldsymbol{E_0} \qquad \text{Equation 6}$$

$$\boldsymbol{E_{in}} = \boldsymbol{E_0} + \frac{3\boldsymbol{n}(\boldsymbol{n}\cdot\boldsymbol{p}) - \boldsymbol{p}}{4\pi\varepsilon_0\varepsilon_m}\frac{1}{r^3} \quad \text{Equation 7}$$

$$\text{where polarizability is defined as } ,\alpha = 4\pi a^3\frac{\varepsilon-\varepsilon_m}{\varepsilon+2\varepsilon_m}$$

where a is the radius of sphere, $\boldsymbol{p}$: dipole moment, $\boldsymbol{p} = \varepsilon_0\varepsilon_m\alpha\mathbf{E_0}$, and ε is the dielectric of particle, ε_m: dielectric of medium.

Absorption and scattering cross-section area due to light interaction with a homogenous sphere is also derived as Equation 8 and Equation 9 [88].

$$C_{sca} = \frac{8\pi}{3}k^4a^6\left(\frac{\varepsilon-\varepsilon_m}{\varepsilon+2\varepsilon_m}\right)^2 \quad \text{Equation 8}$$

$$C_{abs} = 4\pi ka^3\,\mathrm{Im}\left(\frac{\varepsilon-\varepsilon_m}{\varepsilon+2\varepsilon_m}\right) \quad \text{Equation 9}$$

In 1912 Gans modified the above two equations to obtain absorption and scattering cross-section area of prolate and oblate ellipsoids particle and derived Equation 10 and Equation 11 [89, 90].

$$C_{abs} = \frac{2\pi V{\varepsilon_m}^{3/2}}{3\lambda}\sum_j^3\frac{\left(\frac{1}{P_j}\right)^2\varepsilon_2}{\left(\varepsilon_1+\frac{1-P_j}{P_j}\varepsilon_m\right)^2+{\varepsilon_2}^2} \quad \text{Equation 10}$$

$$C_{sca} = \frac{8\pi^3 V {\varepsilon_m}^2}{3\lambda^4} \sum_j^3 \frac{\left(\frac{1}{P_j}\right)^2 [(\varepsilon_1 - \varepsilon_m)^2 + {\varepsilon_2}^2]}{\left(\varepsilon_1 + \frac{1-P_j}{P_j}\varepsilon_m\right)^2 + {\varepsilon_2}^2}$$ Equation 11

where V is the volume of nanoparticle, ε_m is the dielectric constant of surrounding medium, λ is the wavelength of light, ε_1 is the real part of the gold dielectric, ε_2 is the imaginary part of the gold dielectric, and P_j is depolarization factor for three axes. For spheroid nanoparticle, $P_x = P_y \neq P_z$.

$$P_z = \frac{1-e^2}{e^2}\left[\frac{1}{2e}\ln\left(\frac{1+e}{1-e}\right) - 1\right], \qquad e = \sqrt{1 - \left(\frac{B}{A}\right)^2}$$

$$P_x = P_y = \frac{1 - P_A}{2}$$

Finally, the amount of energy absorb in the GNRs upon laser illumination can be calculated using Rayleigh-Gans theory [91]. The heat absorption (Q_{abs}) in the particle is

$$Q_{ext} = \frac{C_{abs} I}{v_p}$$ Equation 12

where v_p is the volume of particle, I is the intensity with the dimensions of energy per unit area and unit time.

2.6.2.2. Heat diffusion equation

Heat equation is derived from conservation energy and Fourier's law. By simply assuming heat flow in a single direction, 1-dimensional heat diffusion equation can be obtained as Equation 13. The rate of temperature change at a specific point is proportional to the curvature of temperature with a thermal diffusivity coefficient (α).

$$\frac{\partial T}{\partial t} = \alpha \frac{\partial^2 T}{\partial x^2} \qquad \text{Equation 13}$$

From the conventional heat diffusion equation, external heat source (Q_0) is added which leads to Equation 14 where k is the thermal conductivity.

$$\frac{\partial T}{\partial t} = \alpha \frac{\partial^2 T}{\partial x^2} + \frac{Q_0}{k} \qquad \text{Equation 14}$$

2.6.2.3. Gouy-Chapman-Stern (GCS) theory

In the early 1910s researchers questioned how the charge distributed near the metal surface (e.g. metal electrode) which is soaked in the electrolyte. A major advancement was made by Gouy [92] and Chapman [93]. They independently proposed an idea of diffuse layer by using Boltzmann relation to describe the statistical distribution of ions that diffuse away from the surface [94] and Poisson equation to describe electrostatic interaction of ions near the surface. Ion concentration along the electrolyte which was statistically modeled using

Boltzmann equation was then combined with electrostatic Poisson equation to yields potential profile in the diffuse layer as Equation 15 [94].

$$\frac{\tanh\left(\frac{ze\phi}{4kT}\right)}{\tanh\left(\frac{ze\phi_O}{4kT}\right)} = e^{-\mathrm{K}x} \qquad \text{Equation 15}$$

$$\text{where, K} = \left(\frac{2n^O z^2 e^2}{\varepsilon\varepsilon_O kT}\right)^{\frac{1}{2}}$$

where ϕ is the electrostatic potential with respect to bulk solution, e is the electron charge, k is the Boltzmann constant, T is the absolute temperature, and z is the (signed) charge.

If ϕ_o is sufficiently small that ($ze\phi_o/4kT$) < 0.5, then tanh($ze\phi_o/4kT$) reduces to $ze\phi_o/4kT$ everywhere and surface potential can be approximated as Equation 16. Potential in the diffuse layer always decays exponentially away from the surface. Moreover, at larger ϕ_o whose surface is strongly charged, surface potential drops abruptly indicating diffuse layer is relatively compact. On the contrary to the large ϕ_o, potential drops gradually for the small ϕ_o.

$$\phi = \phi_O e^{-\mathrm{K}x} \qquad \text{Equation 16}$$

$$\text{where, K} = \left(\frac{2n^O z^2 e^2}{\varepsilon\varepsilon_O kT}\right)^{\frac{1}{2}}$$

Ion distribution model suggested by the Gouy and Chapman assumed ions as

a point charges which can approach to the surface infinitesimal distance. This assumption is actually unrealistic. Stern made a modification of Gouy-Chapman model while considering ions having finite radius and cannot approach to the surface closer than their radius or thickness of solvated ions. Simply envision that x_2 is a closest distance to the plane where ions can approach to the surface, potential inside the x_2 should be reconsidered while Gouy-Chapman model still applies at distance lager than x_2. The layer inside the plane at x_2 is called Helmholtz layer, where charge is not located. Since there is no charge inside the Helmholtz layer, the potential inside is linear. Therefore, linear decaying along the distance with a decaying rate equal to the slope of ϕ at x_2 as Equation 17.

$$\phi_O - \left.\frac{d\phi}{dx}\right|_{x=x_2} \times x = \phi \qquad (x \leq x_2) \qquad \text{Equation 17}$$

2.6.2.4. Hodgkin-Huxley model

Hodgkin and Huxley reported mechanisms of ionic movement underlying the generation of action potentials in the squid giant axons in 1952 [10]. They received the 1963 Nobel Prize in Physiology or Medicine for this work.

As shown in Figure 27 Hodgkin-Huxley (H-H) model describes the axon membrane as an electric circuit with four components connected in parallel. The first one is the capacitor which represents bilipid layer of the axon membrane. Sodium and potassium channels are described as variable conductance with their own electromotive force originated from the concentration difference across the membrane. Similarly, leakage component is depicted as a leak conductance and electromotive force.

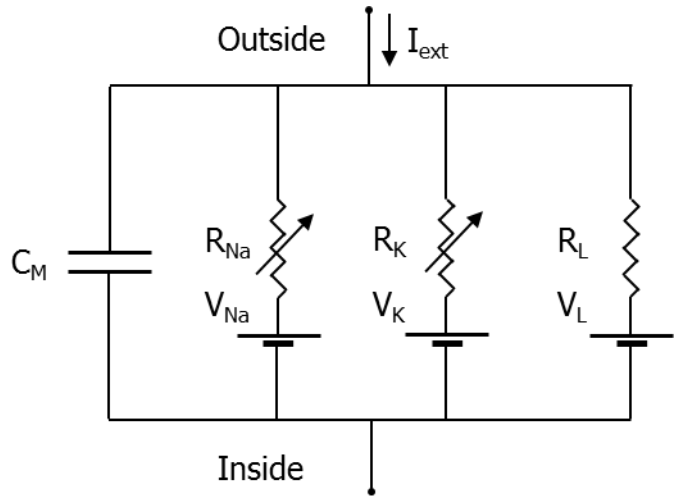

Figure 27 Electrical circuit representing axon membrane depicting lipid bilayer, sodium channel, potassium channel and leak path.

The H-H model describes the ion channels as variable conductance with respect to time and voltage. The potassium conductance is described using maximum conductance and open probability (*n*). By contrast, sodium conductance is described using the maximum conductance, open probability of activation gate (*m*) and inactivation gate (*h*). Hodgkin and Huxley empirically found the power of each open probabilities *n*, *m*, *h* and described the conductance as shown in Equation 18. The open probabilities of each *n*, *m*, *h* are calculated by rate change of each close and open state as in Equation 19. All the rate constants (α , β) were empirically derived at 6.3 ℃ as Equation 20 having Q_{10} of 3.

$$g_K = \overline{g_K} n^4 (V - V_K), \quad g_{Na} = \overline{g_{Na}} m^3 h (V - V_{Na}) \qquad \text{Equation 18}$$

$$g_{leak} = \overline{g_{leak}} (V - V_{leak})$$

$$\frac{dn}{dt} = \alpha_n(1-n) - \beta_n n, \quad \frac{dm}{dt} = \alpha_m(1-m) - \beta_m m \qquad \text{Equation 19}$$

$$\frac{dh}{dt} = \alpha_h(1-h) - \beta_h h$$

$$\alpha_n = \frac{-100(100V+6)}{\exp(-100V-6)-1} \times 3^{\frac{T-6.3}{10}} \qquad \text{Equation 20}$$

$$\beta_n = 125\exp(-12.5(V+0.07)) \times 3^{\frac{T-6.3}{10}}$$

$$\alpha_m = \frac{-100(1000V+45)}{\exp(-100V-4.5)-1} \times 3^{\frac{T-6.3}{10}}$$

$$\beta_m = 4000\exp\left(\frac{-1000(V+0.07)}{18}\right) \times 3^{\frac{T-6.3}{10}}$$

$$\alpha_h = 70\exp(50V+3.5) \times 3^{\frac{T-6.3}{10}}$$

$$\beta_h = \frac{1000}{\exp(-100V-4)+1} \times 3^{\frac{T-6.3}{10}}$$

Combining all the conductance components and capacitor component into a simple electric circuit equation lead to Equation 21.

$$\frac{I_{ext}}{A} = C_M \frac{dV}{dt} + \overline{g_K} n^4 (V - V_K) + \overline{g_{Na}} m^3 h (V - V_{Na}) + \overline{g_{leak}} (V - V_{leak}) \qquad \text{Equation 21}$$

where I_{ext} is external stimulating current and A is the current injected area.

At given externally injected current, membrane voltage (V) can be numerically calculated using above four equations; coupled ordinary differential equations (ODEs) of membrane voltage (V) and open probabilities (n, m, h). Note that, Euler method numerically solves ODEs with given initial values. For example, consider coupled differential equations with an initial value as shown in Equation 22 where $A(t)$ and $B(t)$ are unknown functions of time.

$$\frac{dA(t)}{dt} = f\big(A(t), B(t)\big), \quad \frac{dB(t)}{dt} = g\big(A(t), B(t)\big) \qquad \text{Equation 22}$$
$$A(t_0) = A_0, \quad B(t_0) = B_0$$

Euler method solves every values of $A(t)$ and $B(t)$ with increasing time t. Based on the former values of A and B from time t_n, subsequent values at time t_{n+1} are calculated using Equation 23.

$$t_{n+1} = t_n + \Delta t \qquad \text{Equation 23}$$
$$A(t_{n+1}) = A(t_n) + \Delta t \times f\big(A(t_n), B(t_n)\big)$$
$$B(t_{n+1}) = B(t_n) + \Delta t \times f(A(t_n), B(t_n))$$

Membrane potentials were numerically calculated by solving above mentioned equations using Euler method. Electrical currents were injected at 10 ms for 1 ms duration with varying amplitudes through a 10 μm diameter circle. Parameters were shown in the Table 8 and implemented HH-model using MATLAB. H-H model successfully generated action potentials when stimulating over 25 pA as shown in Figure 28.

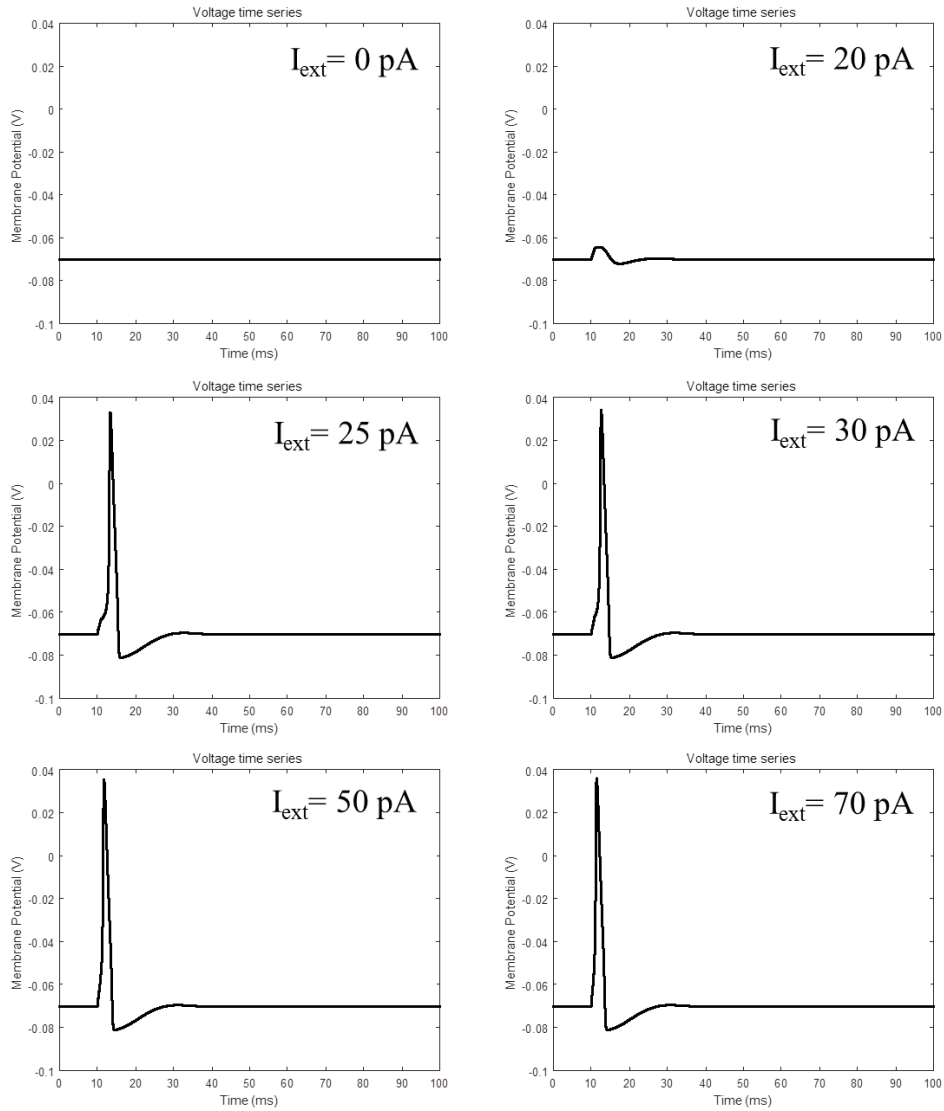

Figure 28 Membrane potentials calculated numerically using H-H method for six different external currents.

2.6.3. Laser induced heat modeling

In this chapter, temperature profile at the neuronal membrane upon laser irradiation is shown by modeling laser induced heat from GNRs. Using a Gans theory, absorption cross-section area of GNRs at the laser irradiation was calculated. Total amount energy generated from GNRs was employed to heat diffusion equation to explore the thermal profile of the plasma membrane.

2.6.3.1. Infrared light absorption of GNRs

When GNRs experience an EM-wave that matches the resonance frequency of GNRs, GNRs absorb electric field within in a region of absorption cross-section area. Gans theory, mentioned in chapter 2.6.2.1, solves the absorption cross-section area of an ellipsoidal particle. Since the shape of GNR is similar to the ellipsoid, we could approximate that the absorption cross-section area of GNR as that of the ellipsoid. As mentioned in the chapter 2.3.1, the diameter and the height of GNRs were measured as 15.3 nm and 80.4 nm, respectively. GNRs were assumed to be soaked in cerebrospinal fluid (CSF). Implementing the characteristics of GNRs at the light wavelength of 986 nm [95] and the dielectric constant of cerebrospinal fluid measured at 800 MHz and temperature of 37 ºC [96], absorption cross-section area (C_{abs}) was calculated as 1.69×10^{-16} $[m^2]$.

Substitute the value of absorption cross-section area into the Rayleigh-Gans theory and assuming the laser intensity of 286 [mJ/cm^2], as an exemplar, total heat generated from a single GNR can be approximated as 4.9064×10^{13} $[W/m^3]$.

2.6.3.2. Heat diffusion to neuronal membrane

Heat generated from the GNRs diffuses away from GNRs and reaches the plasma membrane. Figure 29 shows heat diffusion model while assuming heat flows one dimensionally. GNRs sheet having a thickness equal to the diameter of GNRs are located at 0 nm. The coverage of GNRs were determined by assuming GNRs distributed as in the section 2.3.2. Using the maximum peak temperature and the laser exposure intensity shown in Figure 13, we deduced that the coverage of

GNRs as coverage of GNRs as 0.27. However, the coverage of GNRs will be changed depending on the concentration of GNRs that bound on the membrane, and whether they clustered or not.

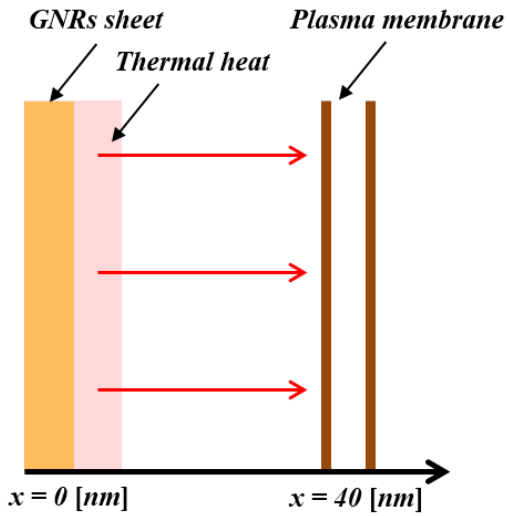

Figure 29 Model of heat diffusion from GNRs to plasma membrane.

Temperature profile of plasma membrane can be numerically calculated using 1-dimensional heat diffusion equation mentioned in chapter 2.6.2.2. Substituting the external heat source (Q_0) with the multiplication of heat generated from single GNR and a coverage of GNRs. We can solve the 1-dimensional heat diffusion equation by applying it to the Fourier and Laplace transforms [97]. Thermal conductivity of CSF was assumed as 0.57 [$W \cdot m^{-1} \cdot K^{-1}$] and the following thermal diffusivity as 1.48×10^{-7}[$m^2 \cdot s^{-1}$].

Using the laser parameters of Table 5, temperature profiles were stimulated at four different laser intensity of 166, 286, 439, 531 mJ/cm^2 as shown in the Figure 30. At the onset of laser irradiation temperature increased abruptly and reached maximum value. Temperature gradually drop to the baseline with a time

constant around 1.4 ms. It is worth noting that maximum peak temperature shows a linear dependence with laser intensity which is a result of the 1-dimensional heat flow.

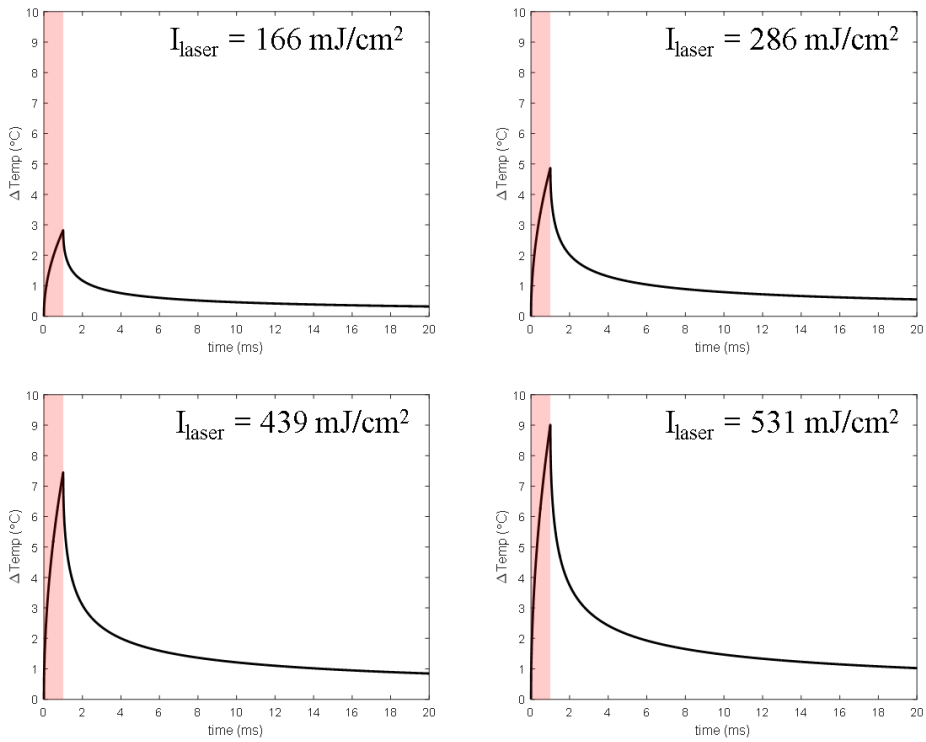

Figure 30 Temperature profiles of plasma membrane upon laser irradiation of four different laser intensities.

Table 5 Parameters of laser irradiance and heat diffusion equation.

Parameter	**Value**	**Unit**
Intensity	Variable	W
Beam diameter	600	μm
Wavelength	980	nm

Start time	0	ms
End time	1	ms

2.6.4. Neuronal membrane modeling

Laser induced temperature change was obtained in the chapter 2.6.3. In this chapter, we sought how the membrane capacitance and TRPV1 channel behave upon temperature increase.

2.6.4.1. Heat induced capacitance change

Extracellular medium vicinity of the plasma membrane (or lipid bilayer) experiences abnormal electrostatic forces compared to bulk medium. Ions in the extracellular medium redistribute to form double layer near the plasma membrane as mentioned in chapter 2.6.2.3. Needless to say, ions in the intracellular medium also redistribute and form double layer inside the membrane. Each side of the membrane is composed of a diffuse layer and a Helmholtz layer. Due to the ions redistribution of both inside and outside of the plasma membrane, potential along the intracellular medium to the extracellular medium is not uniform. Using the Gouy-Chapan-Stern theory potential along the intra- and extracellular medium can be solved, until the surface potentials of each side of the membrane is determined.

Assume, plasma membrane with a thickness δ_m positioned to separate two electrolyte solutions. Plasma membrane has a charge on internal side of the membrane ($x = -\delta_m$) and outside the membrane ($x = 0$) as σ_i, σ_o, respectively. Plasma membrane was assumed to be 1:1 phosphatidylcholine (PC) and phosphatidylethanolamine (PE) bilayer and monovalent electrolyte having 140 mM

of NaCl. Using the Gouy-Chapan-Stern theory with a modification by Genet et al [98]. Surface potential can be expressed as two coupled equations Equation 24 and Equation 25 having variables listed in the Table 6 [34]. (R represents the gas constant which is 8.31 [J·mol^{-1}·K^{-1}].)

$$\left(\sigma_o + \frac{\varepsilon_m}{\delta_m}(\Phi_i - \Phi_o)\right)^2 = 2\varepsilon_T{}^{sol}RT\sum_{j=1}^{n} c_j{}^o(\infty)\left(\exp\left(-\frac{z_j{}^oF}{RT}(\Phi_o - \Delta\Phi_s{}^o)\right) - 1\right) \quad \text{Equation 24}$$

$$\left(\sigma_i + \frac{\varepsilon_m}{\delta_m}(\Phi_i - \Phi_o)\right)^2 = 2\varepsilon_T{}^{sol}RT\sum_{k=1}^{n} c_k{}^i(-\infty)\left(\exp\left(-\frac{z_k{}^iF}{RT}((\Phi_i - V_m) - \Delta\Phi_s{}^i)\right) - 1\right) \quad \text{Equation 25}$$

$$\Delta\Phi_s{}^o = \frac{\delta_s{}^o}{\varepsilon_s{}^o}\left(\sigma_o + \frac{\varepsilon_m}{\delta_m}(\Phi_i - \Phi_o)\right) \quad \text{Equation 26}$$

$$\delta_s{}^o = \delta_{lip}{}^o + \frac{\sum_{j=1}^{n} r_j{}^o c_j{}^o(\infty)\exp\left(-\frac{z_jF}{RT}(\Phi_o - \Delta\Phi_s{}^o)\right)}{\sum_{j=1}^{n} c_j{}^o(\infty)\exp\left(-\frac{z_jF}{RT}(\Phi_o - \Delta\Phi_s{}^o)\right)}$$

$$\Delta\Phi_s{}^i = \frac{\delta_s{}^i}{\varepsilon_s{}^i}\left(\sigma_i - \frac{\varepsilon_m}{\delta_m}(\Phi_i - \Phi_o)\right) \quad \text{Equation 27}$$

$$\delta_s{}^i = \delta_{lip}{}^i + \frac{\sum_{k=1}^{n} r_k{}^i c_k{}^i(-\infty)\exp\left(-\frac{z_kF}{RT}((\Phi_i - V_m) - \Delta\Phi_s{}^i)\right)}{\sum_{k=1}^{n} c_k{}^i(-\infty)\exp\left(-\frac{z_kF}{RT}((\Phi_i - V_m) - \Delta\Phi_s{}^i)\right)}$$

Table 6 Definitions and values used to model heat induced capacitance change.

Variable	Definition	Value	Units
T	Temperature	Variable Initial temperature is 309.5 K	[K]
$\boldsymbol{V_m}$	Membrane potential (potential difference between inner and outer bulk medium)	variable	[V]
$\boldsymbol{\Phi_i}$	Surface potential of inner side of lipid bilayer	variable	[V]
$\boldsymbol{\Phi_o}$	Surface potential of outer side of lipid bilayer	variable	[V]
$\Delta\boldsymbol{\Phi_s}^{\boldsymbol{i}}$	Potential difference of inner stern (or Helmholtz) layer	variable	[V]
$\Delta\boldsymbol{\Phi_s}^{\boldsymbol{o}}$	Potential difference of outer stern (or Helmholtz) layer	variable	[V]
$\boldsymbol{\delta_s}^{\boldsymbol{i}}$	Thickness of inner stern (or Helmholtz) layer	variable	[m]
$\boldsymbol{\delta_s}^{\boldsymbol{o}}$	Thickness of outer stern (or Helmholtz) layer	variable	[m]
$\boldsymbol{\sigma_i}$	Intrinsic charge density of inner side of lipid bilayer	−0.006	[C mm^2]
$\boldsymbol{\sigma_o}$	Intrinsic charge density of outer side of lipid bilayer	−0.006	[C mm^2]
$\boldsymbol{\varepsilon_m}$	Permittivity of lipid bilayer (or plasma membrane)	$2.5 \times \varepsilon_{freespace}$	[A^2 s^4 kg^{-1} m^{-3}]
$\boldsymbol{\delta_m}$	Thickness of lipid bilayer (or plasma membrane)	3×10^{-9}	[m]
$\boldsymbol{\varepsilon_T}^{\boldsymbol{sol}}$	Permittivity of electrolyte medium	$87.740 - 0.40008t + 9.398(10^{-4})t^2 - 1.410(10^{-6})t^3$	[A^2 s^4 kg^{-1} m^{-3}]
$\boldsymbol{c_k}^{\boldsymbol{i}}(-\infty)$	Concentration of *k-th* ionic species in inner electrolyte	(0.14, 0.14)	[M]
$\boldsymbol{c_j}^{\boldsymbol{o}}(\infty)$	Concentration of *j-th* ionic species in outer electrolyte	(0.14, 0.14)	[M]

z_k^i	Valence of *k-th* ionic species in inner electrolyte	(1, −1)	-
z_j^o	Valence of *j-th* ionic species in outer electrolyte	(1, −1)	-
ε_s^i	Permittivity of inner stern (or Helmholtz) layer	$\varepsilon_T^{sol}/10$	[A^2 s^4 kg^{-1} m^{-3}]
ε_s^o	Permittivity of outer stern (or Helmholtz) layer	$\varepsilon_T^{sol}/10$	[A^2 s^4 kg^{-1} m^{-3}]
r_k^i	Hydrated ionic radius of *k-th* ionic species in inner electrolyte	(0.355,0.335) × 10^{-9}	[m]
r_j^o	Hydrated ionic radius of *k-th* ionic species in outer electrolyte	(0.355,0.335) × 10^{-9}	[m]
δ_{lip}^i	Hydrated size of inner polar lipid head groups	0.45 × 10^{-9}	[m]
δ_{lip}^o	Hydrated size of outer polar lipid head groups	0.45 × 10^{-9}	[m]

Equation 24 and Equation 25 depend on the temperature which is attributed from the temperature in Boltzmann equation and temperature dependency of electrolyte permittivity. Note that membrane surface potentials (Φ_i, Φ_o) can be solved at fixed membrane voltage (V_m) while changing temperature. Using this model, we obtained membrane surface potentials over temperature at fixed membrane potential of −100 mV as shown in Figure 31.

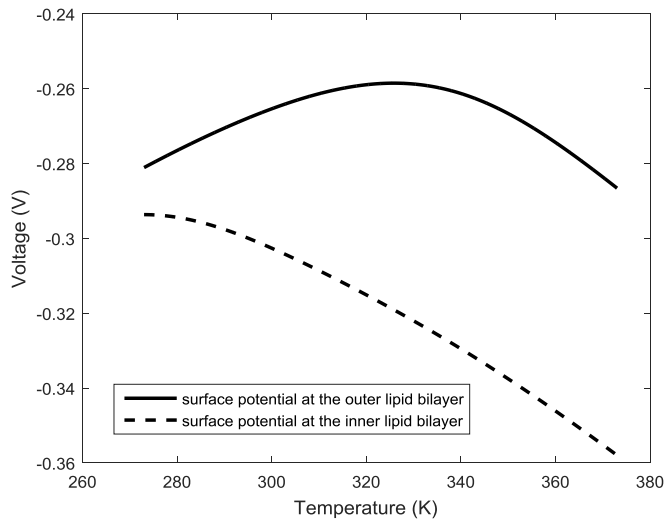

Figure 31 Graph of membrane surface potentials of inner and outer side of the lipid bilayer (plasma membrane).

Surface potentials (Φ_i, Φ_o) at the onset of laser irradiation can be obtained by matching the temperature profile after laser irradiation (Figure 30) with the standard temperature (Figure 31) to find the corresponding surface potentials of each side of the membrane. Transmembrane potential was calculated as $(\Phi_i - \Phi_o)$ and charge accumulated at the membrane was obtained by multiplication of lipid bilayer capacitance (0.01 $F \cdot m^{-2}$) and the transmembrane potential. Since membrane capacitor is equivalent to serially connected lipid bilayer and double layer capacitors of both inside and outside of the lipid bilayer, amount of charges accumulated at the membrane capacitor are same as the charges accumulated at each three capacitors components. Therefore, membrane capacitance (C_m) can be easily computed by the ratio of charge accumulated at the lipid layer and membrane potential (V_m) (Figure 32).

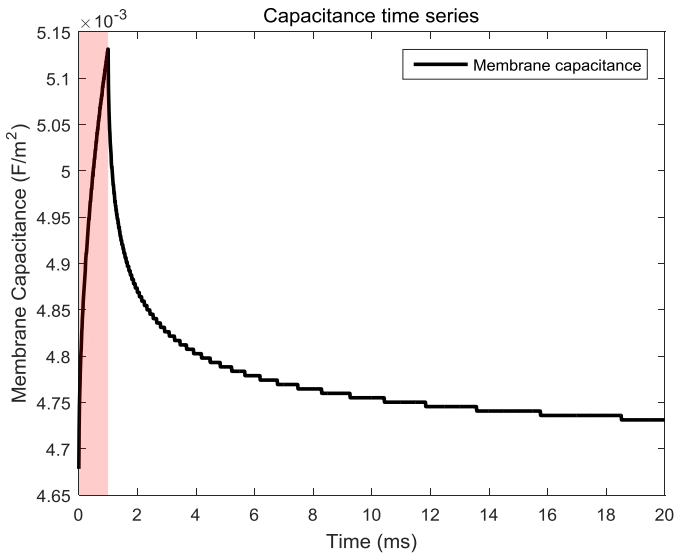

Figure 32 Membrane capacitance change when irradiating laser with an intensity of 286 mJ/cm^2.

Transient rise in membrane capacitance upon laser irradiation might be attributed to the redistribution of ions in the electrolyte of both inside and outside of the membrane. When the temperature of plasma membrane including both sides of electrolyte increases, the ions from the electrolyte move away from the plasma membrane due to the increased mobility of the ions (or increase in diffusion rates of ions). Although, both positively and negatively charged ions move away from the membrane, the amount they travel vary due to the difference in the electrostatic force exerted on each of ions. In the case where the negative membrane potential (V_m), negatively charged ions are abundant in the intracellular bulk medium. At equilibrium, charges are distributed to balance the electrostatic force between the ions. However, temperature elevation induces the movements of ions toward bulk electrolyte. The positively charged ions move more due to the attraction of bulk electrolyte compared to the negatively charged ions which are repelled. Inner surface potential decreases as shown in Figure 33 (left). As two opposite charges

being separated capacitance of inner double layer increases. Likewise, positively charged ions are abundant in the extracellular bulk medium. Hence, negatively charged ions are being attracted and move more toward the bulk medium compared to the positively charged ions. Therefore, surface potential outside of the membrane increases as shown in Figure 33 (right) with an elevation of capacitance of outer double layer. Due to the increase of both inner and outer double layer capacitance, the total double layer capacitance increases at the onset of laser irradiation.

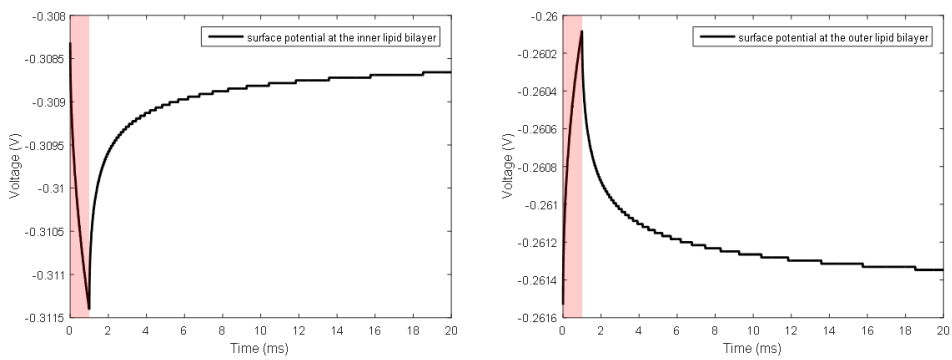

Figure 33 Profiles of surface potentials of lipid bilayer of both side; inner (left), outer (right) when laser with an intensity of 286 mJ/cm^2 was irradiated. Membrane potential (V_m) was fixed as −100 mV.

2.6.4.2. Heat induced conductance change of ion channels

Our present results shown in chapter 2.6.4.1 have important implications when considering possible mechanisms for GNRs-mediated NIR stimulation of neuron where there is no specific ion channel. In this chapter, we questioned what will happen if neuron has specific ion-channel that response to the temperature.

As we feel every day, we possess a sense of temperature. Thermosensation is mainly achieved by the thermoTRPs, a subset of transient receptor potential ion channels. Among them, heat-sensitive TRPV1 channels open above the temperature of 43 ºC. We assumed that TRPV1 channels are responsible for the

possible factors contributing the current flow through the membrane upon GNRs-mediated NIR stimulation.

The mechanisms for gating of TRPV1 channels were discovered in 2004 by Voets et al. They suspected that the temperature dependence might be originated from the thermodynamic consequence of differences in the activation energies associated with voltage-dependent channel opening and closing [37]. Given that, we could describe a TRPV1 channel as a simple two-state model for voltage-gated channel as below.

$$\textbf{Close} \underset{\beta(V,T)}{\overset{\alpha(V,T)}{\rightleftharpoons}} \textbf{Open}$$

The opening rate (α) and closing rate (β) can be described as Equation 28, Values of each parameters are shown in Table 7 [37]. Temperature coefficient for opening rate (α) and closing rate (β) are 14.8 and 1.35, respectively.

$$\alpha = \mathrm{A}\exp\left(\frac{-E_{a,open}}{RT}\right)\exp\left(\frac{\delta zFV}{RT}\right) \qquad \text{Equation 28}$$

$$\beta = \mathrm{B}\exp\left(\frac{-E_{a,close}}{RT}\right)\exp\left(\frac{-(1-\delta)zFV}{RT}\right)$$

Defining an open probability of TRPV1 as ‘r’, relation between closing and open channel can be written as Equation 29.

$$\frac{dr}{dt} = \alpha_r(1-r) - \beta_r r \qquad \text{Equation 29}$$

Open probability of TRPV1 channel (r) can be numerically solved for temperature at fixed membrane voltage −0.07 [V]. As shown in Figure 34, open probability of TRPV1 channel sigmoidally increase as temperature increase from 20 to 44 ºC. Open probability reaches near '1' when temperature becomes 44 ºC.

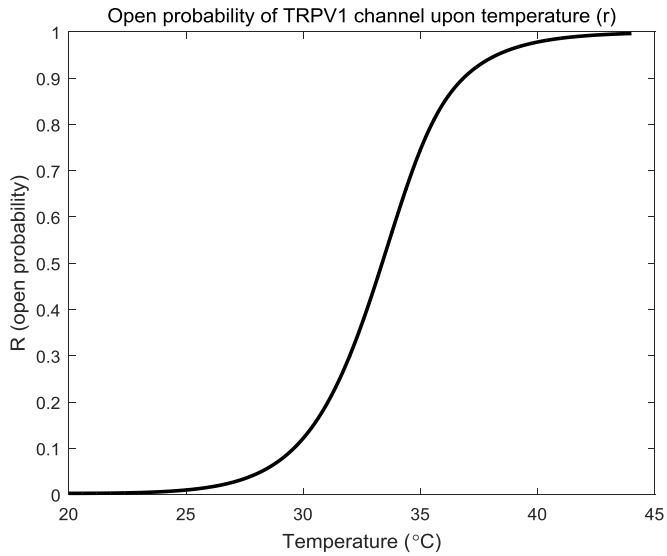

Figure 34 Open probability of TRPV1 channel upon temperature ranging from 20 to 44 ºC.

Table 7 Variables used in opening and closing rate of TRPV1 channel.

Variable	Definition	Value	Units
T	Temperature	Variable Initial temperature is 309.5 K	[K]
$\boldsymbol{V}$	Transmembrane voltage	variable	[V]
$\boldsymbol{A}$	Preexponential factor for opening rate	1.61×10^{37}	$[s^{-1}]$
$\boldsymbol{B}$	Preexponential factor for closing rate	9.67×10^{5}	$[s^{-1}]$
$\boldsymbol{E_{a,open}}$	Activation energy for opening rate	208×10^{3}	$[J \cdot mol^{-1}]$

$E_{a,close}$	Activation energy for closing rate	23.2×10^3	[J·mol^{-1}]
z	Effective charge associated with voltage-dependent gating	0.71	-
δ	Fraction of z moved in the outward direction	0.5	-
R	Gas constant	8.31	[J mol^{-1} K^{-1}]
F	Faraday constant	96500	[s A mol^{-1}]

2.6.5. Capacitance change and conductance change induced action potential

In this chapter, neuronal membrane was modeled based on a classical H-H model which considers time- and voltage-dependent sodium and potassium channels. The H-H model was modified in order to reflect the temperature dependence of the neuronal membrane. Double layers that formed at each side of lipid bilayer and temperature-sensitive ion channel were added to classical H-H model. Overall considerations underlying GNRs-mediated NIR stimulation were implemented in H-H model to verify our hypothesis is valid. As mentioned in the beginning of this chapter, starting from the laser irradiation to generation of the action potential was dealt and this chapter is the final step of this journey.

We hypothesized that GNRs-mediated NIR pulse induces local and transient heat. Transient heat near plasma membrane alters ions distribution status in the membrane resulting membrane capacitance to increase. Moreover, conductance of the TRPV1 channel increases due to the temperature elevation near the membrane. Either membrane capacitance increase or TRPV1 channel opening affect the membrane potential which is crucial in the initiation of an action potential.

Membrane potentials were easily calculated using H-H model as mentioned in the chapter 2.6.2.4. Membrane capacitance change and conductance change of TRPV1 channel were employed in H-H model and sought whether these two or independently may generate an action potential. Influence of each membrane capacitance change and the TRPV1 channel opening on the generation of an action potential were monitored and compared. We modeled three types of modified H-H models; (i) capacitance change considered H-H model, (ii) TRPV1 channel considered H-H model, and (iii) capacitance change and TRPV1 channel considered H-H model.

First, temperature-dependent capacitance change of the plasma membrane is modeled. Plasma membrane with electrical double layer of both sides can be represented by using a capacitor as mentioned in the section above. Note that membrane capacitance obtained using GCS model reflects the time-dependent temperature change rather than a constant value. Therefore, the effects of capacitance change due to rapid increase in temperature on the neural depolarization can be explored. Even though membrane capacitance is calculated at fixed membrane voltage (V_m), membrane capacitance is implemented in H-H model since membrane capacitance is same for all values of membrane voltage (V_m) [34].

Conductance of TRPV1 channel was inserted parallel to the electric circuit of classic H-H model as shown in Figure 35. Assuming the conductance of TRPV1 channel as linear function of open probability 'r', and simple electric circuit equation can be obtained as Equation 30. Note that, open probability (r) was calculated in the chapter 2.6.4.2.

$$g_{trpv1} = \bar{g}_{trpv1} \times r$$

$$0 = \frac{d(C_M V)}{dt} + \overline{g_K} n^4 (V - V_K) + \overline{g_{Na}} m^3 h (V - V_{Na}) + \overline{g_{leak}} (V - V_{leak}) + \overline{g_{TRPV1}} r (V - V_{TRPV1}) \quad \text{Equation 30}$$

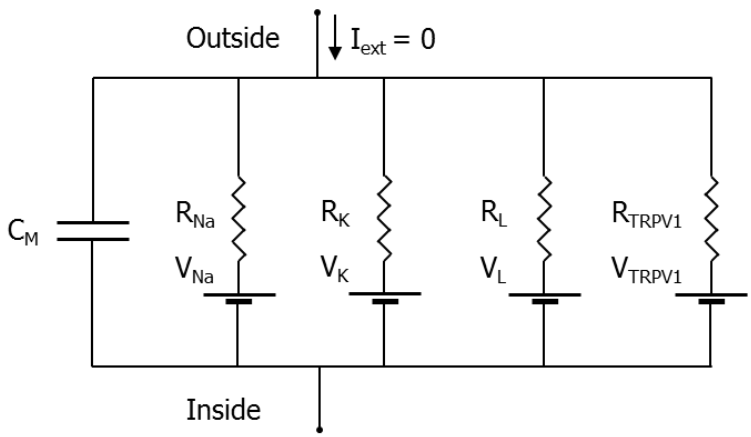

Figure 35 Electrical circuit representing axon membrane including TRPV1 channel in the classical H-H model.

Since TRPV1 channels are non-selective cation channel (or cation selective ion channel), the reversal potential was determined while considering equilibrium potentials of Ca^{2+}, Na^{+}, and K^{+}. First, equilibrium potential of Ca^{2+} ions were calculated using Nernst equation (Equation 31),

$$E_{Ca^{2+}} = \frac{RT}{zF} ln\left(\frac{C_{out}}{C_{in}}\right) \quad \text{Equation 31}$$

where, R is gas constant, T is absolute temperature, z is valance of ion, F is faraday constant, C_{out} is a concentration of ions outside of the membrane, and C_{in} is a concentration of ions inside of the membrane.

The concentration of Ca^{2+} outside of the membrane is 10^{-3} [M]. Most of the

calcium ions inside the cell are in the nucleus, mitochondria, and endoplasmic reticulum. Rest of them are in cytoplasm and only few of them are remained as free ions with a concentration of 2×10^{-7} [M] [99]. Equilibrium potential for TRPV1 channel is then 0.184 [V].

Interestingly, although TRPV1 channels is a non-selective cation channel, permeability of TRPV1 channel to each ion are not same. Ca^{2+} has biggest channel permeability and Na^{+} and K^{+} has nearly the same permeability ($\frac{P_{Ca^{2+}}}{P_{Na^{+}}} = 9.6$) [100]. Since Ca^{2+} can pass through the ion channel more easily, equilibrium potential of Ca^{2+} affects more on the reversal potential of TRPV1 channel. Therefore, reversal potential of TRPV1 channel was calculated using Equation 31, having a value of 0.195 [V].

$$V_{TRPV1} = \frac{1}{9.6}(E_{Na^{+}} + E_{K^{+}}) + E_{Ca^{2+}} \qquad \text{Equation 32}$$

Chapter 3: Results

This chapter demonstrates the results associated with GNRs-mediated NIR stimulation in order to achieve safe, effective and wide applicable INS.

3.1. GNRs-mediated safe INS

This study starts with the fact that conventional INS requires high laser exposure which might cause tissue damage due to bulk tissue heating. To overcome the high laser exposure, we employed GNRs to the conventional INS.

3.1.1. *In vivo* rat sciatic nerve

3.1.1.1. Distribution of GNRs

At first in order to confirm the presence of GNRs near the plasma membrane, we examined a histological study using transmission electron microscopy (TEM) after injecting GNRs into nerve bundle. According to Figure 36, GNRs were distributed in the vicinity of the plasma membrane of axons for local heating of the targeted nerves. Though their size and shape appear non-uniform, it was due to the fact that GNRs are randomly oriented and embedded in a three-dimensional soft tissue.

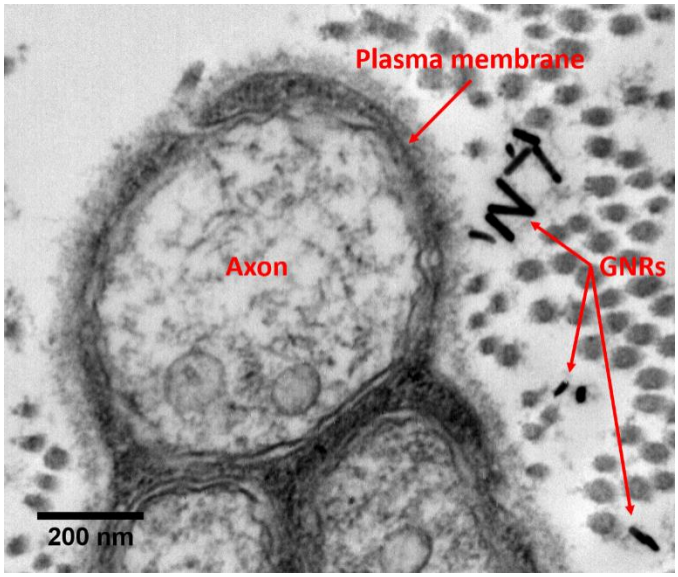

Figure 36 TEM image of GNRs injected into rat sciatic nerve.

3.1.1.2. Effect of GNRs

Subsequently, to demonstrate that a pulsed infrared stimulation elicits a neuronal depolarization, we measured CNAPs from rat sciatic nerves *in vivo* using male Spraque-Dawley rats aged 10 weeks. The sciatic nerve with a length of ~50 mm from the left thigh was exposed and the surrounding tissues were extracted before the stimulation. Fiber-coupled laser with a beam diameter of 2 mm was illuminated the proximal part of the nerve bundle where a 1 μL of GNR solution was injected in advance while extracellular electrical recording was performed at the distal end. During the experiments, optically evoked CNAPs were amplified, filtered and averaged sequentially. Figure 37 shows an exemplar of neural recording results upon the use of GNRs. While both INS strategies resulted in CNAPs under identical laser exposure of 0.641 J/cm^2, larger neural responses were produced in the presence of GNRs by more than 6 times. This clearly demonstrates that laser energy is delivered to the target tissue more effectively through its

conversion to LSP modes excited by GNRs and the resultant local heating initiates more number of neurons to be activated.

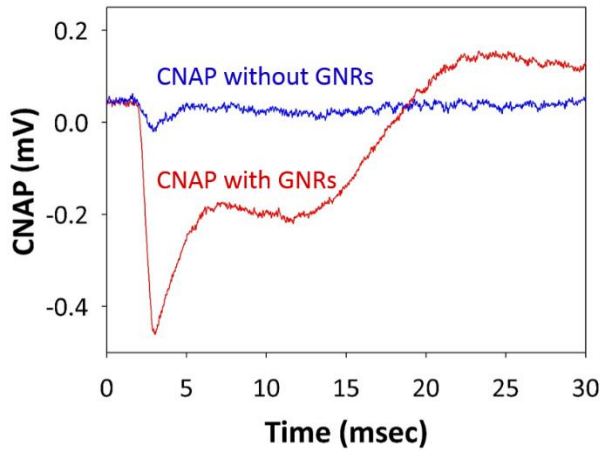

Figure 37 CNAP curves recorded when a laser pulse with an exposure energy of 0.641 J/cm^2 was irradiated to the target nerves with and without gold nanorods.

Having found out the possibility that GNR-based INS elicits evoked potentials, we investigated its effectiveness on neural activation in two aspects: responsivity and threshold. Figure 38 shows the direct comparison of CNAPs with and without GNRs as a function of laser intensity. When a laser exposure was maintained at less than 1.0 J/cm^2 to avoid damaging the plasma membrane, an increase in stimulation power causes an activation of more number of neurons and leads to a corresponding amplitude increment of CNAP signals. Figure 39 show the measured CNAP curves when rat sciatic nerves with and without GNRs were stimulated by a pulsed near infrared laser light in the range from 0.159 J/cm^2 to 1.046 J/cm^2. Of importance is that the linear regression data obtained from the case with GNR show a steeper slope by 5.7 times. It is likely that the enhanced responsivity is attributed to an effect of local heat generation which accelerates the depolarization of neuron cells inside the nerve bundles. In addition, for determining a stimulation threshold, we measured minimum laser intensity required to detect a

neural signal with an averaged magnitude of 60 μV. With an increasing laser power, stimulation thresholds were found to be 0.159 J/cm^2 for the INS with GNRs and 0.480 J/cm^2 for the one without GNRs. The latter is three times bigger than the former, which implies that the GNR-based INS is more advantageous in terms of efficiency and safety in nerve stimulation. Summarizing the results, due to a local temperature elevation by GNRs generating more neural activities and larger CNAP signals and therefore yielding an improvement in responsivity and stimulation threshold.

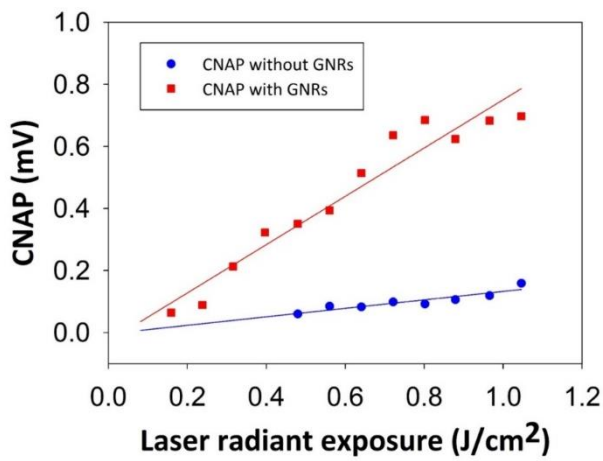

Figure 38 Graphs of laser radiant exposure versus peak amplitude of the evoked CNAP during the stimulation.

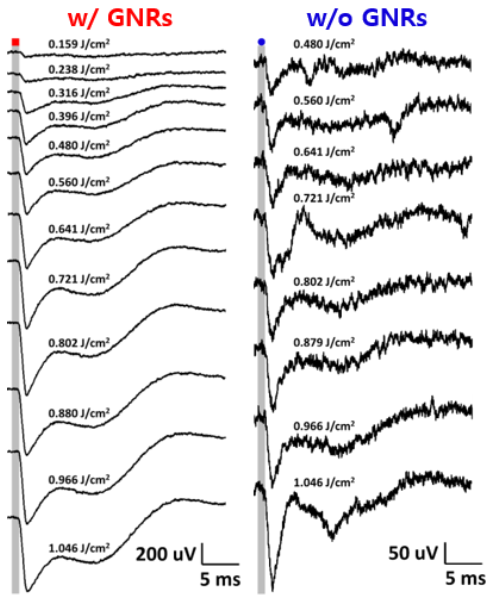

Figure 39 CNAPs recorded for different laser powers when the sciatic nerves with GNRs (left) and without GNRs (right) are stimulated.

3.1.1.3. Histological analysis

Finally, we performed the histological analysis of the sciatic nerve exposed to laser irradiation to assure our stimulation safety for the target tissues. Various radiant exposures in a wide power range were used to induce tissue damages for positive control. Twenty pulses with different radiant exposures from 0.32 J/cm^2 to 2.43 J/cm^2 were applied to the rat sciatic nerve embedded via paraffin. Serial 5 μm thick sections of the entire nerve were cut and stained with hematoxylin and eosin (H&E) to demonstrate pathological changes in the tissue. A sham procedure with no laser stimulation was also performed for negative control. Figure 40a) exhibits the histological image of cross-sectional view of rat sciatic nerve for the negative control indicating no signs of damage. On the other hand, the histological analysis in Figure 40c) for stimulation of 2.23 J/cm^2 presents a significant tissue damage, while stimulating with an exposure of 0.96 J/cm^2 causes no damage of nerve as shown in Figure 40b). Note that, in this study, we used the data obtained at an

exposure level less than 1.0 J/cm^2 to guarantee a damage-free stimulation.

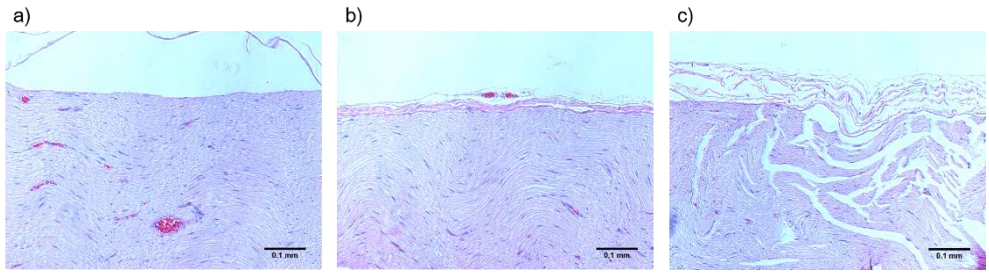

Figure 40 Histology (H&E stain) of nerve tissue upon laser exposure of various intensities. a) The sham specimen does not show any evidence of pathologic abnormality (negative control). b) The nerve irradiated at the stimulation energy of 0.956 J/cm^2 does not show any evidence of thermal damage. c) Significant histological changes in the nerve stimulated at the energy of 2.23 J/cm^2 were observed (positive control).

3.2. Cell-targeted GNRs-mediated effective INS

As mentioned in the results shown in the section 3.1, GNRs reduced stimulation threshold and guaranteed the safety. However, unbounded GNRs were readily washout due to convective extracellular fluid flow. In this study, antibody was used to bind GNRs with neuronal membrane and enhance the INS.

3.2.1. *In vitro* cultured rat hippocampal neuron

3.2.1.1. Distribution of GNRs

To verify whether streptavidin-conjugated GNRs were well bound to the neuronal membrane, the distribution of GNRs was visualized by performing immunocytochemistry. The phase contrast microscope image shows a typical hippocampal neural cell after 18 days *in vitro*. Cell bodies as well as axons can be distinguished morphologically as shown in Figure 41(a). After neuronal membrane was tagged by biotinylated anti-Thy1.1 antibody, streptavidin-coated GNRs were

incubated to form a strong binding with biotinylated antibody. Biotinylated FITC was used to observe the distribution of streptavidin-coated GNRs. Strong FITC fluorescent signal found at the surface of hippocampal neurons implies a high avidity to anchor the GNRs proximal to the neuronal membrane, avoiding diffusion of GNRs away from the target neurons (Figure 41(b)).

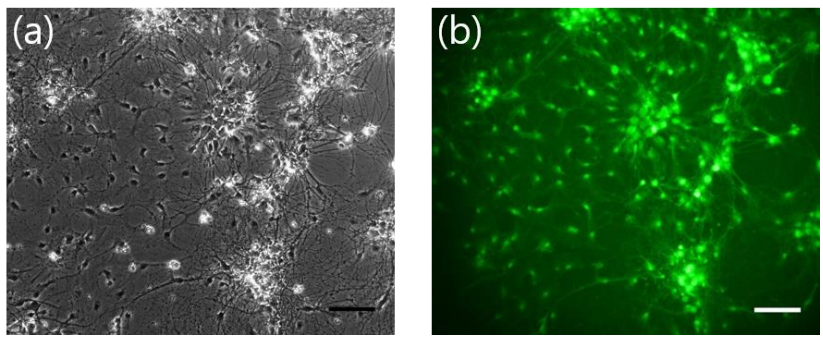

Figure 41 Phase contrast (a) and immunofluorescent microscope image after tagging antibody-conjugated GNRs with FITC to find the distribution of GNRs. Scale bar, 100 μm.

3.2.1.2. Effect of cell-targeted GNRs

Before demonstrating a neural response associated with NIR stimulation and cell-targeted GNRs, spontaneous activities of cultured neural cells were monitored. Array-wide synchronized burst activities were obtained and a time interval between bursts was presented by an inter-burst interval (IBI) histogram. In Figure 42(a), spontaneous burst firing with an average interval of 10.8 s was measured, which indicates that cultures were in the state of development of synaptic connection [62]. Electrical stimulation was delivered to the electrode where strong spontaneous activities were recorded. For electrical stimulation, a neural response was defined as a spike with a peak lower than –12 μV while neglecting the stimulation artifact that appears around 0 s. The first evoked neural response tended to appear in 10-20 ms after the electrical stimulus (Figure 42(b)). When stimulus efficiency was

defined as a percentage of the number of stimuli evoking action potentials to the total number of applied stimuli, the stimulus efficiency of electrical stimulation was measured to be 100 %, verifying a high reliability of electrical neural stimulation. Moreover, from the post-stimulus time histogram (PSTH) shown in Figure 42(c), the majority of action potentials occurred no later than 150 ms and the latency, time to get the maximum spikes after stimulus, is 25 ms.

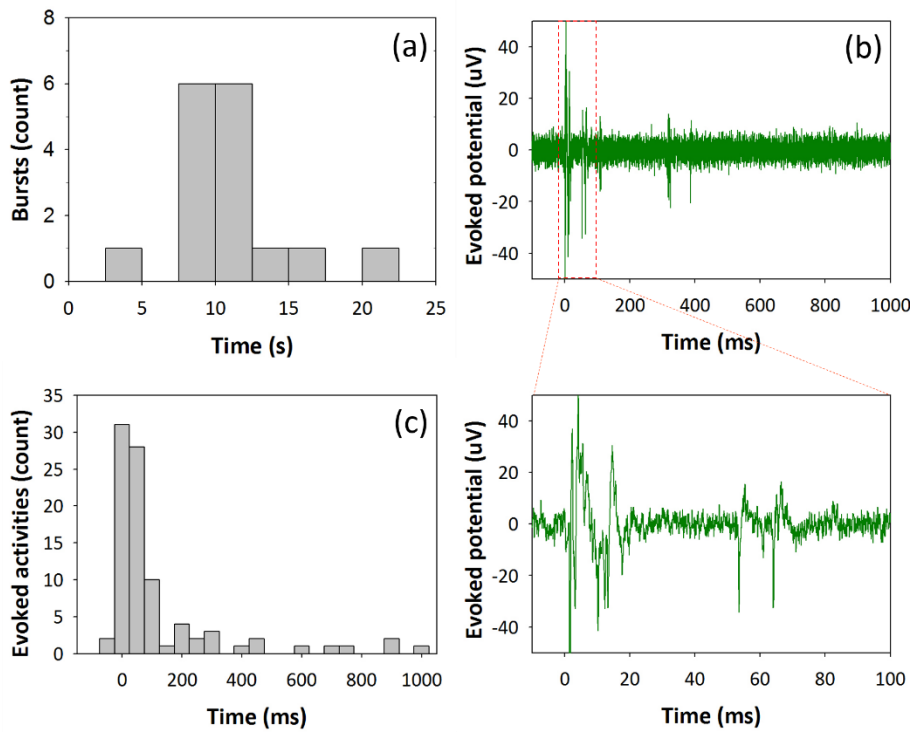

Figure 42 Characteristic of neural response upon electrical stimulus. (a) An inter-burst interval histogram without electrical stimulation. (b) Evoked action potentials after electrical stimulation. (c) A post-stimulus time histogram to show the temporal distribution of electrically evoked action potentials.

Having verified the cellular excitability upon external stimuli, optical stimulation without cell-targeted GNRs was performed. Cell medium was replaced with 1.5 mL of aCSF and culture was maintained in the incubator (36.5°C, 5% CO_2) for 15 mins. Optical pulse was delivered to the neuron for 400 μs every 60 s while

increasing its stimulus intensity to evoke neural depolarization. Note that, the data without cell-targeted GNRs in this study were assumed to include both cases for untreated GNRs and no GNRs. From the previous publication, the photosensitivity results for untreated GNRs and no GNRs showed insignificant difference in the effect of optical stimulation on DRG neurons [97]. It was also demonstrated that perfusion of fresh buffer rapidly washed the nanoparticles out, abolishing their effect. Even without active washing, diffusion of gold nanoparticles away from the neuron cell was sufficient to abolish the optical responses.

The stimulation threshold was defined as the minimum radiant exposure required to evoke action potentials with first three consecutive laser pulses while having stimulus efficiency over the 50 %. While stimulating without cell-targeted GNRs, stimulation threshold level was determined to be 46.9 mJ/cm^2 and stimulus efficiency was measured to be ~80%. In Figure 43(a), neural responses were synchronized to optical stimulus showing that optically evoked neural activities range over several hundreds of milliseconds. Due to such a wide-spreading firing distribution, the latency of PSTH was increased to 265 ms, which is approximately ten times bigger than the result of electrical stimulation of 25 ms (Figure 43(b)).

Subsequently, highly localized GNRs-mediated optical stimulation of neuron was performed by conjugating GNRs to antibodies that specifically bind to external membrane proteins. Neuronal cells were tagged with surface-modified GNRs by replacing aCSF with a cell culture medium containing a mixture of biotinylated anti-Thy-1 antibody (3.3 μg/mL) and streptavidin-conjugated GNRs (2.3×10^{11}/mL). After 2 hrs of incubation, cells were washed three times thoroughly with aCSF and incubated at 36.5°C and 5% CO_2 for 15 mins for stabilization. The neural activities were evoked as shown in Figure 43(c). The GNR-tagged neurons elicited enhanced

stimulus efficiency up to 90% at the threshold intensity of 30.1 mJ/cm^2, which was notably lower than the neurons without conjugation of GNRs. Also, the neural activities were evoked with a reduced latency of 95 ms as presented in PSTH compared to optical stimulation without cell-targeted GNRs (Figure 43(d)). Together, these data show that functionalized GNRs bound to the neuronal membrane enable fast optical neuronal depolarization with low laser intensity while displaying high resistance to washout. When GNRs are tightly bound to the membrane, it is likely that direct change in membrane capacitance and/or rapid opening of temperature-sensitive ion channels allows for a relatively faster depolarization than NIR stimulation without cell-targeted GNRs.

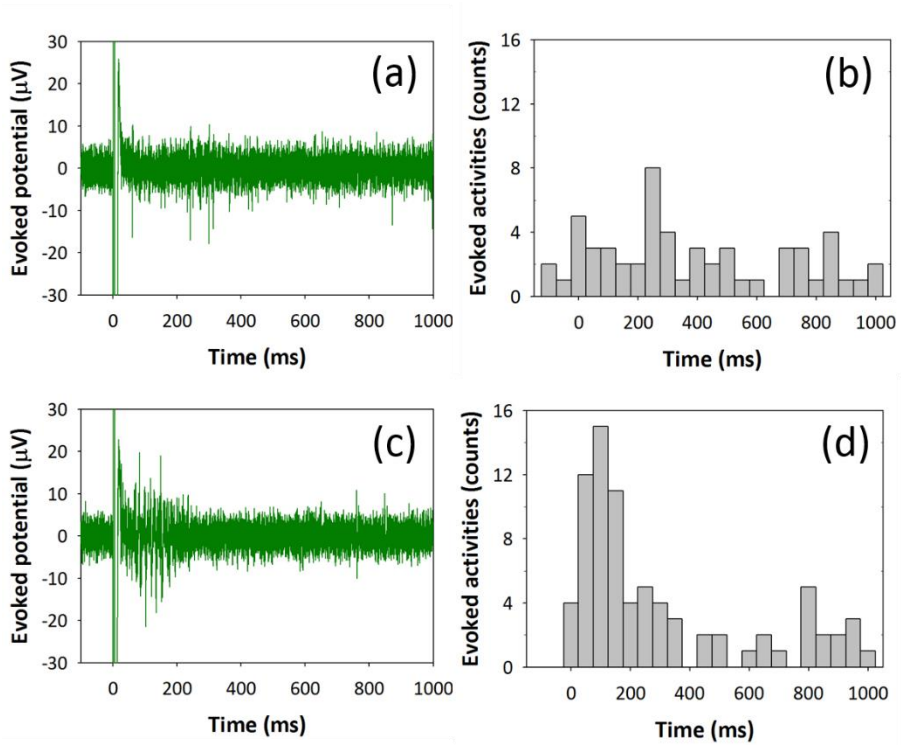

Figure 43 Characteristic of neural response upon optical stimulus with and without cell-targeted GNRs. (a) Evoked action potentials after optical stimulation without cell-targeted GNRs. (b) A post-stimulus time histogram to show the temporal distribution of optically evoked action potentials without GNRs. (c) Evoked action potentials after optical stimulation with cell-targeted GNRs. (d) A post-stimulus time histogram to show the temporal distribution of optically evoked action potentials with GNRs.

We also found the effects GNRs concentration on stimulation threshold. As mentioned in the above, GNRs concentration is the concentration during the incubation in a culture. To demonstrate the effects of GNRs on the stimulation threshold, the stimulation thresholds for the cases with GNRs and without GNRs were measured and their ratio was calculated. We defined the stimulation threshold ratio as stimulation threshold for the case with GNRs over that of the case without GNRs. As shown in Figure 44, with a concentration GNRs of 1.133×10^{11} nps/mL, the stimulation thresholds for both cases are nearly the same. However, as the GNRs concentration increases, stimulation threshold when with GNRs becomes

smaller than that of the case without GNRs as shown in Figure 44. We could speculate that much more GNRs were bound to the neuron and affect more on the neural depolarization. At the GNRs concentration of 3.4×10^{11} nps/mL, we found that stimulation threshold for the case with GNRs became half of that of the case without GNRs.

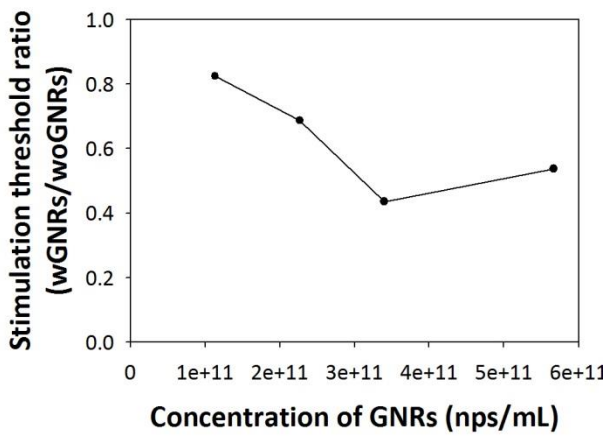

Figure 44 Graph indicating the ratio of stimulation threshold for the case with GNRs and without GNRs upon GNRs concentration.

3.2.2. *In vivo* rat motor cortex

3.2.2.1. Enhanced motor behavior using GNRs

The effect of GNRs on motor behavior was tested. As mentioned in the chapter 2.5.2.2 rats were anesthetized with intraperitoneal injection of urethane (200 mg/kg) and the optical pulses were delivered outside of the brain using fiber-coupled laser diode. Fiber is positioned ~2 mm above the brain where nanoparticles are injected. The stimulation parameters were 50 ms train of fifteen 1.5 ms pulses at 300 Hz with a pulse intensity of 128 mJ/cm^2 which were determined based on the stimulation parameter of intracortical microstimulation (ICMS) [68, 101]. After

optical stimulation, electrical stimulation (66.7 ms train of twenty monophasic, negative, 0.2 ms pulses at 300 Hz with amplitude of 2.4 mA) was delivered through tungsten microelectrode where light was delivered to check the functionality after optical stimulation [68, 101].

We found that NIR stimulation with cell-targeted GNRs facilitated a response of whisker oscillation as shown in Figure 45(a). No significant whisker angle change was observed and an exact value of simulation threshold could not be found when stimulating the motor cortex with no aid of GNRs. While the experimental results for verifying the reproducibility were not shown here, we found that overall trends were consistent, although there was slight difference in the amplitude of angle difference and the delay time to initiate the movement. To check the functionality and the cell viability of stimulation site in motor cortex, optical stimulation was followed by electrical stimulation. Strong stimulus-locked whisker movement was electrically evoked, implying that whisking function remains intact during the courses of NIR stimulation as shown in Figure 45(b). Although whisker movement triggered by optical stimulation was fairly weak and slow compared to the results of electrical stimulation, whisker movement in the presence of GNRs clearly shows an enhancement comparing to the case without GNRs.

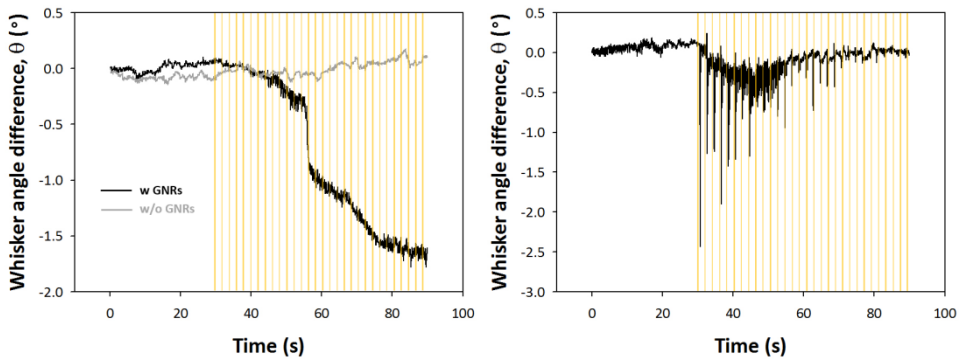

Figure 45 Whisker movement evoked by optical (left) and electrical (right) stimulation of rat vibrissae motor cortex *in vivo*.

3.2.2.2. Effects of laser stimulation parameters upon motor behavior

We demonstrated GNRs-mediated INS could induce motor behavior as shown in shown in chapter 3.2.2.1. Although laser stimulation parameters were determined based on the parameters used in ICMS, a further consideration on stimulation parameter upon motor behavior is needed.

In this experiment, rats were anesthetized with mixture of Ketamine/Xylazine and neural signals were recorded while stimulation. These two are different from the protocols used to obtain the results in the chapter 3.2.2.1. At first, we demonstrated that GNRs-mediated INS could induce whisker behavior with corresponding neural activities. When laser pulse was delivered at time 0 s with a single pulse having duration of 0.35 ms whisker was successfully moved and neural spikes were increase significantly as shown in Figure 46.

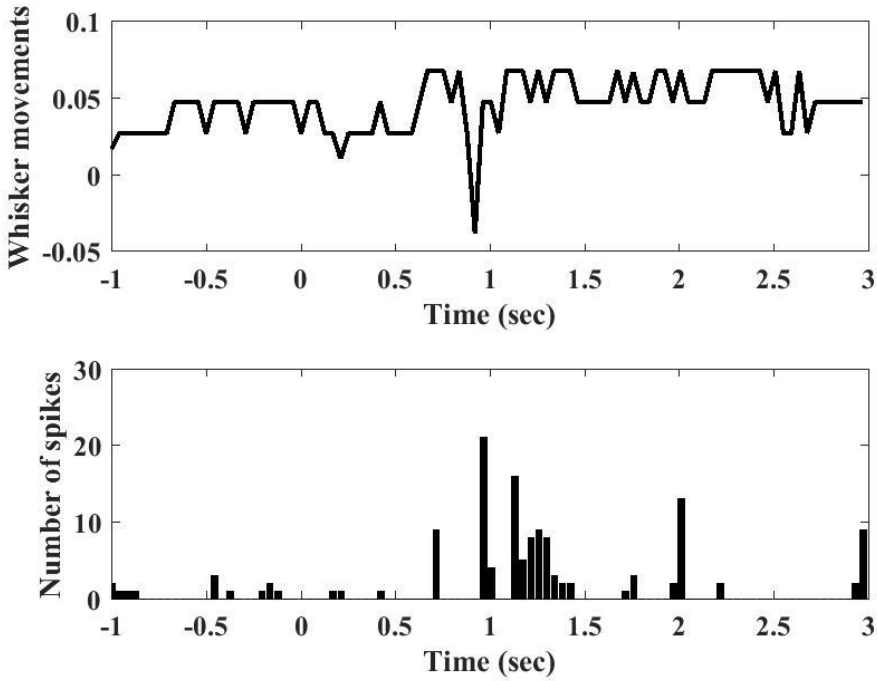

Figure 46 Whisker trajectories (top) and detected spikes from the recorded neural signal (bottom) when cortical stimulation using GNRs-mediated INS.

In order to determine the effect of stimulation parameters upon whisker movements, stimulation thresholds in which minimum radiant exposure energy of a pulse to evoke whisker behavior were determined. Effect of pulse duration on whisker movement was first determined. As shown in Figure 47, stimulation threshold energy increases as pulse duration increases. It seems that when the light energy is delivered in a short period of time, temperature increase rapidly and elicits an action potential.

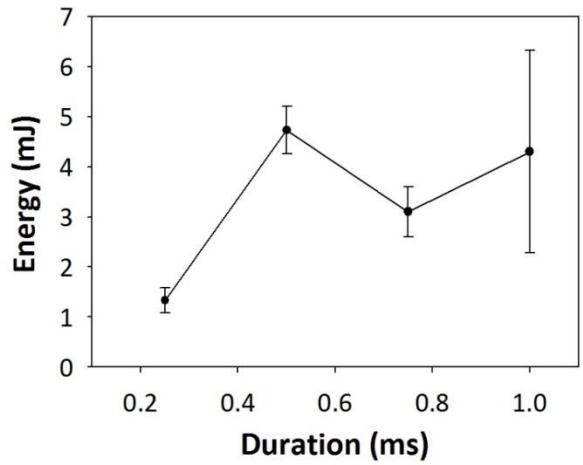

Figure 47 Plot of stimulation thresholds upon laser pulse duration. Numbers of trials for all cases were three except 0.75 ms which was two.

Effect of number of pulses upon whisker movement was determined while fixing the pulse duration at 0.25 ms. We increased the number of pulses and found out that stimulation threshold energy decreased as pulse number increased (Figure 48). It is obvious that as more pulse is delivered to the neural tissue much more light energy is accumulated to generate an action potential.

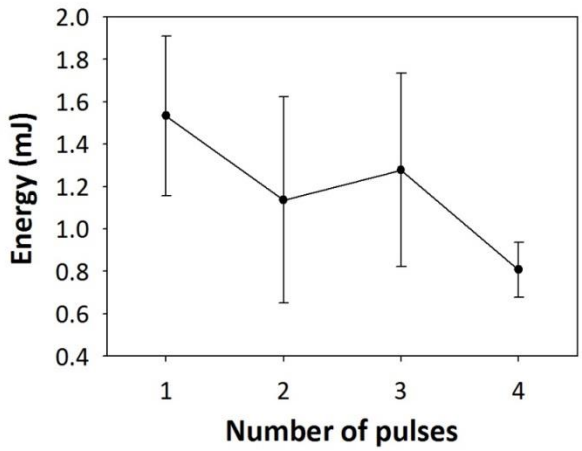

Figure 48 Plot of stimulation thresholds upon number of laser pulse. Numbers of trials for all cases were three.

Finally, laser stimulation frequency was modulated with preset pulse duration of 0.25 ms and number of pulses of four. As shown in Figure 49 stimulation threshold energy decreases as pulse frequency increases. Light energy is more likely to accumulate rather than to dissipate when the pulse frequency increases.

We determined the effects of stimulation parameters upon whisker behavior while monitoring stimulation threshold. We found that stimulation threshold decreases as pulse duration decreases, number of pulses increases, and pulse frequency increases. However, neural spikes analyses were unsuccessful since spontaneous activities were frequent in many cases which make hard to distinguish between evoked activities.

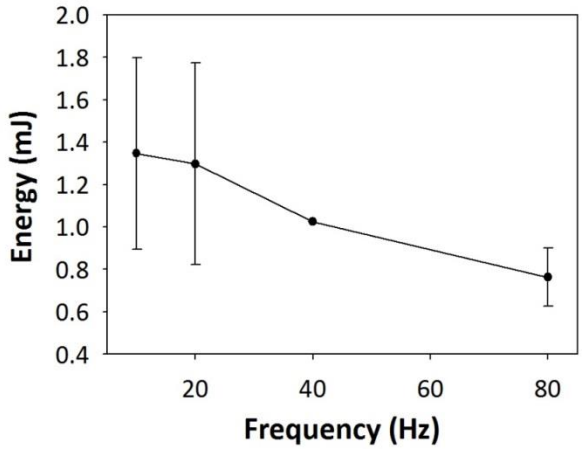

Figure 49 Plot of stimulation thresholds upon laser pulse frequency. Numbers of trials for all cases were three except 80 Hz which was two.

3.3. Cell-targeted GNRs-mediated wide applicable INS

3.3.1. *In vitro* cultured astrocyte

3.3.1.1. Astrocyte culture

Astrocyte cells from cerebral cortices of a rat were cultured and their microscopic images are shown in Figure 50. Immunofluorescence staining for glial fibrillary acidic protein (GFAP) was performed to confirm that the cultures were astrocyte confluent cells. To distinguish the morphology of individual cells, they were cultured with a low density (~150 cells/mm^2). Cells attached to the culture plate have flat, oval or irregular shape with a radially extended processes and those results were morphologically consistent with the previous works [87]. The immuno-fluorescence image in Figure 50(B) revealed that the cultured cells were GFAP-positive astrocytes, indicating that they consisted of astrocyte confluent cells while it was difficult for neurons to survive under the culture condition mentioned in the chapter 2.5.2.1.

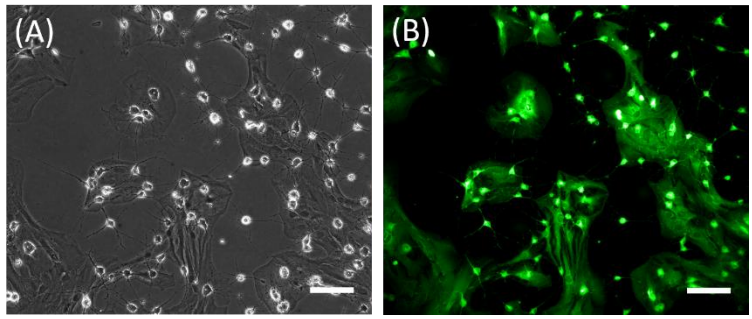

Figure 50 Microscope image of cultured astrocytes. (A) Phase contrast micrographs of cultured astrocytes. (B) Glial fibrillary acidic proteins (GFAPs) are immunocytochemically labeled. Scale bar = 100 μm in all cases.

3.3.1.2. Distribution of GNRs

Prior to photothermal stimulation of astrocytes, the distribution of GNRs were visualized to confirm that surface-modified GNRs are bound to the astrocyte. In Figure 51(B), fluorescence signals were detected in astrocytes, especially at the center of the cells. Moreover, irregular size distribution of bright spots was discontinuously observed, presenting that aggregated GNRs [97] were strongly bound to the surface. This result indicates that GNRs were successfully delivered and attached to the target astrocytes through biotin-streptavidin interaction with a strong affinity.

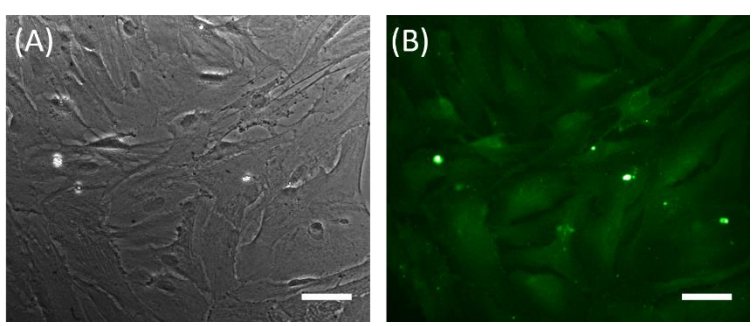

Figure 51 Microscope images of immunocytochemically stained GNRs. (A) Phase contrast microscope image of GNRs tagged astrocyte. (B) Distribution of GNRs are visualized after targeting to the cells. Scale bar = 50 μm in all cases.

3.3.1.3. Cell-targeted GNRs induced intracellular Ca^{2+} transient in astrocyte

To characterize an optically-induced Ca^{2+} transient in densely cultured astrocytes, focused NIR pulse was delivered to the astrocyte while monitoring fluorescence of Rhod-2 simultaneously before and after laser irradiation. At first, NIR stimulation without GNRs was performed using unmodified astrocytes. After pinpoint irradiating NIR pulse of 13.12 mJ/mm^2 to astrocyte, no significant Ca^{2+} wave was monitored as shown in Figure 52. Fluorescence change ($\Delta F/F_0$), the difference in fluorescence intensity at the onset of the stimulus and maximum fluorescence intensity after stimulation, was obtained as small as 1.1%, implying that astrocyte was not affected by the pulsed NIR stimulation when it was stimulated without cell-targeted GNRs.

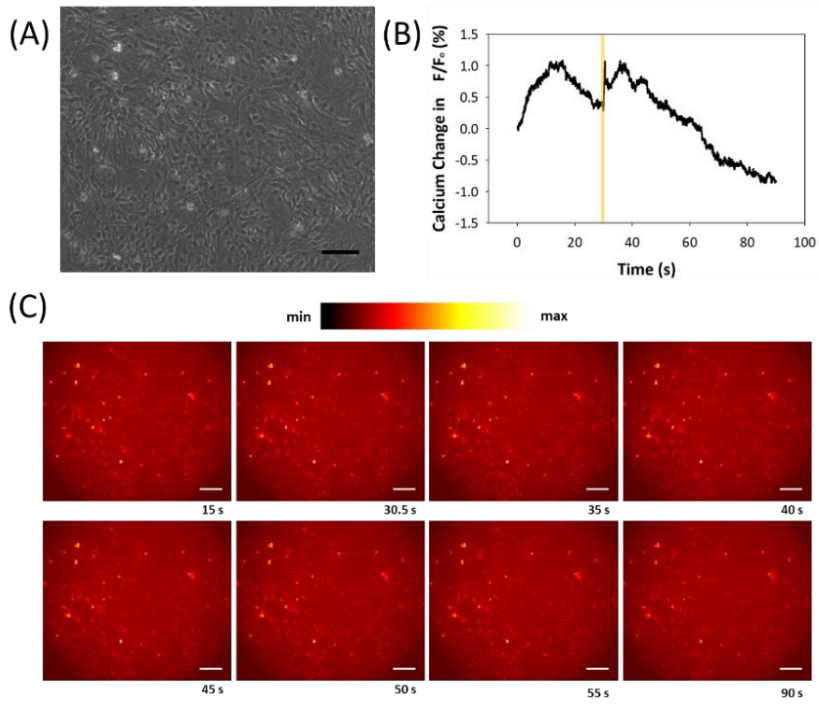

Figure 52 Characterization of NIR stimulation without cell-targeted GNRs. (A) Phase contrast microscope image of astrocyte. (B) Profile of intracellular Ca^{2+} waves before and after optical pulse (yellow box). (C) Ca^{2+} images at 15, 30.5, 35, 40, 45, 50, 55, 90 s. Scale bar = 100 μm in all cases.

Subsequently, optical stimulation with cell-targeted GNRs was examined. GNRs were bound to cell membrane to generate highly localized thermal transient and to resist extracellular fluid flows. Astrocytes were tagged with surface-modified GNRs by incubating with a mixture of biotinylated anti-Thy-1 antibody (5 μg/mL) and streptavidin-coated GNRs (3.4×10^{11}/mL). Cells were then washed three times thoroughly with aCSF and loaded with Ca^{2+} indicator Rhod-2. In Figure 53, at the onset of NIR irradiation of 13.12 mJ/mm^2, fluorescence intensity reached a maximum of 85.1% within 11 s, which was obviously different from spontaneous Ca^{2+} oscillation. Strong intracellular Ca^{2+} transient with an average fluorescence change ($\Delta F/F_0$) of 79.7% was observed. Fast propagation of Ca^{2+} waves both within and between astrocytes was measured with an average propagation velocity

of 20.1 μm/s, which was consistent to the physiological Ca^{2+} activity in the previous literatures [79, 102]. Accordingly, NIR stimulation with targeted GNRs could trigger intracellular Ca^{2+} elevation while the stimulation without GNRs did not induce any noticeable Ca^{2+} change, implying that a combination of GNRs with NIR pulse was effective in generating intracellular Ca^{2+} transient.

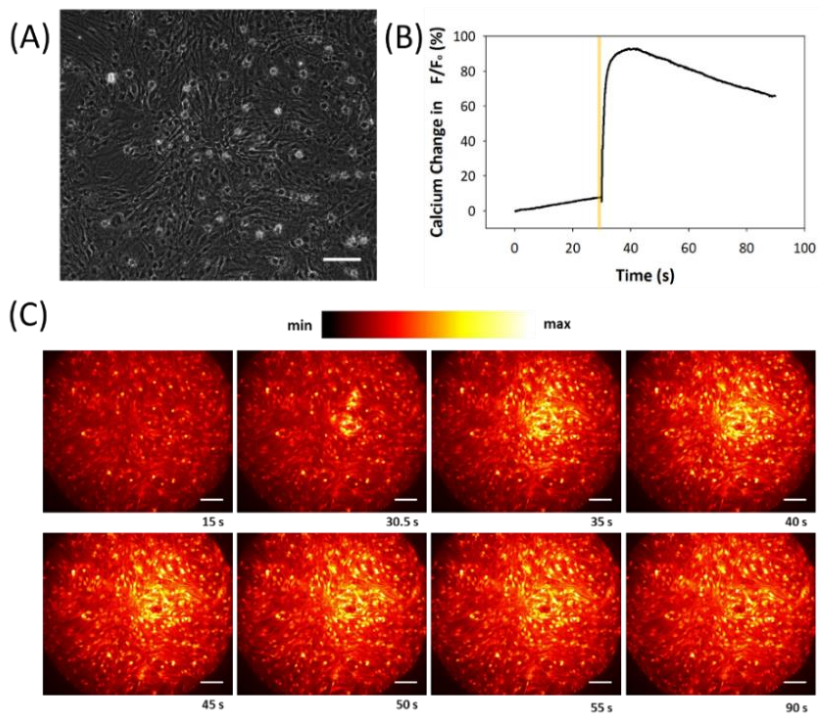

Figure 53 Characterization of NIR stimulation with cell-targeted GNRs. (A) Phase contrast microscope image of astrocyte. (B) Profile of intracellular Ca^{2+} wave before and after optical pulse (yellow box). (C) Ca^{2+} images at 15, 30.5, 35, 40, 45, 50, 55, 90 s. Scale bar = 100 μm in all cases.

In order to causally understand the origin of intracellular Ca^{2+} transients upon infrared laser stimulation, optical stimulation was performed under Ca^{2+}-free aCSF medium (composition (in mM): 124 NaCl, 4.5 KCl, 1.2 NaH_2PO_4, 26 $NaHCO_3$, 3 $MgCl_2$, 10 Glucose with 5% CO_2 bubbling). The experiments were conducted after targeting GNRs to the cell surface. As shown in Figure 54, NIR

stimulation of 13.12 mJ/mm^2 combined with GNRs still induced an abrupt and stimulus-triggered Ca^{2+} elevation and subsequent Ca^{2+} propagation to neighboring cells with an average fluorescence change ($\Delta F/F_0$) of 56.5%. Average propagation velocity of 18.9 μm/s matches the values observed for the stimulation of cells incubated in Ca^{2+} contained medium. The results showed that Ca^{2+} from the extracellular medium was not dominant to generate intracellular Ca^{2+} transients upon optical stimulation. However, intracellular Ca^{2+} elevations were increased when astrocytes were incubated in the Ca^{2+} contained medium compared to the Ca^{2+} elevations when stimulating in the absence of extracellular Ca^{2+} ions. The difference in the Ca^{2+} elevation appears to originate from the absence of Ca^{2+} influx from extracellular medium, suggesting that not only an influx of Ca^{2+} from extracellular medium but also a release of Ca^{2+} from intracellular Ca^{2+} in store contributes to Ca^{2+} transients in astrocyte cells after optical stimulation.

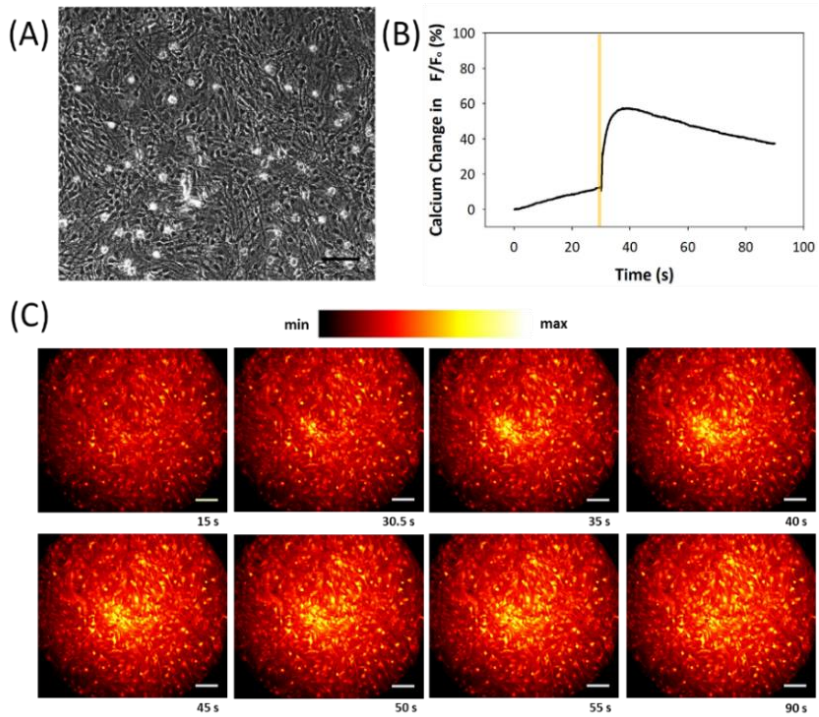

Figure 54 Characterization of optical stimulation with cell-targeted GNRs when cell are incubated in Ca^{2+} free aCSF medium. (A) Phase contrast microscope image of astrocyte. Optical pulse is given at the center of the culture. (B) Profile of intracellular Ca^{2+} wave before and after optical pulse (yellow box). (C) Ca^{2+} images at 15, 30.5, 35, 40, 45, 50, 55, 90 s. Scale bar = 100 μm in all cases.

It has been reported that TRPV channels are highly expressed in astrocyte cells of a cell plasma membrane including cytoplasm [103, 104]. Upon NIR irradiation, localized heat generated from GNRs elevates a local temperature increase to open TRPV channels in the cell plasma membrane and cytoplasm, which in turn induces intracellular Ca^{2+} transient [105]. It is also possible that a membrane potential change due to displacement current might lead to an activation of voltage-gated Ca^{2+} channels (VGCC) and induce an influx of calcium ions [106]. Initiation of intracellular Ca^{2+} increase from either TRPV channel or VGCC leads to an additional Ca^{2+} amplification by Ca^{2+}-induced Ca^{2+} release mechanism from internal Ca^{2+} stores such as endoplasmic reticulum [107]. Regarding the possible mechanisms of INS, it is presumable that thermal heat is responsible for the

intracellular Ca^{2+} transient upon GNRs-mediated NIR stimulation of astrocyte.

Since the astrocyte respond to optical stimulus through transient heat accumulation near the internal Ca^{2+} stores, there need strong laser stimulus. Recall that GNRs are bound to the plasma membrane outside of the cell, high laser exposure energy is required to raise the temperature near the internal Ca^{2+} stores and stimulation of astrocyte might result tissue damage.

3.4. Numerical analysis

GNRs-mediated NIR stimulation of neuron was modeled as shown in the chapter 2.6. We found out that GNRs-mediated NIR pulse generated local temperature jump at the plasma membrane resulting sudden increase in the membrane capacitance and the opening of TRPV1 channel. Moreover, the minimum laser intensity required to generate an action potential was simulated to give an insight of GNRs-mediated NIR stimulation. In this chapter, we numerically calculated whether these changes could generate an action potential which is the final step of the journey.

3.4.1. Numerical analysis using capacitance change considered H-H model

At first, H-H model was modified aiming to consider capacitance change upon laser illumination. Capacitance change obtained in chapter 2.6.4.1 was implemented into H-H model which was a constant value in a classical H-H model. Without externally injected current, we simulated whether capacitance change could trigger an action potential upon laser irradiation. We found that photothermal

effect of GNRs was able to deliver heat to induce transient capacitance increase which was sufficient to induce displacement current for the generation of action potential. Stimulation threshold was defined as the minimum laser intensity required to evoke an action potential. The stimulation threshold for the GNRs-mediated INS while considering the capacitance change was determined as 439 [mJ/cm^2]. Moreover, as laser intensity above the stimulation threshold increases, time to reach the peak potential becomes shorter as shown in Figure 55.

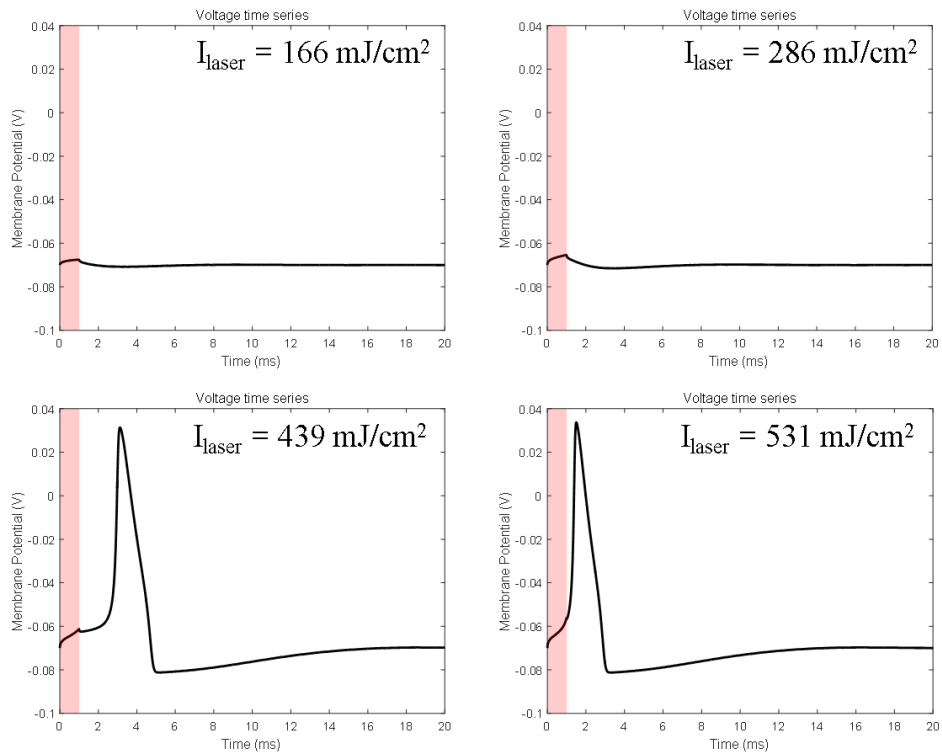

Figure 55 Graphs indicating action potentials upon four different laser intensities obtained by simulating the modified H-H model. Capacitance change was employed in the H-H model.

3.4.2. Numerical analysis using TRPV1 channel considered H-H model

In this chapter, the effect of TRPV1 channel on the generation of the action potential was determined while membrane capacitance was fixed to a constant

value. A resistor of TRPV1 channel was inserted parallel to the electric circuit of classic H-H model. Numerically solving the Equation 30 using the parameters shown in Table 8, we found that TRPV1 channel alone could triggers neural depolarization and finally generates an action potential as shown in Figure 56. The stimulation threshold was found as 286 [mJ/cm^2] and the time to reach the peak potential gets shorter as increasing the laser intensity.

Interestingly, an action potential initiated at least ~6 ms after the optical stimulus at the threshold value which was delayed by comparing to the results obtained using electrical stimulation (~0 ms) and using optically induced capacitance change (~2 ms). We speculated that delayed response is due to the small conductance of TRPV1 channel. Although, open probability of TRPV1 channel increases abruptly at the onset of laser irradiation, membrane potential increases gradually due to the small inward current through the TRPV1 channel. Therefore, considerable time was required to reach the threshold potential (~−0.06 [V]) for the generation of action potential. When the membrane potential approaches the threshold potential, the conductance of the TRPV1 channel increases abruptly (second peak) and support the generation of the action potential as shown in Figure 56. The stimulation thresholds obtained using the membrane capacitance considered H-H model and the TRPV1 channel considered H-H model are 439 and 286 [mJ/cm^2], respectively. Since the TRPV1 channels considered H-H model responded to the optical stimulus at lower exposure energy compared to the capacitance considered H-H model, we could speculate that TRPV1 channel affect more on the mechanism involving GNRs-mediated INS.

Table 8 Variables used in the modified H-H model.

Variable	Definition	Value	Units
T	Temperature	Variable Initial temperature is 309.5 K	[K]
$\boldsymbol{V}$	Transmembrane voltage	Variable Initial voltage is -0.07 V	[V]
$\boldsymbol{n, m, h, and\ r}$	Open probability of each gate	variable	-
$\boldsymbol{\alpha_{n/m/h/r}}$	Opening rate of specific gate	variable	[s^{-1}]
$\boldsymbol{\beta_{n/m/h/r}}$	Closing rate of specific gate	variable	[s^{-1}]
$\boldsymbol{C_M}$	Membrane capacitance per unit area	variable initial value is 1×10^{-3}	[$F \cdot m^{-2}$]
$\boldsymbol{\overline{g_K}}$	Maximum conductance of potassium channel	360	[$S \cdot m^{-2}$]
$\boldsymbol{\overline{g_{Na}}}$	Maximum conductance of sodium channel	1200	[$S \cdot m^{-2}$]
$\boldsymbol{\overline{g_{leak}}}$	Maximum conductance of leak current	3	[$S \cdot m^{-2}$]
$\boldsymbol{\overline{g_{TRPV1}}}$	Maximum conductance of TRPV1 channel	0.3 ref) [108]	[$S \cdot m^{-2}$]
$\boldsymbol{V_K}$	Equilibrium potential of potassium channel	-0.012	[V]
$\boldsymbol{V_{Na}}$	Equilibrium potential of sodium channel	0.115	[V]
$\boldsymbol{V_{leak}}$	Equilibrium potential for the passive leakage	0.0106	[V]
$\boldsymbol{V_{TRPV1}}$	Equilibrium potential of TRPV1 channel	0.195	[V]

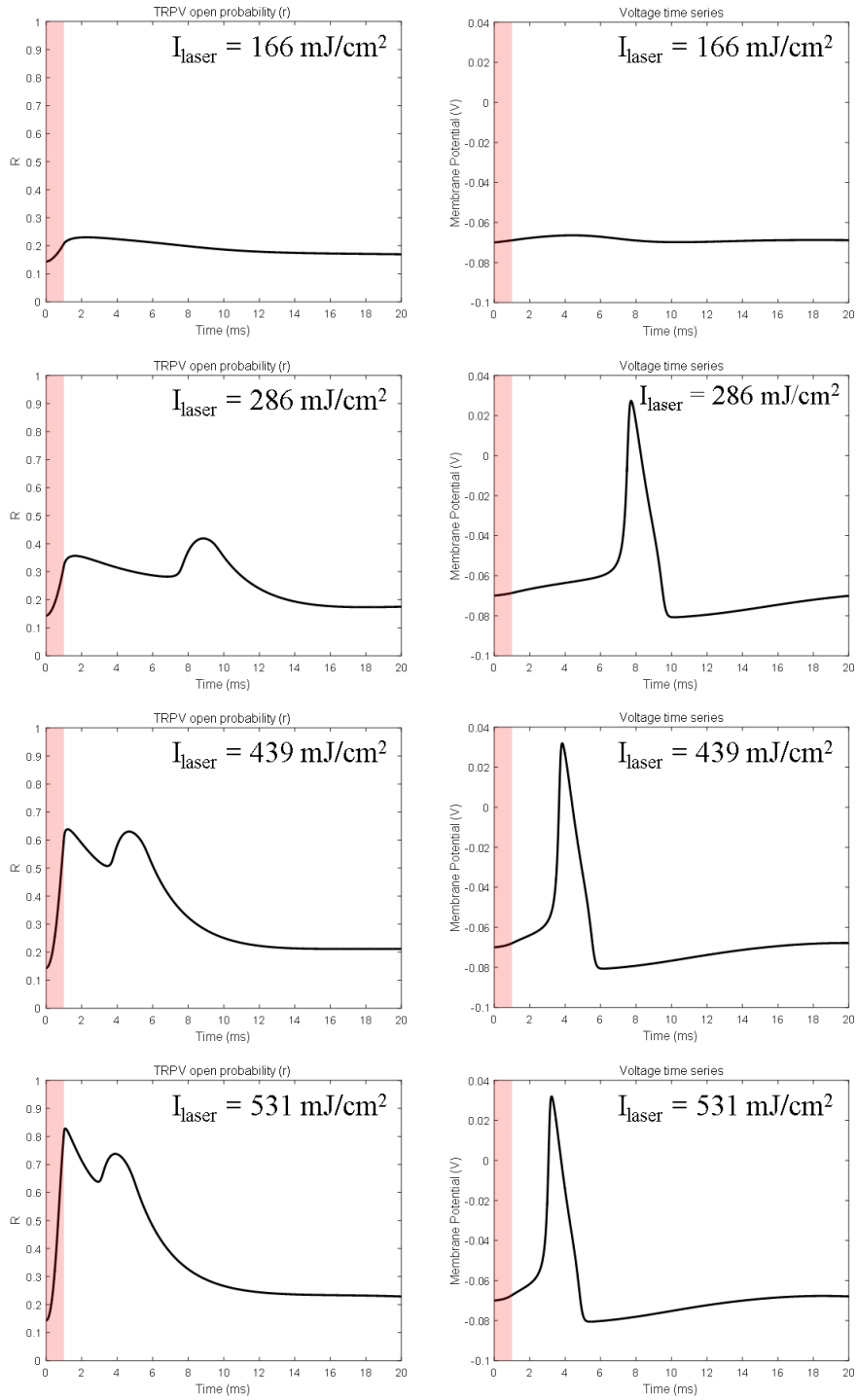

Figure 56 Graphs indicating open probabilities of TRPV1 channel and corresponding action potential for four different laser intensities. All the plots were obtained from the modified H-H model where conductance of TRPV1 channel was considered while membrane capacitance was kept fixed.

3.4.3. Numerical analysis using capacitance change and TRPV1 channel considered H-H model

In fact, both the capacitance change and the TRPV1 channel contribute the generation of action potential when GNRs-mediated NIR stimulation of neuron. Though, in some nervous system such as peripheral nerves do not have TRPV1 channel, it is reasonable to consider both effects. In this section, we implemented both the TRPV1 conductance factor and the membrane capacitance factor in the H-H model.

We simulated whether GNRs-mediated INS could induce an action potential via combination of the transient capacitance increase and the opening of the TRPV1 channel. The action potential was successfully generated with a stimulation threshold of 166 [J/cm^2] as shown in Figure 57. Intriguingly, the stimulation threshold was lowered compared to that obtained using the membrane capacitance considered H-H model (439 [J/cm^2]) and the TRPV1 channel considered H-H model (286 [J/cm^2]). Reduced stimulation threshold might be originated from the increase in the inward current due to the combination of both current from membrane capacitance increase and opening of TRPV1 channel. These results indicate that GNRs-mediated NIR stimulation of sciatic nerve requires higher laser intensity compared to the hippocampal neuron where TRPV1 channels are present.

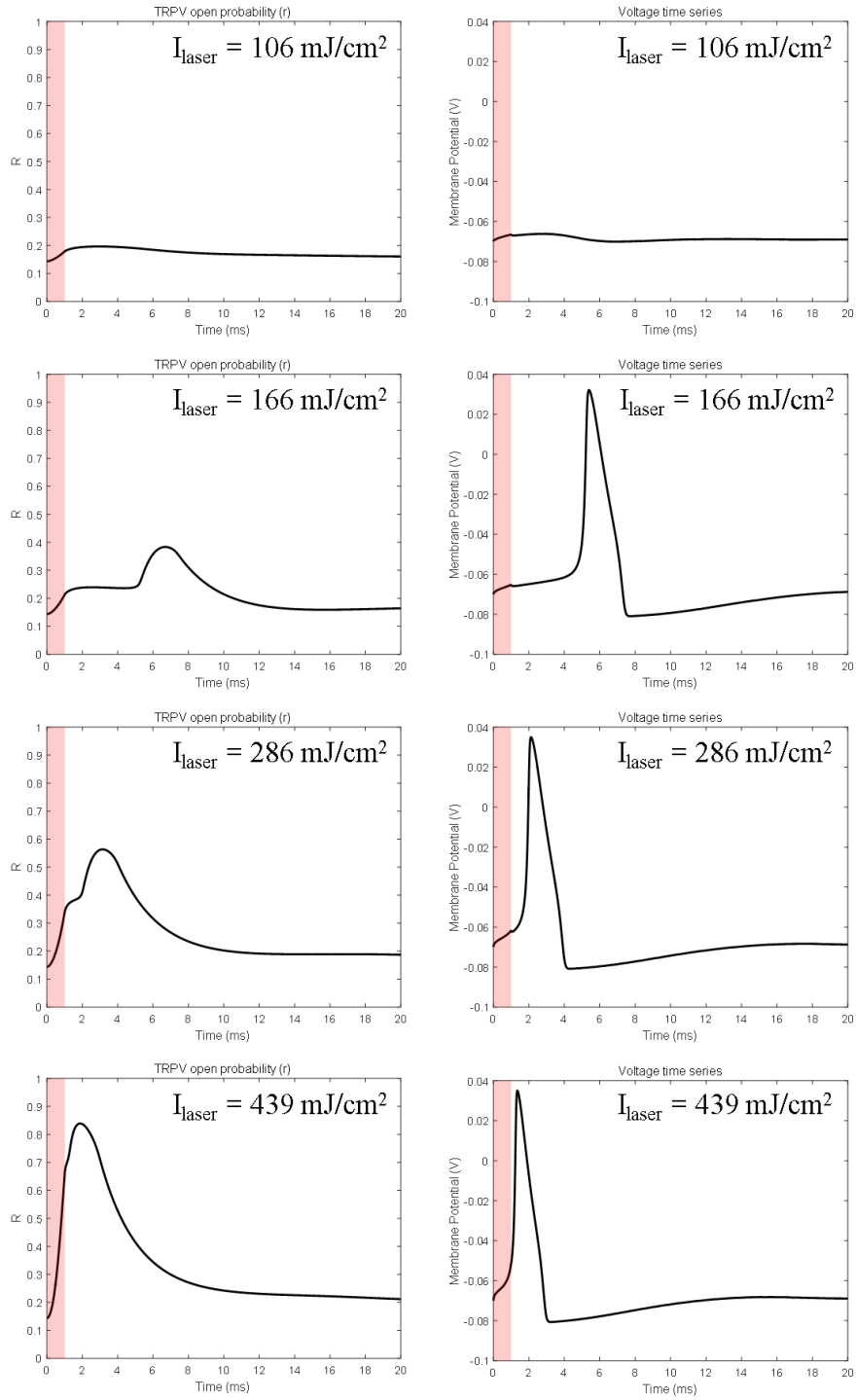

Figure 57 Graphs indicating open probabilities of TRPV1 channel and corresponding action potential for four different laser intensities. All the plots were obtained from the modified H-H model considering membrane capacitance change and TRPV1 channel.

Chapter 4: Discussion

This chapter discusses the pros and cons of the conventional INS by summarizing our previous works. Safety concerns associated with GNRs are dealt. Discussion of linking experimental data and simulated results were considered. Potential applications and the further improvement are discussed.

4.1. Comparison with previous results

GNRs-mediated INS can be compared with the conventional INS in terms of the type of neural tissue implemented in the experiments which are summarized in Table 9. The most outstanding feature of GNRs-mediated INS is the stimulation threshold. GNRs-mediated INS has about the half or minimum one sixth of the stimulation threshold comparing to the conventional INS. Compared to the conventional INS which suffers tissue damage due to strong water absorption of light, GNRs-mediated INS uses the wavelength in the range of NIR region that could reduce the water absorption of light. GNRs-mediated INS has another important advantage that antibody are conjugated to the GNRs in order to deliver GNRs to the target tissue with a strong affinity which could stimulate specific cells of interest.

Table 9 Comparison of conventional and GNRs-mediated INS

	Nano-particles complex	Neural Tissue	Stimulation threshold (mJ/cm^2)	Wavelength (nm)	Pulse duration (ms)
J. Wells et al [24]	-	Rat sciatic *in vivo*	320	2120	0.25
J. M. Cayce et al [25]	-	Thalamocortical brain slice *ex vivo*	190	4400	0.005
J. M. Cayce et al [85]	-	Rat somatosensory cortex *in vivo* (Neuron, astrocyte)	Unknown Radiant exposure of 100 ~ 880	1875	0.25
This study	GNRs	Rat sciatic nerve *in vivo*	159	980	1
This study	Antibody conjugated GNRs	Cultured rat hippocampal neuron	30.1	980	0.4
This study	Antibody conjugated GNRs	Rat motor cortex *in vivo*	128	980	1.5
This study	Antibody conjugated GNRs	Cultured rat astrocyte	1312	980	0.95

As mentioned above nanoparticle-mediated INS shows superiority over conventional INS. Recently, many researchers demonstrated nanoparticle-mediated near-infrared neuro-modulation. In 2013, C. Paviolo et at, first demonstrated that laser exposure of GNRs can increase neuronal outgrowth [109]. In 2014, researchers demonstrated that GNRs and/or spherical gold nanoparticles induce neural activation [110], and inhibition [111]. On the following, surface-modified

nanoparticles were employed to deliver and bound to the specific neural cell [97] enabling washout resistance and cell-specific stimulation.

Table 10 Comparison of recently demonstrated GNRs-mediated NIR neural modulation techniques

Institution /Year	**Target**	**Particle**	**Wavelength (nm)**	**Radiant laser exposure**
Univ. of Chicago /2015 [97]	Cultured rat dorsal root ganglion cells	Antibody-conjugated spherical gold nanoparticle	532	< 126 [mJ] (1 ms duration)
KAIST /2014 [111]	Cultured rat hippocampal neuron	GNRs	785	0 ~ 1500 [mW/cm^2]
KAIST /2016 [112]	Cultured rat hippocampal neuron	GNRs on the MEA substrate	785	300 ~ 2100 [mW/cm^2]
This study /2014	Rat sciatic nerve *in vivo*	GNRs	980	< 159 [mJ/cm^2] (1 ms duration)
This study /2016	Cultured rat hippocampal neuron	Antibody-conjugated GNRs	980	< 30.1 [mJ/cm^2] (0.4 ms duration)
This study /2016	Cultured rat astrocyte	Antibody-conjugated GNRs	980	1.312 [J/cm^2] (0.95 ms duration)
Swinberne Univ. /2013 [109]	Mouse neuroblastoma × rat glioma	GNRs	780	1250 ~ 7500 [W/cm^2]
Swinberne Univ. /2014 [110]	Cultured rat auditory neuron	GNRs Spherical gold nanoparticle	780	0 ~ 90 [μJ] (> 25 ms duration)

4.2. Safety of gold nanoparticle mediated infrared neural stimulation

The safety problem associated with INS arose from the fact that heat is the main factor that drives the activation of neurons. When shining an infrared light to the neural tissue, the light energy is absorbed in the tissue to generate heat. As it is known that thermal heat near the plasma membrane is responsible for the neuromodulation; however, excessive heat accumulated in the tissue unavoidably damages them. Many researches have shown that INS is safe. Nevertheless, the acceptable range of laser exposure while avoiding the tissue damage is small which limits the variability of stimulus parameters. Moreover, acceptable range of laser exposure depends on the conditions of tissue environment. Hence it is necessary to wide up the acceptable range of stimulation.

In this study, we used NIR light whose extinction coefficient is smaller than that of the infrared light ranging over 1400 nm [39]. The use of NIR light reduces the accumulation of the light energy in the tissue. While avoiding bulk tissue absorption of light, GNRs were introduced to the neuronal membrane to absorb light and to generate localized heat. GNRs generated localized thermal heat near the plasma membrane to induce action potentials.

In this study, we showed that the combination of NIR light and GNRs successfully lowered the radiant exposure energy. We demonstrated that GNRs lowers the radiant exposure threshold energy of 0.159 mJ/cm^2 compared to the value obtained in the experiments without GNRs which is 0.48 mJ/cm^2. Previous result of stimulation threshold obtained without GNRs was 0.32 mJ/cm^2 [12]. These results asserted that GNRs-mediated INS lower the stimulation threshold even much lower than the ablation threshold.

Although GNRs meditated INS has superiority over conventional INS in terms of low radiant exposure, further consideration of tissue damage should be taken into account when stimulating at high frequency. The average heat accumulation rate within a single cycle should be lower than the average heat dissipation rate in a single cycle. Moreover, the effect of tissue upon long-term irradiation is still not fully understood. Studies have revealed that INS worked without acute tissue damage [113]. However, there is no evidence of showing chronic stimulation is safe. Therefore, the effect on tissue upon chronic stimulation of INS should also be investigated.

As with foreign materials are not welcomed and may have some undesired side effects in the body, the cytotoxicity of GNRs has been widely investigated. Gold is benign and biologically inert only if the when the diameter of gold is larger than 2 nm. Gold nanoparticles of which the diameter smaller than 2 nm show unusual chemical reactivity [114]. Generally, gold nanoparticles that are used in biomedical research have dimensions larger than 10 nm which is sufficient to decrease their surface reactivity. The other factor that matters cytotoxicity comes from the capping agents used to stabilize the gold nanoparticles. For example, cetyltrimethylammonium bromide (CTAB) frequently used as a capping molecule shows apparent cytotoxicity [115]. Therefore, efforts have paid to replace the CTAB by the non-toxic capping molecules or prevent CTAB desorption from the surface of gold nanoparticles.

It is worth noting that the cellular uptake of nanoparticles occurs which depends on the incubation time, size, shape, surface charge, functionality, concentration, aggregation state, the type of cell. Among the nanoparticles tested in the range from 2 nm to 100 nm, size of 40 ~ 50 nm showed increased in cellular

uptake and affects downstream signaling and subsequent cellular responses such as cell death. Moreover, rod shape gold nanoparticles (14 × 74 nm) are less internalized into the cell compared to the spherical gold nanoparticles of 14 and 74 nm [116].

In this study, rod shape gold nanoparticles having a length and width of 80.4 nm, and 15.3 nm, respectively, were used. Due to the shape and the dimension of GNRs, we could avoid toxicity as well as cellular uptake. Moreover, instead of using CTAB for capping agents non-toxic capping molecules were used to reduce cytotoxicity.

4.3. Link between experimental and simulation results

We demonstrated that GNRs-mediated INS can trigger neural depolarization and validated that local heat generated from GNRs induce membrane capacitance increase and opening of TRPV1 channel which in turn lead to generation of action potential. Though we found that proposed mechanisms could induce neural depolarization, there are some issues in connecting the experimental and the simulation results.

Stimulation thresholds determined in the experiment and the simulation can be directly compared. Stimulation thresholds obtained when simulating the modified H-H models which considered the membrane capacitance change, the TRPV1 channel, and both membrane capacitance change and TRPV1 channel were found out to be 439, 286, 166 mJ/cm^2, respectively. Among them, the TRPV1 channel considered H-H model is not realistic since capacitance change is always

present in the membrane where transient heat is applied. Since the TRPV1 channel does not exist on the sciatic nerve, the simulation result using membrane capacitance considered H-H model can be matched with the result performed in rat sciatic nerve. For the case of sciatic nerve experiments, the stimulation threshold was determined as 159 mJ/cm^2, which is about the one third of the simulation result of 439 mJ/cm^2. TRPV1 channel and membrane capacitance change considered H-H model may also be compared with the experiment involving cultured rat hippocampal neuron since hippocampal neurons possess TRPV1 channels at the membrane. Stimulation threshold was found as 30.1 mJ/cm^2 in rat hippocampal neuron while 166 mJ/cm^2 was obtained in the simulation study. Gap between stimulation thresholds obtained experimentally and in numerical simulation were not bigger than fivefold. Moreover, the tendency of decrement in stimulation threshold observed in hippocampal neuron compared to that observed in sciatic nerve was also found in the simulation study.

Although numerical simulation results follow the experimental results, the discrepancies between them should be addressed. Main factor contributing this gap is the inaccurate coverage value of GNRs and the distance between GNRs and the plasma membrane. We assumed the coverage of GNRs as 0.27 and distance as 50 nm for all cases. However, coverage of GNRs in the experiment performed using hippocampal neuron should be larger since actual GNRs appear as a cluster of GNRs. Moreover, the distance between GNRs and neural membrane should be small. If the coverage of GNRs becomes large and the distance becomes small in the TRPV1 channel and the capacitance considered H-H model, we expect that the stimulation threshold would be smaller than the previously determined value. Moreover, not only GNRs but also neural tissue and water generate heat by absorbing light energy. If we consider water and neural tissue, then stimulation

threshold obtained in the simulations will be lowered. Finally, we have only considered voltage-gated sodium, potassium channels and temperature-sensitive TRPV1 ion channel. We could speculate that consideration of other ion channels such as voltage-gated calcium channel [117], temperature-sensitive potassium TREK-1 channel [111] which are also responsible for the neural activation could reduce the gap between the simulation and experimental results.

The stimulation threshold for the case in the rat sciatic nerve experiment is 5.3 times bigger than that of the hippocampal neuron experiment. However, simulation results show only 2.6 times bigger. This gap might be attributed to the difference in the photothermal efficiency of GNRs for each cases. As mentioned in the section 2.3.3, GNRs in the rat sciatic nerve generate only the half of the LSP of the case in the experiment of cultured hippocampal neuron. Therefore, it is reasonable to double the exposure energy when simulating the membrane capacitance considered H-H model. By doing so, we could obtain nearly the same ratio of stimulation thresholds ($I_{\text{sciatic nerve}}/I_{\text{hippocampal neuron}}$) of simulation and experimental results.

Since electrophysiological recording was basically multi-unit recording, direct comparison of neural waveforms is not reasonable. However, there are some similarities in the time when the neuron starts to fire. Sciatic nerve generates compound nerve action potentials at the onset of laser irradiation without delay which was similar to the result in the modified H-H model. H-H model which considered only the TRPV1 channel showed delayed action potential which was similar to the results obtained using the cultured hippocampal neuron.

We have modeled the mechanisms underlying GNRs-mediated INS using modified H-H model and verified that the model successfully predicts the

experimental results only when considering several factors mentioned above. We speculate that the model could predict stimulation threshold for various experimental conditions such as concentration of GNRs.

4.4. TRPV1 channel and membrane capacitance

We have considered a temperature-dependent membrane capacitor and a temperature-sensitive TRPV1 ion channel in the theoretical modeling of GNRs-mediated INS as mentioned in section 2.6.5.

When the temperature near the membrane jump, abrupt ion distribution change occurs resulting rapid membrane potential change. Moreover, temperature increase also causes TRPV1 channel opening. Since the TRPV1 channel close slowly compared to the temporal profile of the membrane capacitance, influx of current is maintained long period.

In order to determine which factor among the TRPV1 channel and the variable membrane capacitor is dominant factor contributing to the neural depolarization, we compared the stimulation threshold for the both cases. The stimulation thresholds obtained when stimulating the models which considered the variable membrane capacitor were 439 mJ/cm^2, and 286 mJ/cm^2, respectively as depicted in the section 3.4. Based on these results, we could conjecture that TRPV1 channel affects more on the GNRs-mediated INS compared to the variable capacitance. This could be also experimentally verified by comparing stimulation threshold results of before and after blocking TRPV1 channel using channel blockers.

4.5. Possible mechanisms of GNRs-mediated INS

We discuss that the latency measured while stimulating neurons without cell-targeted GNRs is delayed compared to the latency measured in the case of cell-targeted GNRs as mentioned in section 3.2.1. It is possible that the latency is delayed by the prolonged activation of neurons due to the residual heat near the cells after bulk tissue heating. Otherwise, there may exist different underlying mechanisms between optical stimulation with and without GNRs.

When stimulating neuron with cell-targeted GNRs, GNRs that bound to cell surface generate localized heat to triggers neural activities. However, without GNRs, high laser intensity is needed to stimulate the neurons which cause bulk heating of cells. We speculated that the bulk heating could induce transient membrane capacitance change of not only the cell surface membrane but also the membrane of intracellular organelles. Some intracellular organelles such as endoplasmic reticulum or mitochondria, where calcium is stored, dynamically participate in generation of intracellular calcium signals enhancing neuronal activities [118]. The light-induced activation of intracellular organelles can trigger intracellular signaling via the increase of intracellular calcium concentration. This hypothesis is consistent with the delayed latency because the intracellular calcium signaling is known to be slow compared to inward calcium influx through voltage-gated calcium channels activated by action potentials [119]. Similarly, intracellular organelles are responsible for the generation of intracellular Ca^{2+} transient in the astrocyte cells as mentioned in the section 3.3.1. However, direct activation of intracellular organelles by GNRs-mediated NIR stimulation could result tissue damage, since high laser intensity is required to heat up the intracellular organelles using the GNRs attached in the membrane. Therefore, it is essential to find whether

cells are alive after stimulation by performing the Live/Dead cell test.

4.6. Potential applications

Optical neuromodulation techniques have widely been investigated owing to the fascinating features of photonics and their applications. Compared to the electric charge which spreads out through the conductive medium, light can be focused and delivered in a specific region even though it scattered. Furthermore, light can travel through the air conveying its energy. These features led researchers to build optically controlled neuromodulation techniques. Recently, optical neuromodulation techniques have been developed having high spatial selective, and non- or minimally invasive properties.

Particularly, INS has been demonstrated for the first time in 2005 [24]. Attempts to apply in cochlear implant has been performed which could selectively stimulate ganglion cells [38]. Recently, the feasibility of INS in the human spinal cord has been performed [29]. However, the possible tissue damage due to high water absorption of light is limiting clinical use of INS. As an advancement technique of conventional INS, GNRs-mediated INS can modulate neuron with low laser exposure. Therefore, GNRs-mediated INS is more applicable for clinical applications compared to the conventional INS.

Since we demonstrated that GNRs-mediated INS is feasible in central nervous system, this method can be used in the neuroprosthetic devices. For example, cochlear and retinal implants are the possible candidates, since they require high spatial selectivity and the use of multiple channels simultaneously. In addition, this method can be implemented in deep brain stimulation system in some

case where specific targeting is needed. Moreover, we also expect that GNRs-mediated INS can be applied in cortically controlled neuroprosthetic device.

Interestingly, we could selectively enhance specific GNRs by changing the resonance wavelength of GNRs and illuminate with the light that matches the resonance wavelength of GNRs. If the different types of cells are conjugated with the different GNRs, it is expected to modulate cell by the cell types. This feature can be wide up the potential applications not only in the clinics but also in the research area. For instance, we could selectively stimulate inhibitory and excitatory neurons that are intermingled. By selectively stimulate the specific neuron; we believed that it can be applied in advanced deep brain stimulation system. Since, conventional electrical stimulation cannot stimulate neural cells by their cell types and had a hard time localize the stimulation site; it is hard to unveil the neural function and neural network using electrical stimulation. In this kind of neuroscience research, GNRs-mediated INS can be implemented to selectively and locally stimulate the specific cell of interest to find the functions and the networks of neuron.

Overall, we expect that GNRs-mediated INS can be applied in the clinical and research area where minimally invasive, selective and cell-type specific neurostimulation are needed.

4.7. Opportunities for further improvements

This study provides that GNRs-mediated INS is safe in terms of low laser exposure, effective in terms of delivery of GNRs to the plasma membrane and wide applicable in terms of optical stimulation of non-neuronal cell. Due to

aforementioned features, GNRs meditated INS can be applied in various area including clinics and research fields. However, it still requires further improvements.

First, the concerns of injecting GNRs to the target site should be resolved. GNRs can be directly injected using a micro-needle installed in microinjection system. However, it is invasive. Especially, direct injection to the deep brain could damage the neural tissue due to the neural tissue penetration using sharp needle. In this case, an intravenous injection can be the deliver GNRs to the target site, only if GNRs pass through the blood brain barrier (BBB). Note that BBB covers the blood vessels in the brain and blocking the entering of the particles while small molecules pass through easily [120]. Interestingly, focused ultrasound can open the BBB letting large particles pass through the blood vessels [120]. We expect that combination of the intravenous injection of GNRs and focused ultrasound could solve the problem associated with direct injection of GNRs. In the following, application into clinics is also needed.

Second, cell-type specific stimulation system should be developed. With aids of GNRs which can be tuned their resonant wavelength depending on their aspect ratio, cell-type specific stimulation is possible. In order to achieve cell-type specific stimulation, it is essential to find a conjugation mediator that specifically bound to the target site. Prior to selectively modulate cell-type of interest, different types of GNRs in terms of resonant wavelength are bound to the corresponding target neurons. By selecting the light, we could select the specific GNRs and stimulate the specific neural cells.

Recently, inhibition of neural cell by GNRs-mediated infrared light of long duration has been demonstrated [111]. By modulating the stimulating pulse

duration, activation and inhibition of neurons can be achieved. It is expected that combination of cell-specific targeting and the laser pulse modulation can control the activities of specific cells of interest.

In the consideration of clinical uses, safety issue must be considered and validated. Moreover, neuroprosthetic devices such as cochlear implant, retinal implant and DBS stimulate neural tissue with a high repetition rate. Validation of safety issue confronting high repetition rate must also be considered.

Finally, the light source should be miniaturized in order to be applied in clinics. Laser system used in this study is bulk and operated with DAQ equipped computer. Practically, it is impossible to be a source for neuroprosthetic devices since it is not portable. Therefore, it is essential to develop compact, miniaturized and portable laser system. Moreover, to simulate multi-neural cells simultaneously, introduction of multi-channels having a multi-spectrum laser system is required.

Chapter 5: Conclusion

This dissertation presents fundamental research in the development of GNRs-mediated NIR stimulation of neuron as well as astrocyte. NIR light was used, because conventional INS that uses infrared light suffered from tissue damage due to water absorption of light. While NIR light penetrated deep inside the tissue, GNRs were positioned vicinity of the neural tissue to absorb light and generate local heating. We therefore demonstrated enhanced INS using LSPRs of GNRs. This claim is supported by the following:

(1) GNRs-mediated INS reduces the stimulation threshold by one third compared to the INS without GNRs.

(2) Stimulation threshold obtained in the GNRs-mediated INS is out of the the tissue ablation range.

(1) and (2) support GNRs-mediate INS is safe.

(3) Antibody-conjugated GNRs strongly bound to the neuronal membrane.

(4) Antibody-conjugated GNRs-mediated INS elicit faster neural depolarization with lower stimulation threshold compared to INS without GNRs.

(5) Antibody-conjugated GNRs effectively elicit motor behavior.

(3), (4), and (5) support that cell-targeted GNRs effectively stimulate neural cells.

(6) Combination of cell-targeted GNRs and NIR light induce intracellular calcium transient in the astrocytes.

(6) supports GNRs-mediated INS can be applied in non-neuronal cells.

We theoretically elucidated on the GNRs-mediated INS in three steps; (1) generation of local heat from the GNRs, (2) membrane capacitance change and opening of TRPV1 channel due to temperature increase in the membrane, (3) generation of action potential. We numerically demonstrated that our proposed mechanism could successfully generated action potential at the onset of laser irradiation.

Consequently, this dissertation has experimentally and theoretically demonstrated that GNRs-mediated INS generate local temperature increase in the plasma membrane which lead to the capacitance change and the opening of temperature-sensitive ion channels and finally generating action potentials.

Reference

[1] B. S. Wilson, C. C. Finley, D. T. Lawson, R. D. Wolford, D. K. Eddington, and W. M. Rabinowitz, "Better speech recognition with cochlear implants," *Nature*, Vol. 352, pp. 236-238, (1991).

[2] S. K. An, S. I. Park, S. B. Jun, C. J. Lee, K. M. Byun, J. H. Sung, B. S. Wilson, S. J. Rebscher, S. H. Oh, and S. J. Kim, "Design for a Simplified Cochlear Implant System," *IEEE Transactions on Biomedical Engineering*, Vol. 54, pp. 973-982, (2007).

[3] K. D. Brown and T. J. Balkany, "Benefits of bilateral cochlear implantation: a review," *Current Opinion in Otolaryngology & Head and Neck Surgery*, Vol. 15, pp. 315-318, (2007).

[4] J. D. Weiland, W. Liu, and M. S. Humayun, "Retinal Prosthesis," *Annual Review of Biomedical Engineering*, Vol. 7, pp. 361-401, (2005).

[5] J. Jeong, S. H. Bae, K. S. Min, J. M. Seo, H. Chung, and S. J. Kim, "A Miniaturized, Eye-Conformable, and Long-Term Reliable Retinal Prosthesis Using Monolithic Fabrication of Liquid Crystal Polymer (LCP)," *IEEE Transactions on Biomedical Engineering*, Vol. 62, pp. 982-989, (2015).

[6] E. Zrenner, "Will Retinal Implants Restore Vision?," *Science*, Vol. 295, pp. 1022-1025, (2002).

[7] J. S. Perlmutter and J. W. Mink, "DEEP BRAIN STIMULATION," *Annual Review of Neuroscience*, Vol. 29, pp. 229-257, (2006).

[8] J. M. Bronstein, M. Tagliati, R. L. Alterman, and et al., "Deep brain stimulation for parkinson disease: An expert consensus and review of key issues," *Archives of Neurology*, Vol. 68, pp. 165-165, (2011).

[9] E. Margalit, M. Maia, J. D. Weiland, R. J. Greenberg, G. Y. Fujii, G. Torres, D. V. Piyathaisere, T. M. O'Hearn, W. Liu, G. Lazzi, G. Dagnelie, D. A. Scribner, E. de Juan Jr, and M. S. Humayun, "Retinal Prosthesis for the Blind," *Survey of Ophthalmology*, Vol. 47, pp. 335-356, (2002).

[10] A. L. Hodgkin and A. F. Huxley, "A quantitative description of membrane current and its application to conduction and excitation in nerve," *The Journal of Physiology*, Vol. 117, pp. 500-544, (1952).

[11] W. M. Grill, S. E. Norman, and R. V. Bellamkonda, "Implanted Neural Interfaces: Biochallenges and Engineered Solutions," *Annual Review of Biomedical Engineering*, Vol. 11, pp. 1-24, (2009).

[12] J. Wells, C. Kao, E. D. Jansen, P. Konrad, and A. Mahadevan-Jansen, "Application of infrared light for in vivo neural stimulation," *Journal of Biomedical Optics*, Vol. 10, pp. 064003-064012, (2005).

[13] G. Bonmassar, S. W. Lee, D. K. Freeman, M. Polasek, S. I. Fried, and J. T. Gale, "Microscopic magnetic stimulation of neural tissue," *Nature Communications*, Vol. 3, pp. 1-10, (2012).

[14] H. Huang, S. Delikanli, H. Zeng, D. M. Ferkey, and A. Pralle, "Remote control of ion channels and neurons through magnetic-field heating of nanoparticles," *Nature Nanotechnology*, Vol. 5, pp. 602-606,

(2010).
[15] R. Chen, G. Romero, M. G. Christiansen, A. Mohr, and P. Anikeeva, "Wireless magnetothermal deep brain stimulation," *Science*, Vol. 347, pp. 1477-1480, (2015).
[16] Y. Tufail, A. Matyushov, N. Baldwin, M. L. Tauchmann, J. Georges, A. Yoshihiro, S. I. H. Tillery, and W. J. Tyler, "Transcranial Pulsed Ultrasound Stimulates Intact Brain Circuits," *Neuron*, Vol. 66, pp. 681-694, (2010).
[17] C.-P. Richter, A. I. Matic, J. D. Wells, E. D. Jansen, and J. T. Walsh, "Neural stimulation with optical radiation," *Laser & photonics reviews*, Vol. 5, pp. 68-80, (2011).
[18] E. S. Boyden, F. Zhang, E. Bamberg, G. Nagel, and K. Deisseroth, "Millisecond-timescale, genetically targeted optical control of neural activity," *Nature Neuroscience*, Vol. 8, pp. 1263-1268, (2005).
[19] X. Han and E. S. Boyden, "Multiple-Color Optical Activation, Silencing, and Desynchronization of Neural Activity, with Single-Spike Temporal Resolution," *PLoS ONE*, Vol. 2, pp. e299, (2007).
[20] C.-P. Richter and X. Tan, "Photons and neurons," *Hearing Research*, Vol. 311, pp. 72-88, (2014).
[21] C. Hosokawa, Y. Sakamoto, S. N. Kudoh, Y. Hosokawa, and T. Taguchi, "Femtosecond laser-induced stimulation of a single neuron in a neuronal network," *Applied Physics A*, Vol. 110, pp. 607-612, (2012).
[22] J. M. Jang, J. Lee, H. Kim, N. L. Jeon, and W. Jung, "One-photon and two-photon stimulation of neurons in a microfluidic culture system," *Lab on a Chip*, Vol., (2016).
[23] U. K. Tirlapur, K. König, C. Peuckert, R. Krieg, and K.-J. Halbhuber, "Femtosecond Near-Infrared Laser Pulses Elicit Generation of Reactive Oxygen Species in Mammalian Cells Leading to Apoptosis-like Death," *Experimental Cell Research*, Vol. 263, pp. 88-97, (2001).
[24] J. Wells, C. Kao, K. Mariappan, J. Albea, E. D. Jansen, P. Konrad, and A. Mahadevan-Jansen, "Optical stimulation of neural tissue in vivo," *Optics Letters*, Vol. 30, pp. 504-506, (2005).
[25] J. M. Cayce, C. C. Kao, J. D. Malphrus, P. E. Konrad, A. Mahadevan-Jansen, and E. D. Jansen, "Infrared Neural Stimulation of Thalamocortical Brain Slices," *IEEE Journal of Selected Topics in Quantum Electronics*, Vol. 16, pp. 565-572, (2010).
[26] A. D. Izzo, E. Suh, J. Pathria, J. J. T. Walsh, D. S. Whitlon, and C.-P. Richter, "Selectivity of neural stimulation in the auditory system: a comparison of optic and electric stimuli," *Journal of Biomedical Optics*, Vol. 12, pp. 021008-021008-021007, (2007).
[27] A. D. Izzo, J. T. Walsh, Jr., E. D. Jansen, M. Bendett, J. Webb, H. Ralph, and C. P. Richter, "Optical Parameter Variability in Laser Nerve Stimulation: A Study of Pulse Duration, Repetition Rate, and Wavelength," *IEEE Transactions on Biomedical Engineering*, Vol. 54, pp. 1108-1114, (2007).
[28] A. D. Izzo, J. T. Walsh, H. Ralph, J. Webb, M. Bendett, J. Wells, and C.-P. Richter, "Laser Stimulation of Auditory Neurons: Effect of

Shorter Pulse Duration and Penetration Depth," *Biophysical Journal*, Vol. 94, pp. 3159-3166, (2008).

[29] J. M. Cayce, J. D. Wells, J. D. Malphrus, C. Kao, S. Thomsen, N. B. Tulipan, P. E. Konrad, E. D. Jansen, and A. Mahadevan-Jansen, "Infrared neural stimulation of human spinal nerve roots in vivo," *Neurophotonics*, Vol. 2, pp. 015007, (2015).

[30] A. R. Duke, J. M. Cayce, J. D. Malphrus, P. Konrad, A. Mahadevan-Jansen, and E. D. Jansen, "Combined optical and electrical stimulation of neural tissue in vivo," *Journal of Biomedical Optics*, Vol. 14, pp. 060501-060501-060503, (2009).

[31] R. D. Austin, P. Erik, A. M. Mark, A. James, T. Dustin, and E. D. Jansen, "Hybrid electro-optical stimulation of the rat sciatic nerve induces force generation in the plantarflexor muscles," *Journal of Neural Engineering*, Vol. 9, pp. 066006, (2012).

[32] A. R. Duke, M. W. Jenkins, H. Lu, J. M. McManus, H. J. Chiel, and E. D. Jansen, "Transient and selective suppression of neural activity with infrared light," *Scientific Reports*, Vol. 3, pp. 2600, (2013).

[33] J. Wells, C. Kao, P. Konrad, T. Milner, J. Kim, A. Mahadevan-Jansen, and E. D. Jansen, "Biophysical Mechanisms of Transient Optical Stimulation of Peripheral Nerve," *Biophysical Journal*, Vol. 93, pp. 2567-2580, (2007).

[34] M. G. Shapiro, K. Homma, S. Villarreal, C.-P. Richter, and F. Bezanilla, "Infrared light excites cells by changing their electrical capacitance," *Nature Communications*, Vol. 3, pp. 736, (2012).

[35] A. Patapoutian, A. M. Peier, G. M. Story, and V. Viswanath, "ThermoTRP channels and beyond: mechanisms of temperature sensation," *Nature Reviews Neuroscience*, Vol. 4, pp. 529-539, (2003).

[36] E. S. Albert, J. M. Bec, G. Desmadryl, K. Chekroud, C. Travo, S. Gaboyard, F. Bardin, I. Marc, M. Dumas, G. Lenaers, C. Hamel, A. Muller, and C. Chabbert, "TRPV4 channels mediate the infrared laser-evoked response in sensory neurons," *Journal of Neurophysiology*, Vol. 107, pp. 3227-3234, (2012).

[37] T. Voets, G. Droogmans, U. Wissenbach, A. Janssens, V. Flockerzi, and B. Nilius, "The principle of temperature-dependent gating in cold- and heat-sensitive TRP channels," *Nature*, Vol. 430, pp. 748-754, (2004).

[38] A. D. Izzo, C.-P. Richter, E. D. Jansen, and J. T. Walsh, "Laser stimulation of the auditory nerve," *Lasers in Surgery and Medicine*, Vol. 38, pp. 745-753, (2006).

[39] D. Jaque, L. Martinez Maestro, B. del Rosal, P. Haro-Gonzalez, A. Benayas, J. L. Plaza, E. Martin Rodriguez, and J. Garcia Sole, "Nanoparticles for photothermal therapies," *Nanoscale*, Vol. 6, pp. 9494-9530, (2014).

[40] A. C. Thompson, S. A. Wade, N. C. Pawsey, and P. R. Stoddart, "Infrared Neural Stimulation: Influence of Stimulation Site Spacing and Repetition Rates on Heating," *IEEE Transactions on Biomedical Engineering*, Vol. 60, pp. 3534-3541, (2013).

[41] J. D. Wells, S. Thomsen, P. Whitaker, E. D. Jansen, C. C. Kao, P. E. Konrad, and A. Mahadevan-Jansen, "Optically mediated nerve stimulation: Identification of injury thresholds," *Lasers in Surgery and Medicine*, Vol. 39, pp. 513-526, (2007).
[42] M. M. Chernov, G. Chen, and A. W. Roe, "Histological Assessment of Thermal Damage in the Brain Following Infrared Neural Stimulation," *Brain Stimulation*, Vol. 7, pp. 476-482, (2014).
[43] E. Hutter and J. H. Fendler, "Exploitation of Localized Surface Plasmon Resonance," *Advanced Materials*, Vol. 16, pp. 1685-1706, (2004).
[44] H. Chen, L. Shao, Q. Li, and J. Wang, "Gold nanorods and their plasmonic properties," *Chemical Society Reviews*, Vol. 42, pp. 2679-2724, (2013).
[45] J. R. Cole, N. A. Mirin, M. W. Knight, G. P. Goodrich, and N. J. Halas, "Photothermal Efficiencies of Nanoshells and Nanorods for Clinical Therapeutic Applications," *The Journal of Physical Chemistry C*, Vol. 113, pp. 12090-12094, (2009).
[46] S. Schlücker, "Surface-Enhanced Raman Spectroscopy: Concepts and Chemical Applications," *Angewandte Chemie International Edition*, Vol. 53, pp. 4756-4795, (2014).
[47] V. P. Zharov, K. E. Mercer, E. N. Galitovskaya, and M. S. Smeltzer, "Photothermal Nanotherapeutics and Nanodiagnostics for Selective Killing of Bacteria Targeted with Gold Nanoparticles," *Biophysical Journal*, Vol. 90, pp. 619-627, (2006).
[48] S. E. Lee, G. L. Liu, F. Kim, and L. P. Lee, "Remote Optical Switch for Localized and Selective Control of Gene Interference," *Nano Letters*, Vol. 9, pp. 562-570, (2009).
[49] D. P. O'Neal, L. R. Hirsch, N. J. Halas, J. D. Payne, and J. L. West, "Photo-thermal tumor ablation in mice using near infrared-absorbing nanoparticles," *Cancer Letters*, Vol. 209, pp. 171-176, (2004).
[50] L. J. Steven, "Optical properties of biological tissues: a review," *Physics in Medicine and Biology*, Vol. 58, pp. R37, (2013).
[51] C. Sönnichsen, T. Franzl, T. Wilk, G. von Plessen, J. Feldmann, O. Wilson, and P. Mulvaney, "Drastic Reduction of Plasmon Damping in Gold Nanorods," *Physical Review Letters*, Vol. 88, pp. 077402, (2002).
[52] S. A. Stanley, J. E. Gagner, S. Damanpour, M. Yoshida, J. S. Dordick, and J. M. Friedman, "Radio-Wave Heating of Iron Oxide Nanoparticles Can Regulate Plasma Glucose in Mice," *Science*, Vol. 336, pp. 604-608, (2012).
[53] X.-d. Wang, O. S. Wolfbeis, and R. J. Meier, "Luminescent probes and sensors for temperature," *Chemical Society Reviews*, Vol. 42, pp. 7834-7869, (2013).
[54] O. L. Muskens, G. Bachelier, N. D. Fatti, F. Vallée, A. Brioude, X. Jiang, and M.-P. Pileni, "Quantitative Absorption Spectroscopy of a Single Gold Nanorod," *The Journal of Physical Chemistry C*, Vol. 112, pp. 8917-8921, (2008).
[55] T. Ming, L. Zhao, Z. Yang, H. Chen, L. Sun, J. Wang, and C. Yan,

"Strong Polarization Dependence of Plasmon-Enhanced Fluorescence on Single Gold Nanorods," *Nano Letters*, Vol. 9, pp. 3896-3903, (2009).

[56] G. Fischer, S. Kostic, H. Nakai, F. Park, D. Sapunar, H. Yu, and Q. Hogan, "Direct injection into the dorsal root ganglion: Technical, behavioral, and histological observations," *Journal of Neuroscience Methods*, Vol. 199, pp. 43-55, (2011).

[57] J. J. Iliff, M. Wang, Y. Liao, B. A. Plogg, W. Peng, G. A. Gundersen, H. Benveniste, G. E. Vates, R. Deane, S. A. Goldman, E. A. Nagelhus, and M. Nedergaard, "A Paravascular Pathway Facilitates CSF Flow Through the Brain Parenchyma and the Clearance of Interstitial Solutes, Including Amyloid β," *Science Translational Medicine*, Vol. 4, pp. 147ra111-147ra111, (2012).

[58] J. J. Iliff, H. Lee, M. Yu, T. Feng, J. Logan, M. Nedergaard, and H. Benveniste, "Brain-wide pathway for waste clearance captured by contrast-enhanced MRI," *The Journal of Clinical Investigation*, Vol. 123, pp. 1299-1309, (2013).

[59] L. Xie, H. Kang, Q. Xu, M. J. Chen, Y. Liao, M. Thiyagarajan, J. O'Donnell, D. J. Christensen, C. Nicholson, J. J. Iliff, T. Takano, R. Deane, and M. Nedergaard, "Sleep Drives Metabolite Clearance from the Adult Brain," *Science*, Vol. 342, pp. 373-377, (2013).

[60] A. Blau, "Cell adhesion promotion strategies for signal transduction enhancement in microelectrode array in vitro electrophysiology: An introductory overview and critical discussion," *Current Opinion in Colloid & Interface Science*, Vol. 18, pp. 481-492, (2013).

[61] D. A. Wagenaar, J. Pine, and S. M. Potter, "Effective parameters for stimulation of dissociated cultures using multi-electrode arrays," *J. Neurosci. Methods*, Vol. 138, pp. 27-37, (2004).

[62] H. Kamioka, E. Maeda, Y. Jimbo, H. P. C. Robinson, and A. Kawana, "Spontaneous periodic synchronized bursting during formation of mature patterns of connections in cortical cultures," *Neuroscience Letters*, Vol. 206, pp. 109-112, (1996).

[63] G. J. Brewer, J. R. Torricelli, E. K. Evege, and P. J. Price, "Optimized survival of hippocampal neurons in B27-supplemented neurobasal™, a new serum-free medium combination," *Journal of Neuroscience Research*, Vol. 35, pp. 567-576, (1993).

[64] K. L. Fields, D. N. Currie, and G. R. Dutton, "Development of Thy-1 antigen on cerebellar neurons in culture," *The Journal of Neuroscience*, Vol. 2, pp. 663-673, (1982).

[65] C. G. Dotti, R. G. Parton, and K. Simons, "Polarized sorting of glypiated proteins in hippocampal neurons," *Nature*, Vol. 349, pp. 158-161, (1991).

[66] W. S. Lee, M. K. Jain, B. M. Arkonac, D. Zhang, S.-Y. Shaw, S. Kashiki, K. Maemura, S.-L. Lee, N. K. Hollenberg, M.-E. Lee, and E. Haber, "Thy-1, a Novel Marker for Angiogenesis Upregulated by Inflammatory Cytokines," *Circulation Research*, Vol. 82, pp. 845-851, (1998).

[67] H. Kim, S. J. Taghados, K. Fischer, L.-S. Maeng, S. Park, and S.-S.

Yoo, "Noninvasive Transcranial Stimulation of Rat Abducens Nerve by Focused Ultrasound," *Ultrasound in Medicine & Biology*, Vol. 38, pp. 1568-1575, (2012).
[68] S. Tandon, N. Kambi, and N. Jain, "Overlapping representations of the neck and whiskers in the rat motor cortex revealed by mapping at different anaesthetic depths," *European Journal of Neuroscience*, Vol. 27, pp. 228-237, (2008).
[69] X. Han, "Optogenetics in the nonhuman primate," *Progress in brain research*, Vol. 196, pp. 215-233, (2012).
[70] O. G. S. Ayling, T. C. Harrison, J. D. Boyd, A. Goroshkov, and T. H. Murphy, "Automated light-based mapping of motor cortex by photoactivation of channelrhodopsin-2 transgenic mice," *Nat Meth*, Vol. 6, pp. 219-224, (2009).
[71] Vol., (!!! INVALID CITATION !!! {}).
[72] P. G. Haydon and G. Carmignoto, "Astrocyte Control of Synaptic Transmission and Neurovascular Coupling," *Physiological Reviews*, Vol. 86, pp. 1009-1031, (2006).
[73] E. A. Newman, "New roles for astrocytes: Regulation of synaptic transmission," *Trends in Neurosciences*, Vol. 26, pp. 536-542, (2003).
[74] J. W. Dani, A. Chernjavsky, and S. J. Smith, "Neuronal activity triggers calcium waves in hippocampal astrocyte networks," *Neuron*, Vol. 8, pp. 429-440, (1992).
[75] M. Nedergaard, "Direct signaling from astrocytes to neurons in cultures of mammalian brain cells," *Science*, Vol. 263, pp. 1768-1771, (1994).
[76] P. B. Guthrie, J. Knappenberger, M. Segal, M. V. L. Bennett, A. C. Charles, and S. B. Kater, "ATP Released from Astrocytes Mediates Glial Calcium Waves," *The Journal of Neuroscience*, Vol. 19, pp. 520-528, (1999).
[77] C. Henneberger, T. Papouin, S. H. R. Oliet, and D. A. Rusakov, "Long-term potentiation depends on release of d-serine from astrocytes," *Nature*, Vol. 463, pp. 232-236, (2010).
[78] C. G. Schipke, C. Boucsein, C. Ohlemeyer, F. Kirchhoff, and H. Kettenmann, "Astrocyte Ca2+ waves trigger responses in microglial cells in brain slices," *The FASEB Journal*, Vol., (2001).
[79] A. C. Charles, J. E. Merrill, E. R. Dirksen, and M. J. Sandersont, "Intercellular signaling in glial cells: Calcium waves and oscillations in response to mechanical stimulation and glutamate," *Neuron*, Vol. 6, pp. 983-992, (1991).
[80] T. A. Fiacco and K. D. McCarthy, "Intracellular Astrocyte Calcium Waves In Situ Increase the Frequency of Spontaneous AMPA Receptor Currents in CA1 Pyramidal Neurons," *The Journal of Neuroscience*, Vol. 24, pp. 722-732, (2004).
[81] G. Perea, A. Yang, E. S. Boyden, and M. Sur, "Optogenetic astrocyte activation modulates response selectivity of visual cortex neurons in vivo," *Nature Communications*, Vol. 5, (2014).
[82] M. Figueiredo, S. Lane, R. F. Stout Jr, B. Liu, V. Parpura, A. G.

Teschemacher, and S. Kasparov, "Comparative analysis of optogenetic actuators in cultured astrocytes," *Cell Calcium*, Vol. 56, pp. 208-214, (2014).
[83] Y. Zhao, Y. Zhang, X. Liu, X. Lv, W. Zhou, Q. Luo, and S. Zeng, "Photostimulation of astrocytes with femtosecond laser pulses," *Optics Express*, Vol. 17, pp. 1291-1298, (2009).
[84] M. Choi, J. Yoon, T. Ku, K. Choi, and C. Choi, "Label-free optical activation of astrocyte in vivo," *Journal of Biomedical Optics*, Vol. 16, pp. 075003-075003-075005, (2011).
[85] J. M. Cayce, M. B. Bouchard, M. M. Chernov, B. R. Chen, L. E. Grosberg, E. D. Jansen, E. M. C. Hillman, and A. Mahadevan-Jansen, "Calcium imaging of infrared-stimulated activity in rodent brain," *Cell Calcium*, Vol. 55, pp. 183-190, (2014).
[86] S. Schildge, C. Bohrer, K. Beck, and C. Schachtrup, "Isolation and Culture of Mouse Cortical Astrocytes," Vol., pp. e50079, (2013).
[87] R. M. Pruss, "Thy-1 antigen on astrocytes in long-term cultures of rat central nervous system," *Nature*, Vol. 280, pp. 688-690, (1979).
[88] S. A. Maier, *Plasmonics: Fundamentals and Applications* (Springer, 2007).
[89] G. C. Papavassiliou, "Optical properties of small inorganic and organic metal particles," *Progress in Solid State Chemistry*, Vol. 12, pp. 185-271, (1979).
[90] W. Ni, X. Kou, Z. Yang, and J. Wang, "Tailoring Longitudinal Surface Plasmon Wavelengths, Scattering and Absorption Cross Sections of Gold Nanorods," *ACS Nano*, Vol. 2, pp. 677-686, (2008).
[91] E. Sassaroli, K. C. P. Li, and B. E. O. Neill, "Numerical investigation of heating of a gold nanoparticle and the surrounding microenvironment by nanosecond laser pulses for nanomedicine applications," *Physics in Medicine and Biology*, Vol. 54, pp. 5541, (2009).
[92] M. Gouy, "Sur la constitution de la charge électrique à la surface d'un électrolyte," *J. Phys. Theor. Appl.*, Vol. 9, pp. 457-468, (1910).
[93] D. L. Chapman, "LI. A contribution to the theory of electrocapillarity," *Philosophical Magazine Series 6*, Vol. 25, pp. 475-481, (1913).
[94] A. Bard and L. Faulkner, *Electrochemical Methods: Fundamentals and Applications* (John Wiley & Sons, Inc, 2001).
[95] P. B. Johnson and R. W. Christy, "Optical Constants of the Noble Metals," *Physical Review B*, Vol. 6, pp. 4370-4379, (1972).
[96] J. W. Penn and E. L. Bell, "Electrical parameter values of some human tissues in the radio frequency radiation range," (USAF School of Aerospace Medicine. Brooks Air Force Base, San Antonio, 1978).
[97] J. L. Carvalho-de-Souza, J. S. Treger, B. Dang, S. B. H. Kent, D. R. Pepperberg, and F. Bezanilla, "Photosensitivity of Neurons Enabled by Cell-Targeted Gold Nanoparticles," *Neuron*, Vol. 86, pp. 207-217, (2015).
[98] S. Genet, R. Costalat, and J. Burger, "A Few Comments on

Electrostatic Interactions in Cell Physiology," *Acta Biotheoretica*, Vol. 48, pp. 273-287, (2000).
[99] T. J. B. Simons, "Calcium and neuronal function," *Neurosurgical Review*, Vol. 11, pp. 119-129, (1988).
[100] M. J. Caterina, M. A. Schumacher, M. Tominaga, T. A. Rosen, J. D. Levine, and D. Julius, "The capsaicin receptor: a heat-activated ion channel in the pain pathway," *Nature*, Vol. 389, pp. 816-824, (1997).
[101] M. Brecht, M. Schneider, B. Sakmann, and T. W. Margrie, "Whisker movements evoked by stimulation of single pyramidal cells in rat motor cortex," *Nature*, Vol. 427, pp. 704-710, (2004).
[102] T. A. Fiacco and K. D. McCarthy, "Astrocyte calcium elevations: Properties, propagation, and effects on brain signaling," *Glia*, Vol. 54, pp. 676-690, (2006).
[103] V. Benfenati, M. Amiry-Moghaddam, M. Caprini, M. N. Mylonakou, C. Rapisarda, O. P. Ottersen, and S. Ferroni, "Expression and functional characterization of transient receptor potential vanilloid-related channel 4 (TRPV4) in rat cortical astrocytes," *Neuroscience*, Vol. 148, pp. 876-892, (2007).
[104] K. W. Ho, W. S. Lambert, and D. J. Calkins, "Activation of the TRPV1 cation channel contributes to stress-induced astrocyte migration," *Glia*, Vol. 62, pp. 1435-1451, (2014).
[105] K. M. Dunn, D. C. Hill-Eubanks, W. B. Liedtke, and M. T. Nelson, "TRPV4 channels stimulate Ca2+-induced Ca2+ release in astrocytic endfeet and amplify neurovascular coupling responses," *Proceedings of the National Academy of Sciences*, Vol. 110, pp. 6157-6162, (2013).
[106] B. MacVicar, "Voltage-dependent calcium channels in glial cells," *Science*, Vol. 226, pp. 1345-1347, (1984).
[107] A. Verkhratsky and H. Kettenmann, "Calcium signalling in glial cells," *Trends in Neurosciences*, Vol. 19, pp. 346-352, (1996).
[108] B.-S. Chen, Y.-C. Lo, Y.-C. Liu, and S.-N. Wu, "Effects of transient receptor potential-like current on the firing pattern of action potentials in the Hodgkin-Huxley neuron during exposure to sinusoidal external voltage.," *Chinese Journal of Physiology*, Vol. 53, pp. 423-429, (2010).
[109] C. Paviolo, J. W. Haycock, J. Yong, A. Yu, P. R. Stoddart, and S. L. McArthur, "Laser exposure of gold nanorods can increase neuronal cell outgrowth," *Biotechnology and Bioengineering*, Vol. 110, pp. 2277-2291, (2013).
[110] J. Yong, K. Needham, W. G. A. Brown, B. A. Nayagam, S. L. McArthur, A. Yu, and P. R. Stoddart, "Gold-Nanorod-Assisted Near-Infrared Stimulation of Primary Auditory Neurons," *Advanced Healthcare Materials*, Vol. 3, pp. 1862-1868, (2014).
[111] S. Yoo, S. Hong, Y. Choi, J.-H. Park, and Y. Nam, "Photothermal Inhibition of Neural Activity with Near-Infrared-Sensitive Nanotransducers," *ACS Nano*, Vol. 8, pp. 8040-8049, (2014).
[112] S. Yoo, R. Kim, J.-H. Park, and Y. Nam, "Electro-optical Neural Platform Integrated with Nanoplasmonic Inhibition Interface," *ACS*

Nano, Vol. 10, pp. 4274-4281, (2016).
[113] V. Goyal, S. Rajguru, A. I. Matic, S. R. Stock, and C.-P. Richter, "Acute Damage Threshold for Infrared Neural Stimulation of the Cochlea: Functional and Histological Evaluation," *The Anatomical Record: Advances in Integrative Anatomy and Evolutionary Biology*, Vol. 295, pp. 1987-1999, (2012).
[114] E. C. Dreaden, A. M. Alkilany, X. Huang, C. J. Murphy, and M. A. El-Sayed, "The golden age: gold nanoparticles for biomedicine," *Chemical Society Reviews*, Vol. 41, pp. 2740-2779, (2012).
[115] A. M. Alkilany, P. K. Nagaria, C. R. Hexel, T. J. Shaw, C. J. Murphy, and M. D. Wyatt, "Cellular Uptake and Cytotoxicity of Gold Nanorods: Molecular Origin of Cytotoxicity and Surface Effects," *Small*, Vol. 5, pp. 701-708, (2009).
[116] W. Jiang, Y. S. KimBetty, J. T. Rutka, and C. W. ChanWarren, "Nanoparticle-mediated cellular response is size-dependent," *Nat Nano*, Vol. 3, pp. 145-150, (2008).
[117] Brett A. Simms and Gerald W. Zamponi, "Neuronal Voltage-Gated Calcium Channels: Structure, Function, and Dysfunction," *Neuron*, Vol. 82, pp. 24-45, (2014).
[118] A. J. Verkhratsky and O. H. Petersen, "Neuronal calcium stores," *Cell Calcium*, Vol. 24, pp. 333-343, (1998).
[119] N. Kato, T. Tanaka, K. Yamamoto, and Y. Isomura, "Distinct temporal profiles of activity-dependent calcium increase in pyramidal neurons of the rat visual cortex," *The Journal of Physiology*, Vol. 519, pp. 467-479, (1999).
[120] A. K. O. Åslund, S. Berg, S. Hak, Ý. Mørch, S. H. Torp, A. Sandvig, M. Widerøe, R. Hansen, and C. de Lange Davies, "Nanoparticle delivery to the brain — By focused ultrasound and self-assembled nanoparticle-stabilized microbubbles," *Journal of Controlled Release*, Vol. 220, Part A, pp. 287-294, (2015).

국문초록

신경 조절은 뇌신경질환 치료 및 신경 기능 연구에 필요하다. 특히, 비접촉, 고분해능인 적외선 신경 자극 방법이 임상과 연구분야에서 큰 주목을 받고 있다. 이러한 점에도 불구하고 적외선 신경자극 방법은 여전히 빛의 집속에 한계가 있을뿐더러 전체 조직 덩어리의 가열로 인한 조직 손상의 위험성을 안고 있다. 본 학위 논문에서는 기존의 적외선 신경자극 방법의 한계를 극복하는 향상된 적외선 신경자극 방법에 대한 논문이다. 본 논문의 첫번째 파트에서는 금나노막대의 국소표면플라즈몬 공명 현상이 낮은 자극 역치로 안전하게 신경을 자극 할 수 있음을 최초로 보였다. 금나노막대를 이용한 빛 신경 자극을 하기 위하여, 레이저 장치, 금나노입자, 그리고 신경 조직을 준비하였다. 근적외선 펄스를 금나노입자가 주입된 곳에 조사할 경우, 금나노입자가 주변 조직보다 빛을 더욱 잘 흡수하여 국소적인 열을 발생시켜 최종적으로 신경을 활성 시킨다. 본 논문의 두번째 파트에서는 표면 처리된 금나노막대로 하여금 세포막 표면에 붙게 하여 외부 유체에 씻겨나가지 않게 하고 또한 효과적인 적외선 신경자극을 위한 세포막 표면에 집중적으로 열을 발생시키게 하였다. 본 논문의 세번째 파트에서는 세포 표적 금나노막대를 이용한 적외선 신경자극 방법을 다른 종류의 세포에도 적용됨을 보였다. 순간적인 세포 내 칼슘이온이 성상교세포에서 관찰되었으며 이를 통하여 금나노막대 기반의 적외선 자극은 신경세포 이외의 다른 종류의 세포에도 적용됨을 보였다. 본 논문의 마지막 파트에서는 금나노막대 기

반의 적외선 신경자극 방법의 원리에 대하여 논하였다. 금나노막대의 공명주파수에 해당하는 근적외선 빛을 금나노막대에 조사할 경우, 국소 전자기파 집속으로 인하여 국소적인 열이 발생한다. 국소 열은 플라즈마 막으로 확산되어 순간적인 막 주변 온도를 상승시킨다. 순간적인 온도 상승으로 세포막 캐패시턴스 혹은 온도 민감성 이온 채널 (예, TRPV1 채널)의 열림을 유발 하며 이로 인하여 신경이 탈분극 된다. 이를 나타내는 신경 모델을 설계하였고, 금나노막대 기반의 신경 자극을 이론적/수학적으로 보였다. 이러한 실험적/이론적 발견은 비침습적 다양한 뇌신경질환 치료 및 다양한 활성 조직의 분석에 가능성을 열 것이다.

주요어 : 적외선신경자극, 금나노 막대, 국소표면플라즈몬공명, 비침습적 신경제어
학 번 : 2012-30216